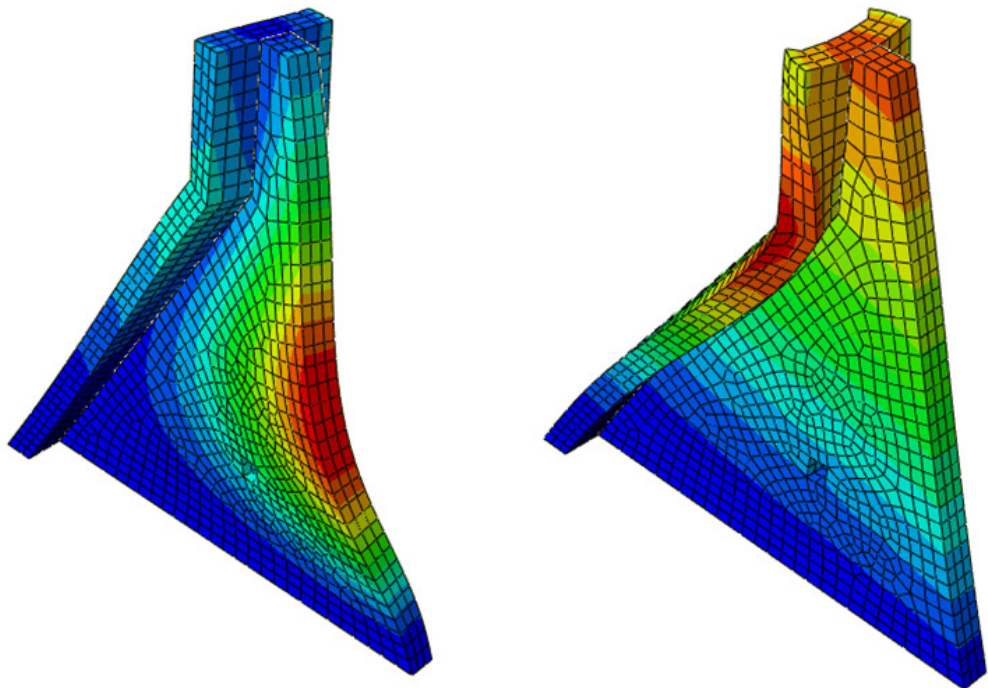


Doctoral Thesis in Civil and Architectural Engineering

Numerical modelling considerations for analysis of concrete hydraulic structures subjected to high-frequency seismic loads

ROGHAYEH ABBASIVERKI



Numerical modelling considerations for analysis of concrete hydraulic structures subjected to high-frequency seismic loads

ROGHAYEH ABBASIVERKI

Academic Dissertation which, with due permission of the KTH Royal Institute of Technology, is submitted for public defence for the Degree of Doctor of Philosophy on Thursday the 6th April 2023, at 10:00 a.m. in Kollegiesalen, Brinellvägen 6, Stockholm.

Doctoral Thesis in Civil and Architectural Engineering
KTH Royal Institute of Technology
Stockholm, Sweden 2023

© Roghayeh Abbasiverki

ISBN 978-91-8040-447-1

TRITA-ABE-DLT-231

Printed by: Universitetsservice US-AB, Sweden 2023

Abstract

Concrete hydraulic structures are of great importance in today's society. When situated in areas with hard bedrock, these structures may become extra vulnerable to seismic excitations as these here are dominated by high-frequency vibrations which can have disastrous consequences for slender structures. The aim of this thesis was to investigate special considerations that must be made when conducting analyses of such hydraulic structures during high-frequency excitations. Underground and on the ground structures were investigated separately. Underground concrete pipelines and concrete buttress dams were selected for the study because their behaviour when exposed to seismic excitations is dominated by their stiffness. The most effective models and modelling methods for the seismic analyses of such structures were implemented and evaluated. Two-dimensional finite element (FE) models were developed for the dynamic analysis of underground concrete pipelines loaded by seismic waves propagating from bedrock through soil. The interaction between the bedrock and the surrounding soil was investigated with respect to rock geometry and soil properties. The surface of dam foundations is commonly irregular, resulting in non-uniform motions at the dam-foundation interface. The free-field modelling methods for concrete dam foundations were adapted in order to accurately describe the propagation of earthquake vibrations from the source to the ground surface. The implementation of a three-dimensional FE model for concrete buttress dams was investigated. Two different methods for free-field modelling are presented, which can be implemented independently of the software used. The seismic loads are applied as effective earthquake forces at non-reflecting boundaries. In the first method, the free-field motions at the non-reflecting boundaries are determined by the so-called domain reduction method using the direct FE calculation. In the second method, the free-field motions are analytically determined based on the one-dimensional wave propagation theory. The results are also compared with the massless foundation modelling approach, in which the topographical amplifications are neglected.

It was demonstrated that a two-dimensional model can effectively account for pipeline behaviour. The most important aspect of the models is the ability to capture bending deformations, as segmented structures such as pipelines are vulnerable in this respect. Non-uniform bedrock reduces the safety of concrete pipeline, especially because of bending deformations in the pipe and joints. The massless method gave unreliable results for analyses of dams, especially for high-frequency excitations. The analytical method was also unreliable in estimating the non-linear behaviour of the dams. But, a new time domain deconvolution method was developed to transform the earthquake motion from the foundation surface to the corresponding input motion at depth. It was found that free-field modelling of foundations using the direct FE method can accurately capture the topographic amplifications of the seismic excitations. It was shown that a three-dimensional model is required for seismic evaluation of concrete buttress dams. The topographic amplification of high-frequency waves at the surface of canyons had a significant effect on the response of this type of dam.

Sammanfattning

Betongkonstruktioner för vattenkraft och vattenförsörjning är av stor betydelse för dagens samhällen. I områden med hård berggrund kan dessa konstruktioner vara särskilt känsliga för seismiska händelser då de domineras av höga frekvenser, vilket kan leda till katastrofala konsekvenser för slanka konstruktioner. Syftet med föreliggande avhandling var att undersöka överväganden och antaganden som måste göras vid analyser av sådana strukturer för vattenkraft och vattenförsörjning vid excitationer med högre frekvenser. Strukturer under jord och på markytan undersöktes separat. Underjordiska rörledningar och lamelldammar av betong valdes till studien eftersom de vid seismiska excitationer domineras av deras styvhet. De mest effektiva modellerna och modelleringsmetoderna för de seismiska analyserna av sådana strukturer implementerades och utvärderades. Tvådimensionella finita element (FE) modeller utvecklades för dynamisk analys av underjordiska rörledningar av betong utsatta för seismiska vågor som utbreder sig från berggrunden och genom jordlager. Samspelet mellan berggrunden och den omgivande marken undersöktes med avseende på bergets geometri och markegenskaperna. Bergytan hos dammfundament är vanligtvis oregelbunden, vilket resulterar i ojämna rörelser vid gränsytan mellan damm och grundläggning. Modelleringsmetoderna med fria fält för betongdammars berggrundläggning har här anpassats för att korrekt beskriva utbredningen av jordbävningsvibrationer från vibrationscentrum till markytan. Implementeringen av en tredimensionell FE-modell för betonglamelldammar undersöktes. Två olika metoder för frifältsmodellering presenteras, vilka kan användas oberoende av aktuell programvara. De seismiska belastningarna appliceras som effektiva jordbävningskrafter vid icke-reflekterande materialgränser. Med den första metoden bestäms de fria fältens rörelser vid de icke-reflekterande gränserna genom den så kallade domänreduktionsmetoden, med direkt FE-beräkning. I den andra metoden bestäms frifältsrörelserna analytiskt utifrån teorin om endimensionell vågutbredning. Resultaten jämförs också med metoden för modellering med antagen masslös undergrund, där de topografiska förstärkningarna försummas.

Det visades att en tvådimensionell modell effektivt kan redogöra för rörledningarnas beteende. Den viktigaste aspekten av modellerna är förmågan att beskriva böjdeformationer, eftersom segmenterade strukturer såsom rörledningar är sårbara i detta avseende. Ojämn berggrund minskar säkerheten för betongrörledningar, särskilt på grund av böjdeformationer i rör och fogar. Metoden som ej beaktade undergrundens massa gav opålitliga resultat vid analys av dammar, speciellt vid högfrekventa excitationer. Den analytiska metoden var också opålitlig när det gäller att uppskatta dammars icke-linjära beteende. Men, en ny metod med konvolution i tidsdomänen utvecklades för att omvandla jordbävningens rörelse från grundläggningsytan till motsvarande rörelse på djupet. Det framkom att modellering av fria fält för grundläggningen med den direkta FE-metoden exakt kan beskriva de topografiska förstärkningarna av de seismiska excitationerna. Det visades att en tredimensionell modell krävs för seismisk utvärdering av betonglamelldammar. Den topografiska förstärkningen av högfrekventa vågor vid markytan hos dalgångar hade en betydande effekt på responsen hos denna typ av damm.

Preface

The research presented in this thesis was carried out at the Division of Concrete Structures, Department of Civil and Architectural Engineering at the Royal Institute of Technology (KTH). During my study under the supervision of Professor Anders Ansell, I have had an excellent opportunity to learn how to work systematically. I have very much enjoyed working under his supervision. He runs a group with a supportive atmosphere, and his expert supervision and continuous support have encouraged me to work with high energy. I give my greatest appreciation and thanks to you, Anders, and I am deeply grateful.

I also wish to express my gratitude towards my co-supervisor Dr Richard Malm for initiating the second part of this project and providing me with advice and support. I would like to thank my second co-supervisor, Adjunct Prof Erik Nordström for his helpful advice. I would also like to thank Adjunct Prof Mikael Hallgren for taking the time to review the thesis. I also express my appreciation all the professors, doctors and colleagues at the Department of Civil and Architectural Engineering.

Last but not least, I would like to express my deepest gratitude to all members of my family, especially my parents and parents-in-law. To my beloved family, my husband Asghar and my daughters Masoumeh and Fatemeh, my warmest and deepest thanks; I dedicate my thesis to you.

Appended papers

The thesis contains the following research papers:

- I. Abbasiverki, R., Ansell, A., Malm, R., *Analysis of shallowly buried reinforced concrete pipelines subjected to earthquake loads*, Nordic Concrete Research 51:111-130, 2014.
- II. Abbasiverki, R., Ansell, A., *Seismic response of large diameter buried concrete pipelines subjected to high frequency earthquake excitations*, Int. J. Structural Engineering, 10(4): 307-329, 2020.
- III. Abbasiverki, R., Malm, R., Ansell, A., *Implementation of free-field modelling of foundations for large dam structures exposed to high-frequency vibrations*, submitted for review.
- IV. Enzell, J., Malm, R., Abbasiverki, A., Ahmed, L., *Non-linear behaviour of a concrete gravity dam during seismic excitation, A case study of the Pine Flat Dam*, In: Numerical Analysis of Dams: Proceedings of the 15th ICOLD International Benchmark Workshop, , Milan, Italy, Springer Nature, 2021.
- V. Abbasiverki, R., Malm, R., Ansell, A., Nordström, E., *Nonlinear Behaviour of Concrete Buttress Dams under High-Frequency Excitations Taking into Account Topographical Amplifications*, Shock and Vibration, Vol 2021, Article ID 4944682, 1-22, 2021.

In Paper I, finite element (FE) modelling was carried out by Abbasiverki with the contribution of Malm. The analyses were carried out by Abbasiverki. The writing and discussion of the results was carried out by Abbasiverki in collaboration with Ansell and Malm. Paper II was written by Abbasiverki in collaboration with Ansell. The FE modelling and analyses were carried out by Abbasiverki, who evaluated the results in collaboration with Ansell. In Paper III, the FE modelling was carried out by Abbasiverki in collaboration with Malm. The simulations were carried out by Abbasiverki. The evaluation and discussion of the results were done by Abbasiverki in collaboration with Malm. Abbasiverki wrote the paper. Ansell and Malm contributed with the overall content and structure of the paper as well as comments on the writing. In Paper IV, Abbasiverki collaborated with Malm in developing the FE model of the foundation. In Paper V, the FE modelling was carried out by Abbasiverki in collaboration with Malm. The analyses were carried out by Abbasiverki and the results were evaluated and discussed with Malm. Abbasiverki wrote the paper. Ansell, Nordström and Malm contributed with the structure of the paper, and comments on the writing and the content of the paper.

Other papers and reports with relevance for the project:

- 1) Abbasiverki, R., Ansell, A., *Analysis of buried reinforced concrete pipelines subjected to seismic waves*, Proceeding of the XXII Nordic Concrete Research Symposium, Iceland, 2014.
- 2) Abbasiverki, R., *Analysis of underground concrete pipelines subjected to seismic high-frequency loads*, Licentiate thesis, KTH Royal Institute of Technology, Stockholm, Sweden, 2016.
- 3) Abbasiverki, R., Nordström, E., Ansell, A., *Initial study on seismic analyses of concrete and embankment dams in Sweden*, Report 164, KTH Concrete Structures, Stockholm, Sweden, 2017.

Table of Contents

CHAPTER 1: Introduction	1
1.1 Background.....	2
1.2 Aim and goals.....	5
1.3 Limitations.....	6
1.4 Contents of thesis.....	6
CHAPTER 2: Wave Propagation in Half-Space	7
2.1 Earthquake waves.....	7
2.2 One-dimensional wave propagation theory.....	9
2.3 Reflection of waves.....	11
2.4 Three-dimensional wave propagation theory.....	13
2.5 Numerical modelling of wave propagation in half space.....	15
2.5.1 Truncated medium.....	15
2.5.2 Seismic source modelling.....	17
2.5.3 Wave propagation in a discrete mesh.....	18
CHAPTER 3: Effective Earthquake Forces	23
3.1 Formulation of effective earthquake forces.....	23
3.2 Computing effective earthquake forces.....	25
3.2.1 Bottom boundary.....	25
3.2.2 Side boundaries.....	26
3.2.3 Propagation of high-frequency impulsive load.....	27
3.3 Effective earthquake forces for foundations with uniform canyon.....	29
3.3.1 Analysis of 1D column.....	31
3.3.2 Analysis of 2D system.....	31
3.4 Analytical method.....	31
3.5 Deconvolution.....	33
CHAPTER 4: Numerical Modelling	39
4.1 Underground pipelines.....	39
4.2 Soil-pipe interface.....	40
4.3 Numerical example for underground concrete pipeline.....	41
4.4 Sensitivity analysis for pipeline length.....	44
4.5 Reservoir modelling.....	46
4.6 Reservoir boundary conditions.....	48
4.7 Dam-foundation-reservoir system.....	49
4.7.1 Contraction joints.....	51
4.7.2 Dam-foundation interface.....	53
4.8 Numerical example for concrete gravity dam.....	53

4.9 Effect of reservoir level on seismic response of concrete gravity dam.....	55
4.10 Numerical example for concrete buttress dam.....	56
4.11 Sensitivity analysis for foundation size.....	58
CHAPTER 5: Summary of Appended Papers	61
5.1 Paper I.....	62
5.2 Paper II.....	62
5.3 Paper III.....	63
5.4 Paper IV.....	63
5.5 Paper V.....	64
CHAPTER 6: Results and Discussion	65
6.1 Effective two-dimensional FE models for underground pipelines.....	65
6.2 Influence of rock geometry variations on buried concrete pipelines	70
6.3 Implementation of free-field modelling of dam foundations	73
6.4 Implementation of 2D and 3D FE models (concrete gravity dams).....	77
6.5 Stiffness-dominated concrete structures on the ground (buttress dams).....	80
CHAPTER 7: Conclusions	89
7.1 Two-dimensional FE models for underground pipelines	89
7.2 Influence of variations in rock geometry and soil stiffness on buried pipelines	90
7.3 Implementation of free-field modelling for dam foundations.....	90
7.4 Implementation of 2D FE models for on the ground structures (gravity dams).	90
7.5 Structural response of stiffness-dominated concrete structures (buttress dam)..	90
7.6 Future work.....	91
REFERENCES	93
NOMENCLATURE	111

CHAPTER 1

Introduction

Concrete structures as parts of the civil infrastructure are of great importance for today's society. They connect cities, enable the transportation of people and goods, and protect the land from flooding and erosion. Water-related infrastructures are called hydraulic structures. They can be part of power plants, water transport systems, water supply systems or irrigation systems. Hydraulic structures are categorised as water retention structures like dams, water-conveying structures (artificial channels and pipelines) or special-purpose structures (for hydropower generation or inland waterways). Figure 1.1 illustrates the most common types of hydraulic structures in hydropower plants. Figure 1.2 shows a schematic representation of a water supply and distribution system. These types of structures are exposed to different loads due to interaction with environmental factors such as water, ice, thermal and earthquakes. An earthquake can cause failure or damage of hydraulic structures. Failure of hydraulic structures can lead to severe environmental damage, loss of life and economic damage [2; 40; 55; 92; 150].

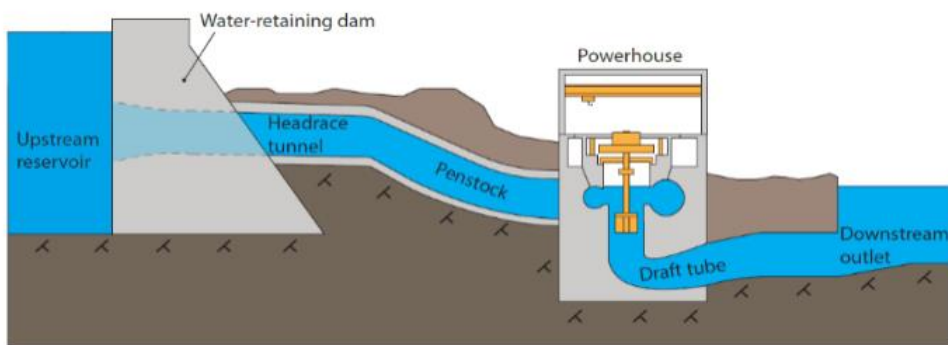


Figure 1.1: Schematic cross section of a hydropower facility [55].

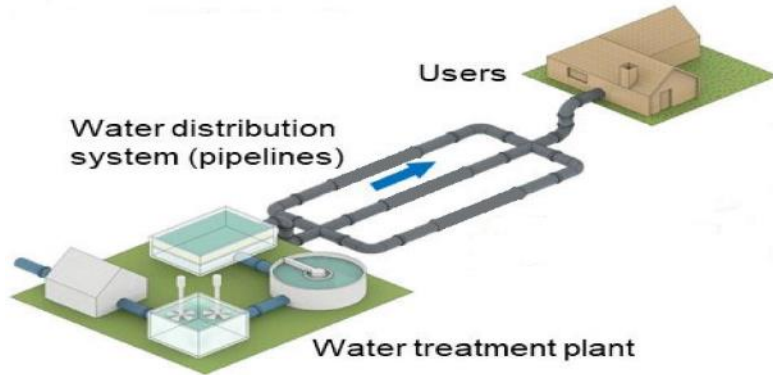


Figure 1.2 Schematic view of a water supply and distribution system [174].

1.1 Background

There are various causes for earthquakes – e.g., volcanic activity, the sudden collapse of a mine/cave or reservoir-induced seismicity (when the reservoirs are filled or drained) – but the cause of most earthquakes globally is plate tectonics. The movement of tectonic plates, both in magnitude and direction, leads to an accumulation of stress within the plates and at their boundaries. When strain reaches its limit along a weak region or at plate boundaries or existing faults, a sudden movement or slip releases the energy of the accumulated strain. This generates elastic waves in the rock mass, which propagate through the elastic medium to the ground surface [45; 50]. The ground motion of an earthquake consists of a combination of harmonic motions with different frequencies. The initial level and frequency content of the motion are influenced by the source conditions [36]. High-frequency seismic waves are generated by a rupture front that concentrates in the initial phase of the earthquake and causes pulses with a high slip rate [66]. High frequencies are quickly attenuated in soft soils and propagate further in stiff soils or rocks. Tests carried out by Svinkin [149] show that the range of dominant frequencies of waves propagating during blasting on construction sites, similar to an earthquake with sudden energy release, is mainly between 10 and 60 Hz. The propagation of such high-frequency waves through rock masses and soil medium can affect underground structures such as pipelines and tunnels, and when the waves reach the ground surface they can damage brittle structures and installations [80; 114; 134].

Before the 1995 Kobe earthquake in Japan, underground structures were considered relatively safe with respect to earthquakes. But the damage done to the Daikai subway station during the earthquake raised new concerns about the vulnerability of underground structures [29; 47]. During an earthquake, buried pipelines can be damaged by deformations caused by wave propagation. An example of this is the damage caused during the 1985 Michoacan earthquake in Mexico City. The local geology and soil variations in the area resulted in damage to large-diameter pipelines [54; 122]. The damage pattern of pipelines largely depends on their material properties and the joint details. According to empirical data from

earthquake loads on pipelines, the damage caused by wave propagation is more severe in brittle than in ductile pipelines, which are 30% more vulnerable compared to the latter [60; 95].

Pipeline materials are generally divided into two groups: rigid and flexible. Concrete and steel pipelines are examples of rigid and flexible piping materials, respectively. Compared to steel, concrete is an economical and durable material that is often used in water and wastewater networks [116]. Concrete pipelines are of particular interest because they are relatively heavy and non-deformable in comparison with steel pipelines. Different types of concrete pipelines are used in water and wastewater networks, i.e., non-reinforced, reinforced and pre-stressed. The joints of concrete pipelines are generally in the form of bells and spigots and sealed with rubber gaskets or mortar [23; 24; 116]. Figure 1.3 shows a typical joint for a reinforced concrete pipeline with a bell and spigot joint sealed with a rubber gasket.

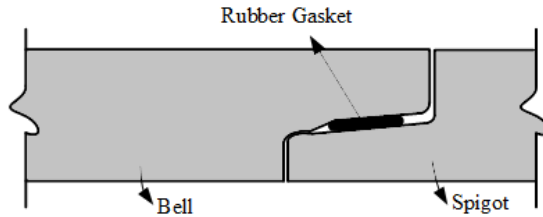


Figure 1.3: Typical joints for reinforced concrete pipelines. Reproduced from [98].

Observations from previous earthquakes show that the principal failure mode of segmented pipelines is axial pull-out at the joints [95; 123; 145]. Field observations and theoretical and experimental studies indicate that damage to buried pipelines is often concentrated to areas with irregular topography and non-uniform soil properties in the horizontal direction [10; 87; 98; 151]. Therefore, for concrete pipelines distributed in regions with hard rock, it is important to investigate how high-frequency excitations can affect the response of concrete pipelines depending on the geological conditions.

Large structures, such as concrete dams, have a large contact area at the interface to the foundation. In most cases, the surface of such foundations has an irregular topography, which can have a significant effect on the wave patterns at a particular site, especially for high-frequency excitations [157; 164]. Data recorded during earthquakes at several points near the interface between a large concrete dam and its foundation showed that the motion is more irregular for the higher-frequency components [121]. Accurate assessment of the seismic performance of concrete dams is of great importance, as the consequences of failure during an earthquake are catastrophic for downstream communities. Chopra [33] recommends certain factors to be considered in the seismic response of concrete dams. It has been shown that neglecting the topography amplifications leads to unrealistic responses in concrete dams. The different methods developed in recent years for the analysis of concrete dams can be divided into two main types: the substructure method [63] and the direct method [163]. The

direct finite element (FE) method has been widely used compared to frequency-based analyses. The reason for this is its ability to account for non-linear effects such as concrete cracking, separation and sliding at joints and interfaces of dam and rock foundation. To facilitate non-linear dynamic analyses, simplifications are considered by engineers and researchers when modelling the rock foundation. A common simplification method is the massless method, which causes uniform movement of the rock surface and is widely used in seismic analyses of concrete dams, e.g., [70; 77; 160]. To account for topographic amplification, a foundation mass with a non-reflective boundary and a suitable free-field input should be used. In recent years, several methods for free-field modelling of foundations have been developed and shown to be effective for low-frequency excitations and for foundations with uniform surfaces [35; 89; 101; 115; 147]. Therefore, adaptation of these methods for modelling irregular rock surface foundations in regions with high-frequency excitations should be investigated.

There are three common types of concrete dams: gravity, arch and buttress dams, as illustrated in Figure 1.4. The gravity dam resists the horizontal pressure of the water through its own weight and consists of several monoliths that are independently stable (see Figure 1.4a). The arch dam is designed to transfer the acting forces to the foundation or abutments through a combination of arch and cantilever action (see Figure 1.4b). Buttress dams are a type of gravity dam, as their design follows the same basic principles. However, they are a lighter version of the gravity dam. In a typical buttress dam, the inclined upstream face (front plate) is supported by buttresses at regular intervals (see Figure 1.4c). The hydrostatic pressure is transferred to the foundation via the slab and buttresses (analogous to gravity dams) [39; 69].

The seismic behaviour of concrete gravity dams and arch dams has been studied by many researchers, e.g., [7; 15; 52; 53; 71; 74; 109; 113; 126; 142; 154; 172]. Concrete buttress dams are vulnerable to strong earthquakes. Examples of two dams that have been shaken by strong earthquakes are the Hsinfengkian Dam in China and the Sefidrud Dam in Iran [144; 5]. However, there is little discussion of the dynamic behaviour of buttress dams in the literature, which mainly focuses on the dams' behaviour in the stream directions [30; 68; 76; 88]. The design of older buttress dams usually only considered gravity and water pressure loads, and the buttress configuration is remarkably efficient in providing the resistance required for these loads. However, for efficiency reasons, the buttresses were built slender and therefore had very little strength to resist cross-stream vibrations [69; 77]. In addition, lower mass and high stiffness lead to a higher natural frequency of the dam, which can have devastating consequences in regions with high-frequency excitations. Therefore, it is important to study the seismic response of such structures, especially in the transverse valley direction during high-frequency excitations.

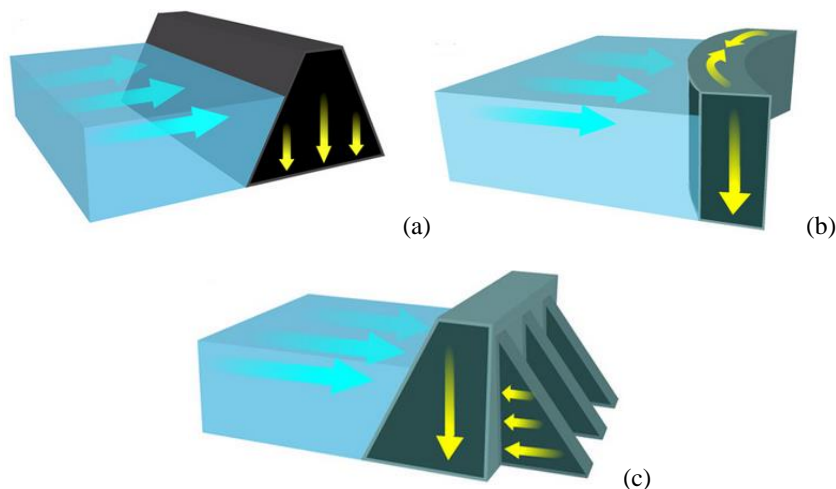


Figure 1.4: Different types of concrete dams: (a) gravity dam, (b) arch dam and (c) buttress dam [39].

1.2 Aim and goals

The overall objective of this thesis is to investigate special considerations that must be made when conducting analyses of concrete hydraulic structures subjected to seismic loading at higher dominant frequencies. In this regard, the most effective models and modelling approaches were implemented and evaluated. Underground and on the ground structures were studied separately. For underground structures, the interaction between bedrock and surrounding soil was investigated. For structures located on the ground, free-field modelling methods were adapted to accurately describe the propagation of earthquake vibrations from their source to the ground surface. The goals of this thesis are defined by the following specific research questions.

When exposed to high-frequency seismic loads:

How can 2D FE models be used effectively for the analysis of underground concrete structures (pipelines)?

How do variations in bedrock geometry and soil properties affect buried concrete pipelines?

How can free-field modelling be used to describe vibrations at dam foundations?

How can 2D and 3D FE models be effectively used for the analysis of concrete structures (gravity dams) on the ground?

How does the structural response of stiffness-dominated concrete structures on the ground change with variations in the dominant load frequencies?

1.3 Limitations

It would be practically impossible to study all the different types of concrete hydraulic structures. Therefore, representative structures were selected for this study. Concrete pipelines were chosen to represent underground concrete structures, since they are stiffness dominated and have large elongations. They are also often important infrastructure components from a safety point of view. When verifying the numerical results of an analysis of concrete pipelines, it was not possible to determine the stresses of the pipes during seismic events in situ, so model tests should be considered, which is beyond the scope of this project. The analyses were carried out for a fixed pipe dimension in a frictional soil. Non-linear soil behaviour and varying soil material properties with ground depth are not considered in the numerical examples.

For on the ground structures, concrete gravity dams were studied as a general case and concrete buttress dams as a special case. A buttress dam is slender and stiffness dominated, meaning that it has higher characteristic natural frequencies and should therefore be more affected by high-frequency loads. The Pine Flat concrete gravity dam was chosen for the numerical benchmark. This is because this dam has been extensively studied and the behaviour of the dam has also been measured through experimental tests. In the cases of the concrete dams considered here, the effects of spillways were neglected. In the modelling of the foundation, non-linearities in the rock due to the sliding along discontinuities were neglected and the rock mass was considered to be linearly elastic and homogeneous.

In this thesis, case studies from a Swedish context are considered because in regions with hard rock i.e., such as Sweden, ground motions are associated with high frequencies. Since Sweden is a region with low seismicity, artificial accelerograms corresponding to Swedish hard rock response spectra were selected in the absence of real earthquake data.

1.4 Contents of thesis

Chapter 2 provides background information on wave propagation in half-space (i.e., an elastic medium where the ground surface is considered as a stress-free edge), numerical modelling of wave propagation and methods for modelling seismic sources. At the end of the chapter, a numerical example of one-dimensional wave propagation is given. Chapter 3 describes the methods implemented for free-field modelling of foundations. This chapter includes numerical examples to show the effects of free-field modelling on the computed surface motion of the dam foundations. This chapter also presents a developed method for seismic wave deconvolution. Chapter 4 presents numerical modelling aspects for the FE modelling of the underground pipeline system and the dam-foundation-reservoir system. Numerical examples for an underground concrete pipeline, a concrete gravity dam and buttress dam are also presented. Chapter 5 provides a summary of the appended papers. Chapter 6 presents the results and a discussion of the work presented in this thesis. Chapter 7 presents the conclusions and suggestions for future work.

CHAPTER 2

Wave Propagation in Half-Space

This chapter describes the fundamental concepts of seismic wave propagation in half-space. First, the different types of seismic waves generated during an earthquake are briefly introduced. Then, one-dimensional and three-dimensional wave propagation theories are summarised. Numerical aspects for the simulation of wave propagation with the FE method are then described. Finally, an example of one-dimensional wave propagation with the FE method is given.

2.1 Earthquake waves

During an earthquake, two types of seismic waves are generated: body waves and surface waves. Body waves are of two types: P-waves and S-waves. An earthquake source simultaneously generates both types of body waves which can propagate through the interior of the earth. However, they arrive at earthquake observation stations at different times due to different propagation speeds. P-waves are known as compressional, longitudinal or primary waves. They are a propagation of compressions and extensions, i.e., a variation of pressure and volume changes. The particle motion during wave propagation is parallel to the direction of propagation (see Figure 2.1a). A typical example of a P-wave is the propagation of sound, and thus P-waves can also propagate through solids and liquids.

S-waves are known as shear, transverse or secondary waves, which cause shear deformation as they propagate through a material. As shown in Figure 2.1b, the motion of the particles is perpendicular to the direction of propagation.

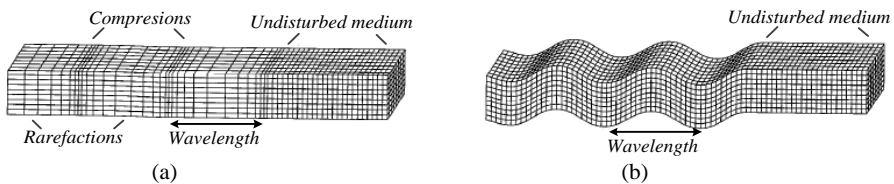


Figure 2.1: Deformations induced by body waves: (a) P-wave; (b) SV-wave [93].

The S-wave is divided into two components depending on the direction of particle movement: movement in the horizontal plane, SH, and movement in the vertical plane, SV. Shear waves generate a considerable amount of horizontal motion at the ground surface, and are thus considered the most significant cause of seismic damage [93].

The propagation velocity of body waves depends on the stiffness of the materials through which they propagate. Geological materials are stiffest when compressed. Therefore, P-waves propagate faster than other seismic waves and are the first to arrive at a given location. Liquids have no shear stiffness and therefore cannot carry S-waves. The propagation velocities of body waves are given by:

$$V_p = \sqrt{\frac{E(1-\nu)}{\rho(1-2\nu)(1+\nu)}} , \quad V_s = \sqrt{\frac{G}{\rho}} \quad (2.1)$$

where V_p and V_s are the propagation velocity of P- and S- waves, respectively. Here, E is the elastic modulus, G the shear modulus, ν the Poisson's ratio and ρ the density. Table 2.1 shows the typical values for P- and S- wave velocities.

Table 2.1: P- and S- wave velocity for different materials [165; 170].

Material Type	S-Wave velocity (m/s)	P-Wave velocity (m/s)
Granite	3000-3500	4500-5500
Sandstone, Shale	1200-1600	2300-3800
Fractured rock	800-1400	2000-2500
Moraine	300-600	1400-2000
Saturated sand and Gravel	100-300	1400-1800
Clay below GW*	40-100	1480-1520
Organic soils	30-50	1480-1520
Dry sand and Gravel	150-350	500-800
Ice	1500-1600	3000-3500
Water	0	1480-1520
Air (-20°C to +60 °C)	-	315-370

*GW: Ground Water level

Surface waves are generated by the interaction between body waves, the surface and surficial layers of the earth. Therefore, they propagate along the ground surface with amplitudes that decrease roughly exponentially with depth. For engineering purposes, the most important surface waves are Rayleigh waves and Love waves. The interaction of P-waves and SV-waves with the ground surface produces Rayleigh waves [93]. Figure 2.2a shows the propagation of Rayleigh waves, which include both vertical and horizontal particle motion. An example of this type of motion is ocean surface waves [155]. The interaction of SH-

waves with a soft surface layer results in Love waves. Figure 2.2b illustrates the propagation of Love waves that do not have a vertical component of particle motion.

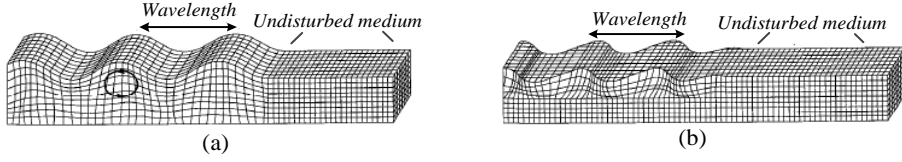


Figure 2.2: Deformations induced by surface waves: (a) Rayleigh wave; (b) Love wave [93].

2.2 One-dimensional wave propagation theory

Consider the free vibration of a semi-infinitely long, linearly elastic soil column with unit cross-sectional area, as shown in Figure 2.3.

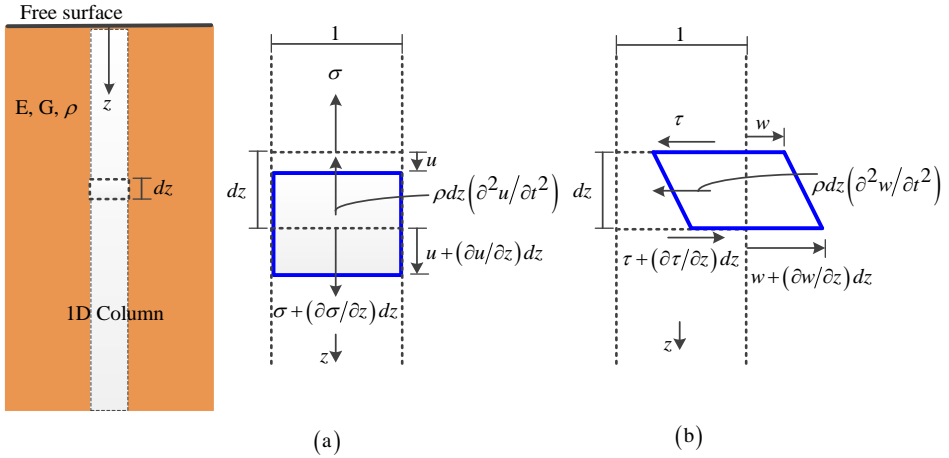


Figure 2.3: Stresses and displacements for an element of length dz in the semi-infinite long column due to one-dimensional propagation of (a) P-wave and (b) S-wave, adapted from [93; 156].

The one-dimensional (1D) equation of motion is obtained by constraining the particle motion to allow only axial deformation for the P-wave or only shear deformation for the S-wave propagation [93; 156]. As the compressive stress wave propagates along the column and passes through the small element in Figure 2.3a, axial stresses and displacements are induced. The dynamic equilibrium of the element gives the one-dimensional equation of motion:

$$\left(\sigma + \frac{\partial \sigma}{\partial z} dz \right) - \sigma = \rho dz \frac{\partial^2 u}{\partial t^2} \quad \rightarrow \quad \frac{\partial \sigma}{\partial z} = \rho \frac{\partial^2 u}{\partial t^2} \quad (2.2)$$

where u is the displacement in the z -direction. The equation of motion is simplified by expressing the left-hand side as displacement, using stress-strain relationship, $\sigma = M \varepsilon$ and

$\varepsilon = \partial u / \partial z$, where the constrained modulus is $M = E(1-\nu)/(1+\nu)(1-2\nu)$. These substitutions give the one-dimensional longitudinal wave equation of the column:

$$\frac{\partial^2 u}{\partial t^2} = \frac{M}{\rho} \frac{\partial^2 u}{\partial z^2} \rightarrow \frac{\partial^2 u}{\partial t^2} = V_p^2 \frac{\partial^2 u}{\partial z^2} \quad (2.3)$$

The particle velocity is determined by using the strain-displacement relationship: $\partial u = \varepsilon \partial z$, the stress-strain relationship: $\varepsilon = \sigma / M$ and the definition of the wave propagation velocity $\partial z = V_p \partial t$:

$$\dot{u} = \frac{\partial u}{\partial t} = \frac{\varepsilon \partial z}{\partial t} = \frac{\sigma}{M} \frac{V_p \partial t}{\partial t} = \frac{\sigma}{M} V_p = \frac{\sigma}{\rho V_p^2} V_p = \frac{\sigma}{\rho V_p} \quad (2.4)$$

Eq. (2.4) shows that the particle velocity is proportional to the axial stress, and where ρV_p is the specific impedance of the material, which is another important property that influences the behaviour of waves at boundaries.

Figure 2.3b shows the shear stresses and displacements caused by the passage of the shear wave in the element. The dynamic equation of motion gives the one-dimensional equation of motion of the S-wave:

$$\left(\tau + \frac{\partial \tau}{\partial z} dz \right) - \tau = \rho dz \frac{\partial^2 w}{\partial t^2} \rightarrow \frac{\partial \tau}{\partial z} = \rho \frac{\partial^2 w}{\partial t^2} \quad (2.5)$$

where w is the displacement in the transverse direction. With the same method as for the P-wave, but using stress-strain relationship $\tau = G\gamma$ and $\gamma = \partial w / \partial z$, the one-dimensional shear wave equation is obtained:

$$\frac{\partial^2 w}{\partial t^2} = \frac{G}{\rho} \frac{\partial^2 w}{\partial z^2} \rightarrow \frac{\partial^2 w}{\partial t^2} = V_s^2 \frac{\partial^2 w}{\partial z^2} \quad (2.6)$$

The particle motion is derived by using $\partial w = \gamma \partial z$ (from the strain-displacement relationship), $\gamma = \tau / G$ (from the stress-strain relationship) and $\partial z = V_s \partial t$ (from the definition of the wave propagation velocity):

$$\dot{w} = \frac{\partial w}{\partial t} = \frac{\gamma \partial z}{\partial t} = \frac{\tau}{G} \frac{V_s \partial t}{\partial t} = \frac{\tau}{G} V_s = \frac{\tau}{\rho V_s^2} V_s = \frac{\tau}{\rho V_s} \quad (2.7)$$

Eq. (2.7) shows that the particle velocity is proportional to the shear stress, where ρV_s is the specific impedance of the material for the shear wave propagation.

From the comparison between Eqs. (2.3) and (2.6), the one-dimensional wave equation for the body wave can be written as a partial differential equation of the form:

$$\frac{\partial^2 v}{\partial t^2} = V^2 \frac{\partial^2 v}{\partial z^2} \quad (2.8)$$

where V is the wave propagation velocity corresponding to the type of stress wave of interest and v is the particle motion. The solution to such an equation can be written as:

$$v(z, t) = f_w(Vt - z) + g_w(Vt + z) \quad (2.9)$$

where f_w and g_w can be any arbitrary functions of $(Vt - z)$ and $(Vt + z)$ satisfying Eq. (2.8). The argument f remains constant as z increases with time (at velocity V), and the argument g remains constant as z decreases with time. Therefore, the solution describes a displacement wave $f_w(Vt - z)$ propagating with velocity V in the positive z -direction and another $g_w(Vt + z)$ propagating with the same speed in the negative z -direction.

2.3 Reflection of waves

When a stress wave propagating along a one-dimensional body reaches an interface, part of its energy is transmitted to the other side of the interface and the rest is reflected back. At the interface, the following equilibrium must be satisfied:

$$\sigma_I + \sigma_R = \sigma_T \quad (2.10)$$

$$\dot{u}_I + \dot{u}_R = \dot{u}_T \quad (2.11)$$

where σ_I , σ_R and σ_T are the stresses of the incident, reflected and transmitted waves, respectively, where, \dot{u}_I , \dot{u}_R and \dot{u}_T are the particle velocities of the incident, reflected and transmitted waves. At an interface between two materials with a specific impedance of $\rho_A V_A$ and $\rho_B V_B$, the particle velocity for incident, reflected and transmitted waves are obtained from Eq. (2.4) or Eq. (2.7):

$$\dot{u}_I = \frac{\sigma_I}{\rho_A V_A} \quad (2.12)$$

$$\dot{u}_T = \frac{\sigma_T}{\rho_B V_B} \quad (2.13)$$

$$\dot{u}_R = \frac{-\sigma_R}{\rho_A V_A} \quad (2.14)$$

During reflection, a positive stress leads to a negative particle velocity which is illustrated by the negative sign in Eq. (2.14). Combining Eqs. (2.10)-(2.11) with Eqs. (2.12)-(2.14), and defining impedance ratio as $\alpha_z = \rho_B V_B / \rho_A V_A$ results in:

$$\begin{cases} \frac{\sigma_T}{\sigma_I} = \frac{2\rho_B V_B}{\rho_B V_B + \rho_A V_A} = \frac{2\alpha_z}{1+\alpha_z} \\ \frac{\sigma_R}{\sigma_I} = \frac{\rho_B V_B - \rho_A V_A}{\rho_B V_B + \rho_A V_A} = \frac{\alpha_z - 1}{1+\alpha_z} \end{cases} \quad (2.15)$$

$$\begin{cases} \frac{\dot{u}_T}{\dot{u}_I} = \frac{2\rho_A V_A}{\rho_B V_B + \rho_A V_A} = \frac{2}{1+\alpha_z} \\ \frac{\dot{u}_R}{\dot{u}_I} = \frac{\rho_A V_A - \rho_B V_B}{\rho_B V_B + \rho_A V_A} = \frac{1-\alpha_z}{1+\alpha_z} \end{cases} \quad (2.16)$$

From Eqs. (2.15) and (2.16), it is clear that the impedance ratio has a significant influence on the reflection and transmission waves at the interface. Different behaviours occur when the impedance ratio is less than or greater than 1. Of particular interest, for example, are the cases of $\alpha_z = 0$ and $\alpha_z = \infty$, where the former represents a free surface and the latter a rigid boundary. The particle velocity and the stress of the reflected and transmitted waves encountering a free surface and a rigid boundary are calculated from Eqs. (2.15) and (2.16) and presented in Table 2.2.

Table 2.2: Particle velocity and stress of reflected and transmitted waves for free surface and a rigid boundary [11].

Impedance ratio	Particle velocity			Stress		
	Incident	Reflected	Transmitted	Incident	Reflected	Transmitted
0	\dot{u}_I	\dot{u}_I	$2\dot{u}_I$	σ_I	$-\sigma_I$	0
∞	\dot{u}_I	$-\dot{u}_I$	0	σ_I	σ_I	$2\sigma_I$

Figure 2.4 shows the reflection of a rectangular stress pulse from a free surface and a rigid boundary. As can be seen, a pressure wave that reaches a free surface is reflected as a tensile wave and vice versa. The reason for this is that $\sigma_R = -\sigma_I$ while the particle velocity is maintained, $\dot{u}_R = \dot{u}_I$ (see Table 2.2). However, with a rigid boundary it is the other way round: the sign of the tension is maintained and the direction of the particle velocity is reversed. Figure 2.4 also shows the principle of superposition, i.e., the net stress and the net

particle velocity at each point where the impulses meet or reflect are the algebraic sums of the instantaneous stresses and the instantaneous particle velocities acting at that point [11; 93].

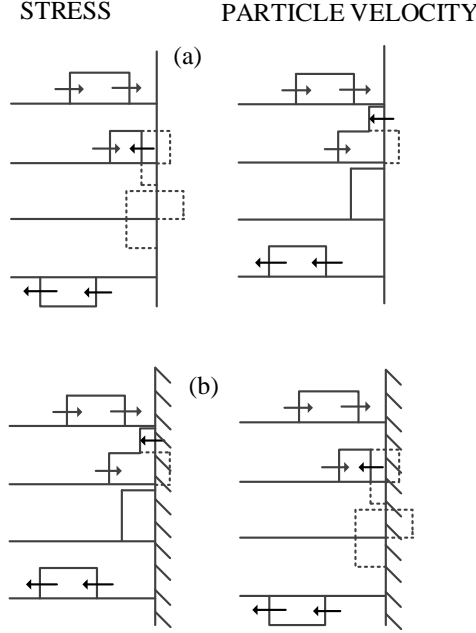


Figure 2.4: Reflection of a rectangular stress pulse at (a) a free surface and (b) a rigid boundary. Dashed lines are pulse components prior to superposition, reproduced from [11].

2.4 Three-dimensional wave propagation theory

Seismic waves in half-space are described by three-dimensional wave propagation because the earth and the sources of seismic energy are three-dimensional. The three-dimensional equations of motion are obtained by the same step used for one-dimensional wave propagation [93]. Figure 2.5 shows the variation of stress in an infinitesimal cube in the x-direction. The dynamic equilibrium in the x-direction gives:

$$\begin{aligned}
 \rho dx dy dz \frac{\partial^2 u_x}{\partial t^2} &= \left(\sigma_{xx} + \frac{\partial \sigma_{xx}}{\partial x} \right) dy dz - \sigma_{xx} dy dz \\
 &+ \left(\sigma_{xy} + \frac{\partial \sigma_{xy}}{\partial y} \right) dx dz - \sigma_{xy} dx dz \rightarrow \rho \frac{\partial^2 u_x}{\partial t^2} = \frac{\partial \sigma_{xx}}{\partial x} + \frac{\partial \sigma_{xy}}{\partial y} + \frac{\partial \sigma_{xz}}{\partial z} \quad (2.17a) \\
 &+ \left(\sigma_{xz} + \frac{\partial \sigma_{xz}}{\partial z} \right) dx dy - \sigma_{xz} dx dy
 \end{aligned}$$

Dynamic equilibrium in the y- and z-directions is also obtained by repeating this operation:

$$\rho \frac{\partial^2 u_y}{\partial t^2} = \frac{\partial \sigma_{yx}}{\partial x} + \frac{\partial \sigma_{yy}}{\partial y} + \frac{\partial \sigma_{yz}}{\partial z} \quad (2.17b)$$

$$\rho \frac{\partial^2 u_z}{\partial t^2} = \frac{\partial \sigma_{zx}}{\partial x} + \frac{\partial \sigma_{zy}}{\partial y} + \frac{\partial \sigma_{zz}}{\partial z} \quad (2.17c)$$

where u_x , u_y and u_z are the displacement components in the x -, y - and z -directions, respectively. σ_{xx} , σ_{yy} and σ_{zz} are normal stresses $\sigma_{xy} = \sigma_{yx}$, $\sigma_{xz} = \sigma_{zx}$ and $\sigma_{yz} = \sigma_{zy}$ are shear stresses. The first and second letters in the subscript describe the direction of the stress itself and the axis perpendicular to the plane in which it acts.

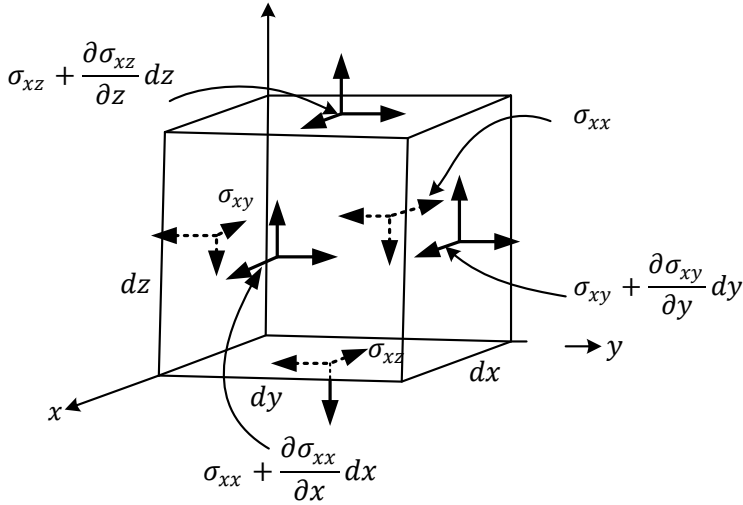


Figure 2.5: Stresses in the x -direction of an infinitesimal cube with dimensions $dx \times dy \times dz$ [93].

Eqs. 2.17 describe the three-dimensional motion of an elastic solid. These equations are expressed in terms of displacements using stress-strain relationship, and strain-displacement relationship. The final equations of motion are formulated:

$$\rho \frac{\partial^2 u_k}{\partial t^2} = (\lambda_L + G) \frac{\partial \bar{\epsilon}}{\partial i} + G \nabla^2 u_k, \quad k=x,y,z \quad (2.18)$$

Where $\bar{\epsilon}$ is the volumetric strain, u_k is the displacement component with respect to the k -th spatial coordinate and λ_L is the Lamé's first constant which is expressed:

$$\lambda_L = \frac{2G\nu}{(1-2\nu)} \quad (2.19)$$

The solution of the equation of motion is a set of uncoupled wave equations representing the propagation of P- and S- waves.

$$\frac{\partial^2 \bar{\varepsilon}}{\partial t^2} = V_p^2 \nabla^2 \bar{\varepsilon} \quad (2.20)$$

$$\frac{\partial^2 \Omega_{kj}}{\partial t^2} = V_s^2 \nabla^2 \Omega_{kj}, \quad \Omega_{kj} = \left(\frac{\partial u_k}{\partial j} - \frac{\partial u_j}{\partial k} \right) \quad (2.21)$$

where Ω_{kj} is the rotation about the normal axis of the kj -plane. The numerical modelling of wave propagation is described below.

2.5 Numerical modelling of wave propagation in half space

Since there are no exact solutions for wave propagation in complex domains, numerical methods are widely used. Various numerical techniques have been used in seismic wave simulations, such as the finite difference method [8], boundary element and boundary integral methods [141], the finite element (FE) method [105], hybrid methods [124] and the spectral element method [59]. Compared to the other methods, the finite element method offers more flexibility in the simulation of geometrically complex domains. The following sections describe important aspects that must be considered in the FE modelling of earthquake waves.

2.5.1 Truncated medium

When simulating wave propagation with the FE method, it is not possible to model a semi-infinite domain directly. The infinite domain must be converted into a finite domain by truncating the physical domain. Suitable boundary conditions should be defined at the truncated surface to absorb outgoing waves and prevent reflections at the truncated surface. Different types of absorbing boundary conditions have been developed, such as viscous boundary conditions [106], viscous spring boundary conditions [48; 99] and perfectly matched layers [16; 18]. One of the earliest non-reflective boundaries is the viscous boundary proposed by Lysmer and Kulemeyer [106], where dashpots on the truncation surface are used to absorb outgoing waves. The dashpot coefficients are obtained by enforcing the one-dimensional radiation condition for body waves, i.e., outgoing waves should not return from the infinite domain to the finite domain. This radiation condition, which assumes that the body waves are perpendicular to the boundary, is defined as follows:

$$\sigma(t) + \rho V_p \dot{u}(t) = 0 \quad (2.22a)$$

$$\tau(t) + \rho V_s \dot{w}(t) = 0 \quad (2.22b)$$

In a FE model, the distributed damper is lumped at the boundary nodes by discrete dampers with coefficients (see Figure 2.6):

$$c_p = A\rho V_p \quad (2.23a)$$

$$c_s = A\rho V_s \quad (2.23b)$$

where A is the tributary area for the boundary node. The viscous damper perfectly absorbs the body waves normally incident on the boundary, but body waves with arbitrary angle of incidence and surface waves are partially absorbed. However, acceptable accuracy is achieved if the boundary is placed at a sufficient distance from the wave source [38]. In this thesis, infinite elements provided by the FE software ABAQUS [1] are implemented as a non-reflective boundary for 2D and 3D models. The infinite element is based on the work of Zienkiewicz et al. [175] for static response and Lysmer and Kuhlemeyer [106] for dynamic response (see Figure 2.7).

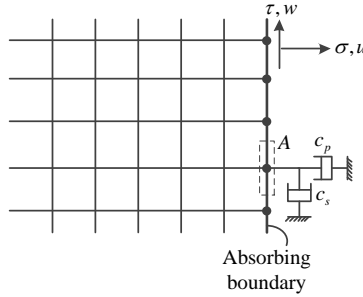


Figure 2.6: Schematic view of lumped viscous dampers in FE modelling, reproduced from [103].

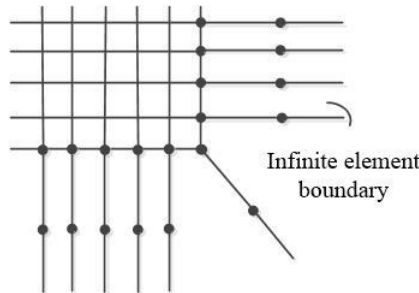


Figure 2.7: Schematic view of infinite elements, reproduced from [1].

2.5.2 Seismic source modelling

One of the major challenges in numerical modelling of seismic wave propagation is the introduction of seismic loading. Two main methods can be considered for modelling seismic sources [129]. There are also other methods that simplify the modelling of seismic sources. In the following sections, the two main methods are presented first, followed by some of the simplified methods.

1. Including seismic source within the computational domain. This is a general method for modelling seismic sources that requires a large computational domain to simulate the propagation of seismic waves from the earthquake source to the local site (see Figure 2.8a). Point source [64; 72; 73] and extended source models [14; 67; 125] can be used to model seismic sources within a computational domain. The former is suitable for simulating faults with insignificant size effects compared to the seismic zone dimension or for simulating weak earthquakes and aftershocks. The latter is used to model faults that are relatively large compared to the seismic zone or to simulate strong earthquake events. However, there are limitations in simulating seismic source within the computational domain, such as: lack of information about the rupture of the specific earthquake, simulation models being limited to lower-frequency components, and also that this method is expensive and time-consuming in practice [86; 129].

2. The seismic source is considered outside the computational domain. In this method, seismic loading is introduced into the FE model in the form of effective earthquake forces (see Figure 2.8b). This method is also called the Domain Reduction Method (DRM) and was proposed by Bielak et al [19]. The DRM is a two-stage FE method in which the effects of incoming waves due to remote excitations are introduced by equivalent nodal forces applied in a single continuous layer of elements inside the truncated boundary. The rigorous procedure for free-field foundations is based on the use of a perfectly matched layer (PML) as the absorbing boundary and DRM for the earthquake input mechanism [17; 173].

The PML boundary and DRM procedure are currently not available in most commercial FE codes; the only exception is LS-DYNA [100]. To overcome this, Lokke and Chopra [103] have developed a DRM-based method using the direct FE method for viscous boundaries. In this method, the effective earthquake forces are applied at the non-reflected boundaries. The effective earthquake forces at non-reflected boundaries can be calculated with an analytical approach using one-dimensional wave theory, a method developed for boundaries with viscous springs [28; 35; 89]. Subsequently, Song et al. [147] further developed this method for use with infinite elements. In the following chapter, two methods for calculating the effective earthquake forces are presented. In the first method, the effective earthquake forces are calculated by direct FE modelling and in the second by an analytical approach.

There are other methods that simplify the modelling of the seismic source, such as 1) using only the artificial boundary condition [41; 42], 2) tied degrees of freedom at the boundaries

[175] and 3) massless foundation [37]. In the first method, the effective earthquake forces on the artificial boundary side are excluded. In the second, the degrees of freedom of the nodes at each level are assumed to be bounded at the side of the truncated domain. The method satisfies the 1D wave propagation requirements, but the radiation condition is not satisfied and waves may be reflected from the boundaries. To minimise scattered wave reflections from the boundaries, a large domain size should be considered [148]. The third method is to use a common approximation in seismic analysis of dams. The massless approach assumes that the rock foundation has no mass. Therefore, the flexibility of the foundation is considered in the dam-foundation interaction system. A limitation of the massless method is the neglected radiation damping effect of the infinite foundation [28; 35; 171].

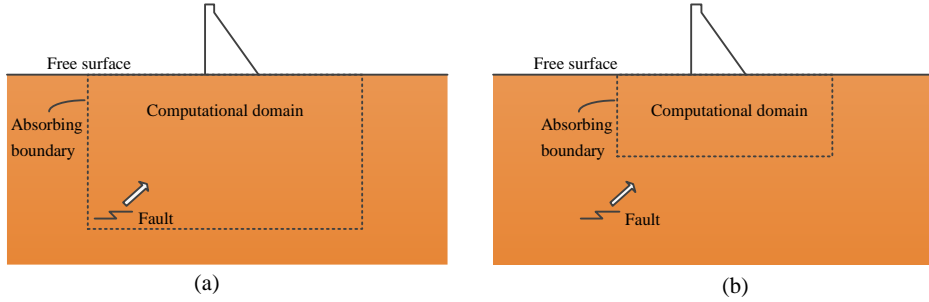


Figure 2.8: Schematic view of seismic source modelling: (a) simulation of seismic source in the computational domain and (b) excluding seismic source from computational domain by computing effective earthquake forces.

2.5.3 Wave propagation in a discrete mesh

When seismic waves propagate through the FE mesh, this behaves like a low-pass filter with a certain cut-off frequency. In this way, seismic waves above the cut-off frequency cannot propagate through the FE model. The cut-off frequency is considered to be the highest frequency of interest. The maximum element size must be adjusted to capture the wavelength of the cut-off frequency. To achieve acceptance accuracy in a FE model, Kuhlemeyer and Lysmer [94] recommended eight elements per wavelength of the slowest-propagating body wave (shear wave) in the elastic material to simulate seismic wave propagation:

$$\lambda = 8l_{el} = \frac{V_s}{f} \quad (2.24)$$

where λ is the wavelength of the cut-off frequency f (Hz). To see the significant effect of a FE mesh in seismic wave transmission, a 1D FE column exposed to vertical propagation of harmonic S- and P- waves with uniform amplitude and frequency has been modelled. The 1D FE column is developed by constraining the degrees of freedom of the nodes on each level. For the propagation of the S-wave, a tangential dashpot is placed at the base of the FE

column and subjected to a shear stress $\tau = 2\rho V_s \dot{w}_I$, where w_I is the incident displacement time history at the base of the column (see Figure 2.9). For the propagation of the P-wave, a normal dashpot is placed at the base of the FE column and subjected to a normal stress $\sigma = 2\rho V_p \dot{u}_I$, where u_I is the incident displacement time history at the base of the FE column (see Figure 2.10). The derivation of the equations for the base stresses applied to the absorbing boundaries is described in the following chapter. The material properties assigned to the column have a shear wave propagation velocity of 1600 m/s², a density of 2500 kg/m³ and a Poisson's ratio of 1/3. The analyses are performed using the FE software ABAQUS [1].

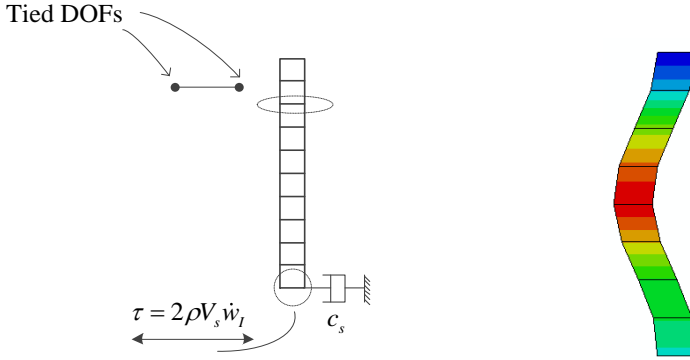


Figure 2.9: Propagation of 1D shear stresses in an FE column.

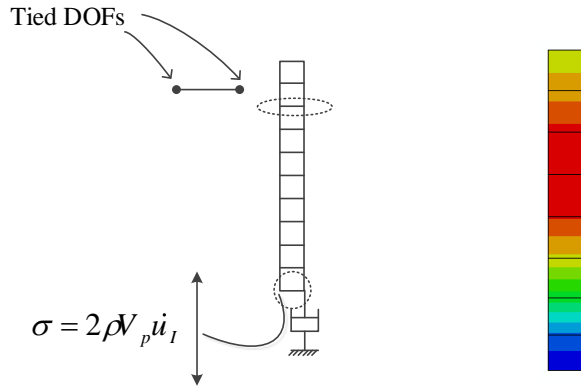


Figure 2.10: Propagation of 1D P-wave stresses in an FE column.

Figure 2.11 shows the recorded time history of the displacement at the free surface of the 1D FE columns due to the propagation of S-waves for different mesh sizes corresponding to two, three, five and eight elements per wavelength. The results are compared with the theoretical solution. As can be seen from the figure, at two and three elements per wavelength, the FE mesh cannot capture the seismic wave and numerical dissipation occurs. With five elements per wavelength, the seismic wave is captured, but with some errors, and with eight elements, acceptable accuracy is achieved. With the P-wave, on the other hand, the wave is captured with two and three elements (see Figure 2.12).

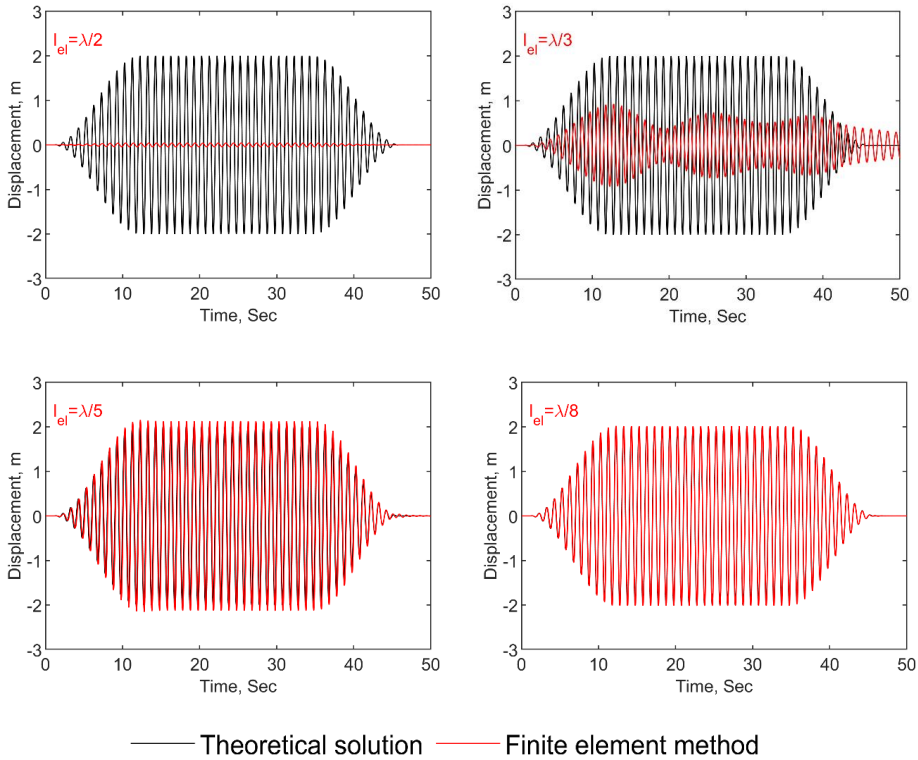


Figure 2.11: FE mesh effect on transmitting a harmonic S-wave with a frequency of 1 Hz in a 1D FE column, considering two, three, five and eight elements per wavelength.

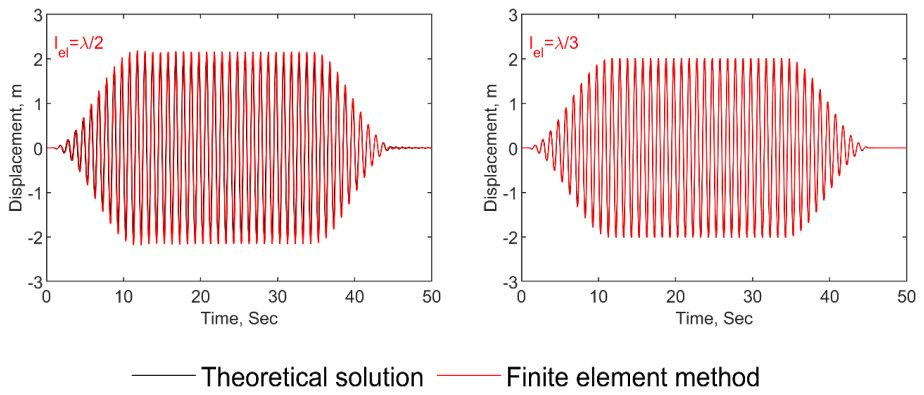


Figure 2.12: FE mesh effect on transmitting a P-wave with frequency of 1 Hz in a 1D FE column, considering two and three elements per wavelength.

CHAPTER 3

Effective Earthquake Forces

This chapter describes the formulation of effective earthquake forces. It then presents the calculations of effective forces based on: 1) the direct FE method [103] and 2) the analytical method [147]. The chapter ends with a description of a method developed for seismic wave deconvolution.

3.1 Formulation of effective earthquake forces

The effective earthquake forces are determined based on the scattering problem, where the local structure disturbs the free-field motion in the unbounded media. Figure 3.1a shows the semi-infinite seismic region before the construction of the local structure.

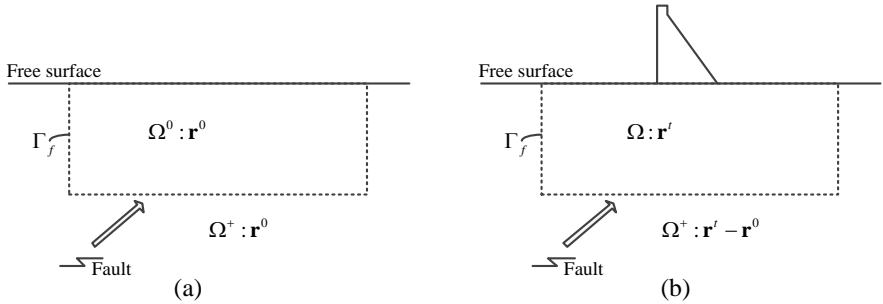


Figure 3.1: Local structure and truncated domain as a scattering problem: (a) semi-infinite seismic region before constructing local structure with displacement field defined by \mathbf{r}^0 in $\Omega^0 \cup \Omega^+$; (b) truncated seismic region including local structure with displacement field defined by the total motion \mathbf{r}^t in Ω and the scattered motion $\mathbf{r}^t - \mathbf{r}^0$ in Ω^+ , reproduced from [103].

This domain is divided into two sub-domains: the region interior of the future absorbing boundary Γ_f and the semi-unbounded exterior region, denoted respectively by Ω^0 and Ω^+ . The free-field displacement at the nodes in both sub-domains is denoted by \mathbf{r}^0 . The actual system with local structure is also separated into two sub-domains: the truncated seismic region with local structure interior of the absorbing boundary Γ_f and the semi-unbounded

exterior region, denoted by Ω and Ω^+ . The displacement field in the actual system, which contains local structure, is defined by the total displacement \mathbf{r}^t in the interior region Ω and the scattered motion $\mathbf{r}^t - \mathbf{r}^0$ in the exterior region Ω^+ . Therefore, the total motion in the system consists of the free-field motion and the scattered motion caused by the presence of the local structure.

The governing equation of motion in the FE model of the local structure with a truncated domain and an absorbing boundary (Figure 3.1b) is:

$$\mathbf{M}\ddot{\mathbf{r}}^t + \mathbf{C}\dot{\mathbf{r}}^t + \mathbf{f}(\mathbf{r}^t) = \mathbf{q}^t \quad (3.1)$$

where \mathbf{M} and \mathbf{C} are the mass and damping matrices, respectively; $\mathbf{f}(\mathbf{r}^t)$ is the internal forces vector, which may be non-linear in the local structure and the adjacent part of the truncated domain; and \mathbf{q}^t are the forces associated with the absorbing boundary Γ_f , which include the effect of the excitation induced by the propagation of seismic waves from a distant earthquake source to the local site and the radiation conditions at the boundaries.

The semi-unbounded region Ω^+ is modelled by the viscous-damper boundary, where the displacements are defined by the scattered motion, $u = u^t - u^0$ and $w = w^t - w^0$. Since the region Ω^+ is assumed to be linear, the boundary tractions associated with the scattered motion are also defined by $\sigma = \sigma^t - \sigma^0$ and $\tau = \tau^t - \tau^0$. Substituting the scattered motion and the corresponding tractions into the viscous boundary radiation condition, Eq. (2.22), yields:

$$\sigma^t = \sigma^0 - \rho V_p [\dot{u}^t - \dot{u}^0] \quad (3.2a)$$

$$\tau^t = \tau^0 - \rho V_p [\dot{w}^t - \dot{w}^0] \quad (3.2b)$$

Therefore, the total tractions at the non-reflected boundary are composed of two parts: the free-field tractions, and the product of the scattered motion and a damper coefficient. For the boundary Γ_f , Eq. (3.2) in matrix and vector notation can be written:

$$\mathbf{q}^t = \mathbf{q}^0 - \mathbf{C}_f [\dot{\mathbf{r}}^t - \dot{\mathbf{r}}^0] \quad (3.3)$$

where \mathbf{q}^0 is the nodal forces vector consistent with the free-field tractions and \mathbf{C}_f is the matrix of damper coefficients c_p and c_s . The final equations of motion for the local structure and the truncated domain are obtained by substituting Eq. (3.3) into Eq. (3.1) and rearranging the terms:

$$\mathbf{M}\ddot{\mathbf{r}}' + [\mathbf{C} + \mathbf{C}_f] \dot{\mathbf{r}}' + \mathbf{f}(\mathbf{r}') = \mathbf{f}^0 \quad (3.4)$$

where the effective earthquake forces acting on the boundary Γ_f are:

$$\mathbf{f}^0 = \mathbf{q}^0 + \mathbf{C}_f \dot{\mathbf{r}}^0 \quad (3.5)$$

The comparison between Eqs. (3.4) and (3.1) shows that the unknown forces \mathbf{q}' at the absorbing boundary are expressed by the viscous damper forces $\mathbf{C}_f \dot{\mathbf{r}}'$ and the effective earthquake forces \mathbf{f}^0 . The effective earthquake forces consist of two parts: (1) the forces \mathbf{q}^0 which are consistent with the free-field tractions at Γ_f , and (2) $\mathbf{C}_f \dot{\mathbf{r}}^0$, the damper forces determined from the spatially varying free-field motion at Γ_f . The methods for calculating the effective earthquake forces are described below.

3.2 Computing effective earthquake forces

Effective earthquake motions are calculated based on the assumption of vertical propagation of seismic waves from an underlying elastic medium.

3.2.1 Bottom boundary

Assuming that the free-field system (Figure 3.1a) is linear and homogenous or horizontally layered, the tractions at bottom boundary due to vertical propagation of seismic waves can be defined as the sum of the tractions σ_I^0 and σ_R^0 due to the incident (propagating upward) and reflected (propagating downward) seismic waves, respectively:

$$\sigma^0 = \sigma_I^0 + \sigma_R^0 \quad (3.6)$$

The free-field motion at the boundary in the normal direction is also defined as the sum of the incident wave u_I^0 and reflected wave u_R^0 , ($u^0 = u_I^0 + u_R^0$). The radiation condition at the boundary must be fulfilled for both the incident and the reflected wave:

$$\sigma_I^0 - \rho V_p \dot{u}_I^0 = 0 \quad \sigma_R^0 + \rho V_p \dot{u}_R^0 = 0 \quad (3.7)$$

Substituting $\dot{u}_R^0 = \dot{u}^0 - \dot{u}_I^0$ into Eq. (3.7), and inserting the result into Eq. (3.6), a new expression for the free-field boundary tractions σ^0 is obtained:

$$\sigma^0 = \rho V_p \left[2\dot{u}_I^0 - \dot{u}^0 \right] \quad (3.8a)$$

For the tangential tractions τ^0 , a similar expression is derived:

$$\tau^0 = \rho V_s [2\dot{w}_t^0 - \dot{w}^0] \quad (3.8b)$$

Free-field tractions in Eq. (3.8) in vector and matrix notation are written as:

$$\mathbf{q}^0 = \mathbf{c}_f [2\dot{\mathbf{r}}_t^0 - \dot{\mathbf{r}}^0] \quad (3.9)$$

The final expression for the effective earthquake forces at the bottom of the foundation domain is obtained by substituting Eq. (3.9) into Eq. (3.5):

$$\mathbf{f}^0 = 2\mathbf{C}_f \dot{\mathbf{r}}_t^0 \quad (3.10)$$

where $\dot{\mathbf{r}}_t^0$ is the incident (upward-propagating) seismic wave. The incident motion is calculated as 1/2 of the outcrop motion at the bottom boundary. The outcrop motion at the base of the foundation is obtained from the deconvolution analysis described in this chapter.

3.2.2 Side boundaries

The free-field motions and tractions at two side boundaries are computed by an auxiliary analysis of the free-field system shown in Figure 3.1a. This system is reduced to a single FE column with a viscous damper at the base subjected to the forces of Eq. (3.10). The FE column is analysed and the free-field motions $\dot{\mathbf{r}}^0$ and tractions \mathbf{q}^0 at each node along the height are calculated. The procedure is shown in Figure 3.2.

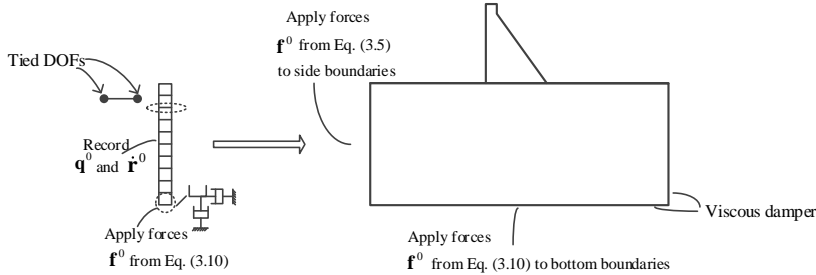


Figure 3.2: Computing effective earthquake forces \mathbf{f}^0 with direct FE method using auxiliary analysis of 1D column to compute $\dot{\mathbf{r}}^0$ and \mathbf{q}^0 , reproduced from [103].

Based on this processor, the following steps are required to compute the lateral effective earthquake forces:

1. **Deconvolution:** The outcrop motion at the bottom boundary is computed for each component of the surface control motion $a_s^k(t)$, $k=x, y$ by 1D deconvolution methods.

2. Computing effective forces at FE column bottom boundary: The effective earthquake forces \mathbf{f}^0 at the bottom boundary are calculated from Eq. (3.10). The incident (upward-propagating) $\dot{\mathbf{r}}_i^0$ is equal to the 1/2 of the outcrop motion extracted from the deconvolution analysis.

3. Developing 1D FE column: The 1D FE column with a single column of elements having the same mesh density as the main FE model at the side boundaries is developed. Viscous dampers are attached at the base in the x - and y -directions (Figure 3.2).

4. Analysing FE column: The column is analysed subjected to the force computed at step 2 and the free-field velocities $\dot{\mathbf{r}}^0$ and forces \mathbf{q}^0 at each node over the height are recorded.

5. Computing lateral earthquake forces: The effective earthquake forces \mathbf{f}^0 at the side boundaries are determined from Eq. (3.5) using $\dot{\mathbf{r}}^0$ and \mathbf{q}^0 recorded in step 4.

3.2.3 Propagation of high-frequency impulsive load

Case B1 presented at the 15th ICOLD International Benchmark Workshop [140] was not included in Paper IV due to space limitations. Case B1 was an analysis of the dam foundation using a high-frequency impulsive loading to show how modelling of the free field at non-reflective boundaries can affect the propagation of shear waves in the rock foundation. Figure 3.3 shows a time history of the impulse velocity and the corresponding Fourier amplitude at the free surface. The characteristic frequency of the load is 40 Hz and the signal sampling frequency is 1000 Hz.

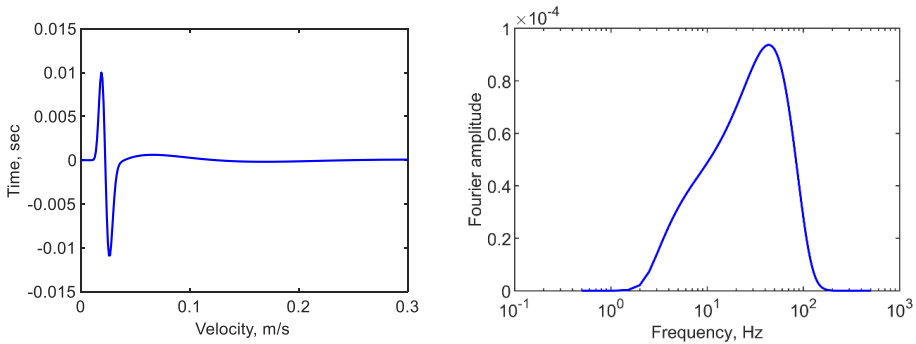


Figure 3.3: High-frequency impulsive time history and corresponding Fourier amplitude spectra.

The response of the foundation was evaluated subjected to a vertical propagation of SH-waves and the responses at the points shown in Figure 3.4 were compared. The incident shear wave at the base of the foundation is 1/2 the free surface motion because the foundation is homogeneous and undamped [27]. The effective earthquake forces at the base of the foundation were obtained from Eq. (3.10). The lateral effective earthquake forces were

determined according to the steps described in the previous section. The generation of the 1D FE column and the force transfer were carried out using Python programming [130]. The analyses were performed for the two cases with inclusion and then with neglect of the lateral earthquake forces.

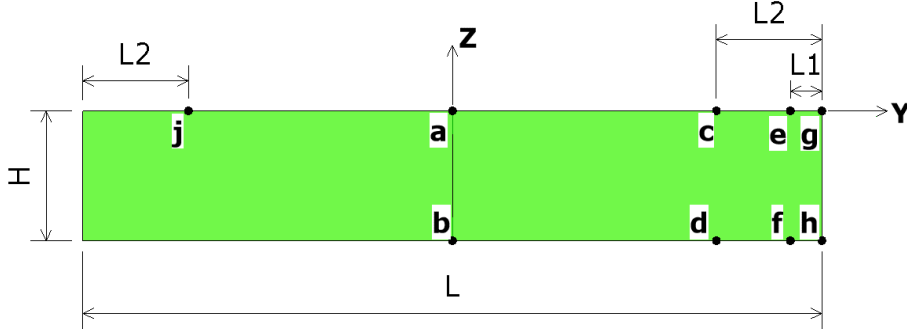


Figure 3.4: Schematic view of a two-dimensional foundation and locations of the points used for results comparison. Dimensions: $L=700$ m, $L1=20$ m, $L2= 100$ m and $H=122$ m.

Figure 3.5 shows the recorded velocity time history at specified points on the foundation base and the free surface in the foundation, taking into account the effective earthquake forces at the lateral absorbing boundaries. Figure 3.6 shows the recorded velocity time history in the foundation without taking into account the effective earthquake forces at the lateral absorbing boundaries.

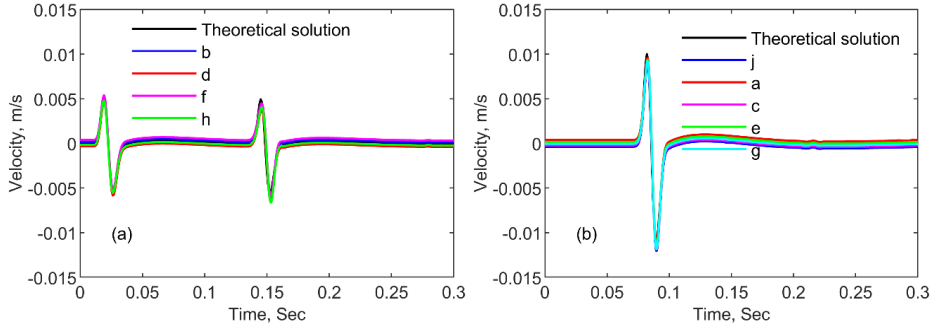


Figure 3.5: Recorded velocity time history in the foundation, considering effective earthquake forces at absorbing boundaries: (a) base of the foundation and (b) free surface.

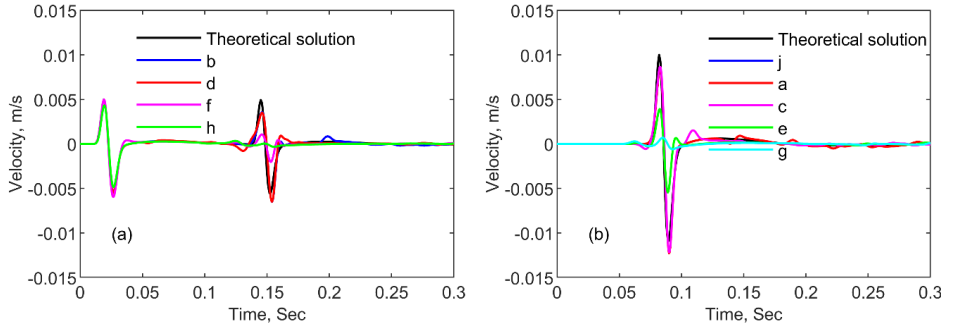


Figure 3.6: Recorded velocity time history in the foundation, neglecting lateral effective earthquake forces at absorbing boundaries: (a) base of the foundation and (b) free surface.

From Figure 3.5 it can be seen that all points correspond exactly to the theoretical solution of wave propagation. In the case where the lateral effective earthquake forces are not considered (Figure 3.6), the points on the absorbing boundary and near the boundary are considerably attenuated by the absorbing boundaries. This effect can also be seen in Figure 3.7, which shows the propagation of the high-frequency impulsive shear stress wave at the time 0.006 seconds before the stress wave arrives at the surface. As can be seen in Figure 3.7a, a shear stress propagates uniformly along the boundaries and within the area. However, in the model without effective earthquake forces, the lateral absorbing boundaries attenuate the upward-going shear stress wave.

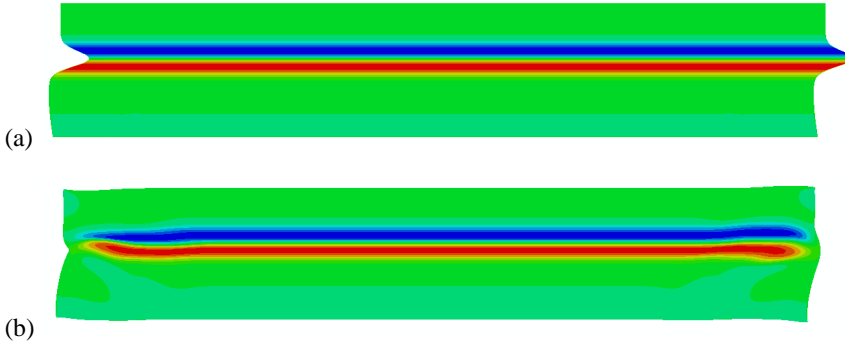


Figure 3.7: Propagation of high-frequency impulsive shear stress at time 0.006 s: (a) including lateral effective earthquake forces and (b) excluding lateral effective earthquake forces.

3.3 Effective earthquake forces for foundations with uniform canyon

For a three-dimensional, semi-unbounded seismic region with an irregular free surface, such as a dam foundation with canyon, the effective earthquake forces are also formulated based on a scattering problem where the dam disturbs a free-field state of the system. Similar to the

2D system described above, the effective earthquake forces are calculated from Eq. (3.10) for the bottom foundation boundaries and Eq. (3.5) for the lateral foundation boundaries. The free-field motions $\dot{\mathbf{r}}^0$ and tractions \mathbf{q}^0 at each node are calculated using the auxiliary analyses. The free-field system shown in Figure 3.8a is reduced to a two-dimensional free-field system with corresponding 1D corner columns, Figure 3.8b. The effective earthquake forces at each node along the lateral boundaries are calculated from Eq. (3.5), where $\dot{\mathbf{r}}^0$ and \mathbf{q}^0 are determined from analyses of a 1D column assumed at the along-canyon boundaries, Figure 3.8c. Free-field motions $\dot{\mathbf{r}}^0$ and tractions \mathbf{q}^0 at the cross –canyon boundaries at the upstream and downstream ends of the domain are determined by analysing the 2D system shown in Figure 3.8d. The required steps for auxiliary analyses are described in Sections 3.3.1-2.

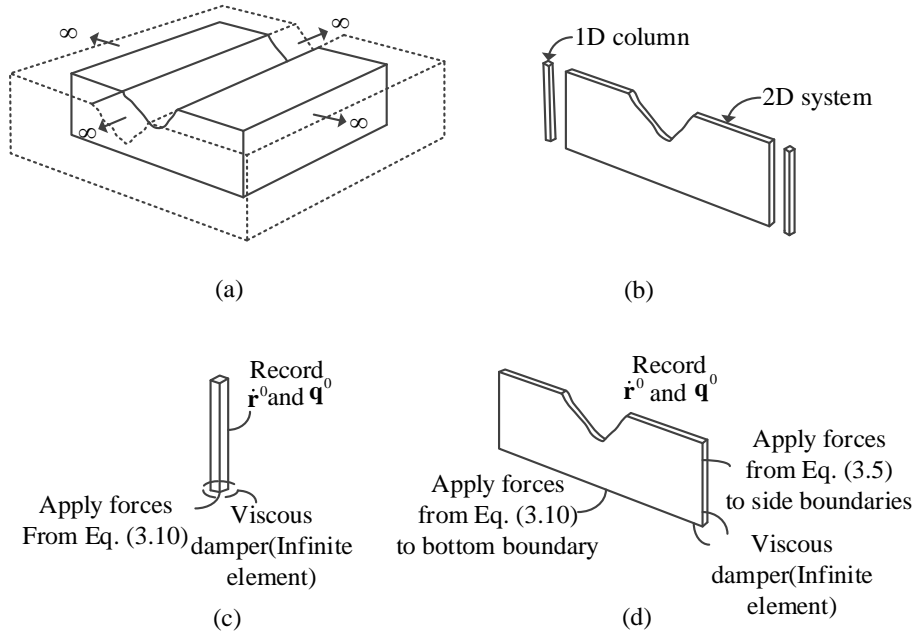


Figure 3.8: Effective earthquake forces with the direct FE method: (a) 3D free-field system with uniform canyon cut in the foundation rock half-space; (b) two-dimensional free-field system with corresponding 1D corner columns; (c) analysis of 1D foundation-rock column to compute $\dot{\mathbf{r}}^0$ and \mathbf{q}^0 at side boundaries, (d) analysis of 2D system to compute $\dot{\mathbf{r}}^0$ and \mathbf{q}^0 at upstream and downstream boundaries, reproduced from [103].

This method was implemented in Papers III and V. Analyses were performed using Python programming [130] to develop 1D and 2D foundation rock systems and transferring forces. The described procedure for calculating the effective earthquake forces is rigorous because the free-field system is identical to the actual system in the domain exterior to the non-

reflected boundaries. However, it requires large amounts of data transfer and bookkeeping. In the following section, an analytical method based on one-dimensional wave propagation theory is presented that simplifies the free-field system to the one-dimensional column [147].

3.3.1 Analysis of 1D column

The following steps are required to develop the 1D corner columns shown in Figure 3.8c:

1. Develop an FE model for the 1D foundation column that has the same mesh density as the boundary of the 2D system.
2. For each component of ground motion, $k = x, y, z$, add a viscous damper at the base in the k direction and constrain the DOFs in the other directions to allow only shear ($k = x, z$) or axial ($k=y$) deformations of the 1D column.
3. Apply the effective earthquake forces from Eq. (3.10) to the base in the k direction and compute $\dot{\mathbf{r}}^0$ and \mathbf{q}^0 at each node along the height.

3.3.2 Analysis of 2D system

The following steps are required to develop the 2D system shown in Figure 3.8d:

1. Develop an FE model for the 2D foundation-rock system with the same mesh density as the main FE model at the upstream/downstream boundary.
2. For each component of ground motion, $k = x, y, z$, add viscous dampers at the bottom and side boundaries and constrain the DOFs at the faces to model the "infinite length" in the direction perpendicular to the model boundary.
3. Apply the effective earthquake forces from Eq. (3.10) to the bottom boundary and from Eq. (3.5) to the side boundaries using $\dot{\mathbf{r}}^0$ and \mathbf{q}^0 from the 1D analysis, and compute $\dot{\mathbf{r}}^0$ and \mathbf{q}^0 at each node in the 2D system.

3.4 Analytical method

In this method, the free-field system of the foundation with any free surface shape is reduced to the 1D column. The effective earthquake forces at the absorbing boundaries are determined by applying the one-dimensional wave theory. The effective earthquake forces are calculated using the following equation:

$$\mathbf{f}^0 = \mathbf{C}_f \dot{\mathbf{r}}^0 + \boldsymbol{\sigma}^0 \mathbf{n} \quad (3.11)$$

where $\boldsymbol{\sigma}^0$ the free-field stress and \mathbf{n} cosine vectors of the outer normal direction of the artificial boundary. The components of the free-field stress are obtained from elastic theory:

$$\begin{Bmatrix} \sigma_{xx} \\ \sigma_{yy} \\ \sigma_{zz} \\ \sigma_{xy} \\ \sigma_{yz} \\ \sigma_{zx} \end{Bmatrix} = \begin{bmatrix} \lambda_L + 2G & \lambda_L & \lambda_L & 0 & 0 & 0 \\ \lambda_L & \lambda_L + 2G & \lambda_L & 0 & 0 & 0 \\ \lambda_L & \lambda_L & \lambda_L + 2G & 0 & 0 & 0 \\ 0 & 0 & 0 & G & 0 & 0 \\ 0 & 0 & 0 & 0 & G & 0 \\ 0 & 0 & 0 & 0 & 0 & G \end{bmatrix} \begin{Bmatrix} \partial u_x / \partial x \\ \partial u_y / \partial y \\ \partial u_z / \partial z \\ \partial u_x / \partial y + \partial u_y / \partial x \\ \partial u_y / \partial z + \partial u_z / \partial y \\ \partial u_z / \partial x + \partial u_x / \partial z \end{Bmatrix} \quad (3.12)$$

where $\begin{bmatrix} u_x & u_y & u_z \end{bmatrix}^T$ denotes the displacement vector. When a P-wave propagates vertically from the bottom boundary, the displacements of the incident wave are $u_x = 0$, $u_y = 0$, $u_z = u_{zI}(t)$. The free-field displacement, velocity and the partial derivative of the displacement in height h are determined from the 1D wave motion theory in two parts, the incident and the reflected waves:

$$\begin{cases} u_z = u_{zI} \left(t - \frac{h}{V_p} \right) + u_{zJ} \left(t - \frac{2H-h}{V_p} \right) \\ \dot{u}_z = \dot{u}_{zI} \left(t - \frac{h}{V_p} \right) + \dot{u}_{zJ} \left(t - \frac{2H-h}{V_p} \right) \\ \frac{\partial u_z}{\partial z} = -\frac{1}{V_p} \left[\dot{u}_{zI} \left(t - \frac{h}{V_p} \right) - \dot{u}_{zJ} \left(t - \frac{2H-h}{V_p} \right) \right] \end{cases} \quad (3.13)$$

where H is the distance from the bottom boundary to the free surface. Using Eqs. (3.12) and (3.13) and taking into account the conditions $u_x = 0$, $u_y = 0$, $h = 0$ at the bottom boundary, the free-field stress is calculated as follows:

$$\begin{Bmatrix} \sigma_{xx} \\ \sigma_{yy} \\ \sigma_{zz} \\ \sigma_{xy} \\ \sigma_{yz} \\ \sigma_{zx} \end{Bmatrix} = \begin{Bmatrix} \lambda_L \frac{\partial u_z}{\partial z} \\ \lambda_L \frac{\partial u_z}{\partial z} \\ \rho V_p^2 \frac{\partial u_z}{\partial z} \\ 0 \\ 0 \\ 0 \end{Bmatrix} = \begin{Bmatrix} -\frac{\lambda_L}{V_p} \left[\dot{u}_{zI}(t) - \dot{u}_{zJ} \left(t - \frac{2H}{V_p} \right) \right] \\ -\frac{\lambda_L}{V_p} \left[\dot{u}_{zI}(t) - \dot{u}_{zJ} \left(t - \frac{2H}{V_p} \right) \right] \\ -\rho V_p \left[\dot{u}_{zI}(t) - \dot{u}_{zJ} \left(t - \frac{2H}{V_p} \right) \right] \\ 0 \\ 0 \\ 0 \end{Bmatrix} \quad (3.14)$$

Substituting Eq. (3.14) into Eq. (3.11) and taking into account the boundary condition $n = [0 \ 0 \ -1]^T$, the effective earthquake force in each direction at the bottom boundary is expressed as:

$$\begin{aligned}
 \begin{Bmatrix} f_x^0 \\ f_y^0 \\ f_z^0 \end{Bmatrix} &= \begin{Bmatrix} c_s \\ c_s \\ c_p \end{Bmatrix} \begin{Bmatrix} 0 \\ 0 \\ \dot{u}_{zl}(t) + \dot{u}_{zl}\left(t - \frac{2H}{V_p}\right) \end{Bmatrix} + \begin{Bmatrix} 0 \\ 0 \\ \rho V_p \left[\dot{u}_{zl}(t) - \dot{u}_{zl}\left(t - \frac{2H}{V_p}\right) \right] \end{Bmatrix} \\
 &= \begin{Bmatrix} 0 \\ 0 \\ c_p \left[\dot{u}_{zl}(t) + \dot{u}_{zl}\left(t - \frac{2H}{V_p}\right) \right] + \rho V_p \left[\dot{u}_{zl}(t) - \dot{u}_{zl}\left(t - \frac{2H}{V_p}\right) \right] \end{Bmatrix}
 \end{aligned} \quad (3.15)$$

When the shear wave propagates vertically from the bottom boundary, the particle displacements within the input wave are $u_x = u_{xl}(t)$, $u_y = 0$, $u_z = 0$, and the effective forces are derived by the analogous method:

$$\begin{aligned}
 \begin{Bmatrix} f_x^0 \\ f_y^0 \\ f_z^0 \end{Bmatrix} &= \begin{Bmatrix} c_s \left[\dot{u}_{xl}(t) + \dot{u}_0\left(t - \frac{2H}{V_s}\right) \right] + \rho V_s \left[\dot{u}_{xl}(t) - \dot{u}_{xl}\left(t - \frac{2H}{V_s}\right) \right] \\ 0 \\ 0 \end{Bmatrix}
 \end{aligned} \quad (3.16)$$

The corresponding effective forces on the four lateral boundaries are derived using the above method. A MATLAB script [110] was used to obtain the effective forces at the foundation boundary nodes, which were then assigned to each node in the FE model. A MATLAB script developed for two- and three-dimensional FE models is implemented in Papers III, IV and V.

3.5 Deconvolution

Design earthquake motions for dynamic analyses are usually given as outcrop motions. However, for direct FE analysis, the seismic input must be applied at the base of the foundation. The corresponding input motion at depth can be calculated by a deconvolution analysis. A typical method for this is carried out in the frequency domain based on 1D shear wave propagation in horizontally layered media, using 1D wave propagation software such as SHAKE or DEEPSOIL [81; 143], or by directly calculating the inverse of the transfer function for a 1D half-space [93]. Software for 1D wave propagation usually calculates two

different base motions at depth: a within motion and an outcrop motion. The within motion is the superposition of the incident and reflected waves, i.e., the actual motion at a certain depth in half-space. This type of base motion is suitable for the input of a rigid base, where a time history of the acceleration (or velocity or displacement) is specified at the base. The main disadvantage of the rigid base is that the downward wave is reflected back to the model. A rigid base is suitable for example when simulating low-velocity sediments over high-velocity rocks at the base [112]. In Papers I and II, rigid base motion is used for the propagation of waves from the hard rock to the soil layer. The outcrop motion is the motion that would occur at a theoretical outcrop location (free surface) at the same depth. To fulfil the condition of zero shear stress at the free surface, the upward and downward wave should be the same. Therefore, the outcrop motion is equal to twice the amplitude of the incident motion. This type of base motion is suitable for a compliant base where an absorbing boundary is used at the base. In this case, the input motion should be applied in the form of seismic stress or nodal force. Note that applying the time history of the incident acceleration (or velocity or displacement) at the absorbing boundary is equivalent to considering a rigid base [112; 128].

In this thesis, a deconvolution method in the time domain is developed based on an iterative procedure. This type of iterative method has been used as an earthquake input mechanism in 2D systems of dam foundations [148]. Here, the iterative method is developed using a one-dimensional FE column subjected to vertical propagation of P- or S- waves. In this method, the frequency and amplitude of the incident motion are adjusted to obtain the target motion at the surface. In the first estimation, it is assumed that the outcrop motion at the base is identical to the target motion. Therefore, the incident motion is considered to be 1/2 of the target motion. The effective earthquake forces are calculated from Eq. (3.10) and applied to the base of the 1D FE column:

$$F_i^{\text{Input}}(t) = 2\rho V_s \dot{u}_i^{\text{Input}}(t) \rightarrow \text{S-wave} \quad (3.17a)$$

$$F_i^{\text{Input}}(t) = 2\rho V_p \dot{u}_i^{\text{Input}}(t) \rightarrow \text{P-wave} \quad (3.17b)$$

where \dot{u}_i^{Input} is the velocity time history of the incident wave. The 1D FE column subjected to the assumed incident motion is analysed and the acceleration time history of the surface and the base is recorded. The correction factor is then calculated by dividing the target response acceleration, $S_a^{\text{Target}}(\omega)$ by the response acceleration of the recorded motion at the free surface of the column, $S_{a-i}^{\text{Response}}(\omega)$:

$$H(\omega) = \frac{S_a^{\text{Target}}(\omega)}{S_{a-i}^{\text{Response}}(\omega)} \quad (3.18)$$

The input motion is modified by multiplying the correction factor by the Fast Fourier Transform (FFT) [32] of the incident motion, $A_{i-1}^{\text{Input}}(\omega)$:

$$A_i^{\text{Input}}(\omega) = H(\omega) A_{i-1}^{\text{Input}}(\omega) \quad (3.19)$$

The new incident motion is transformed into the time domain by Inverse Fast Fourier Transform (IFFT) [32]. The 1D FE column is analysed using the new incoming motion. The free surface motion generated is compared with the target motion. The iteration procedure is continued until the response motion on the surface closely matches the target motion. The accuracy can be calculated using the Euclidean 2 norm [27].

$$r = \frac{\|X - Y\|^2}{\|Y\|^2} = \frac{\sqrt{\sum_{j=1}^{j=n} |x_j - y_j|^2}}{\sqrt{\sum_{j=1}^{j=n} |y_j|^2}} \times 100 \quad (3.20)$$

In the last iteration step, the acceleration time history at the base of the FE column is recorded as a within motion consisting of incident and reflected waves. The outcrop motion is twice the modified input motion:

$$\ddot{u}_{\text{deconvolved}}^{\text{within}}(t) = \ddot{u}_{i-\text{base}}^{\text{Response}} \quad (3.21a)$$

$$\ddot{u}_{\text{deconvolved}}^{\text{outcrop}}(t) = 2\ddot{u}_i^{\text{Input}} \quad (3.21b)$$

The procedure described is summarised in Figure 3.9.

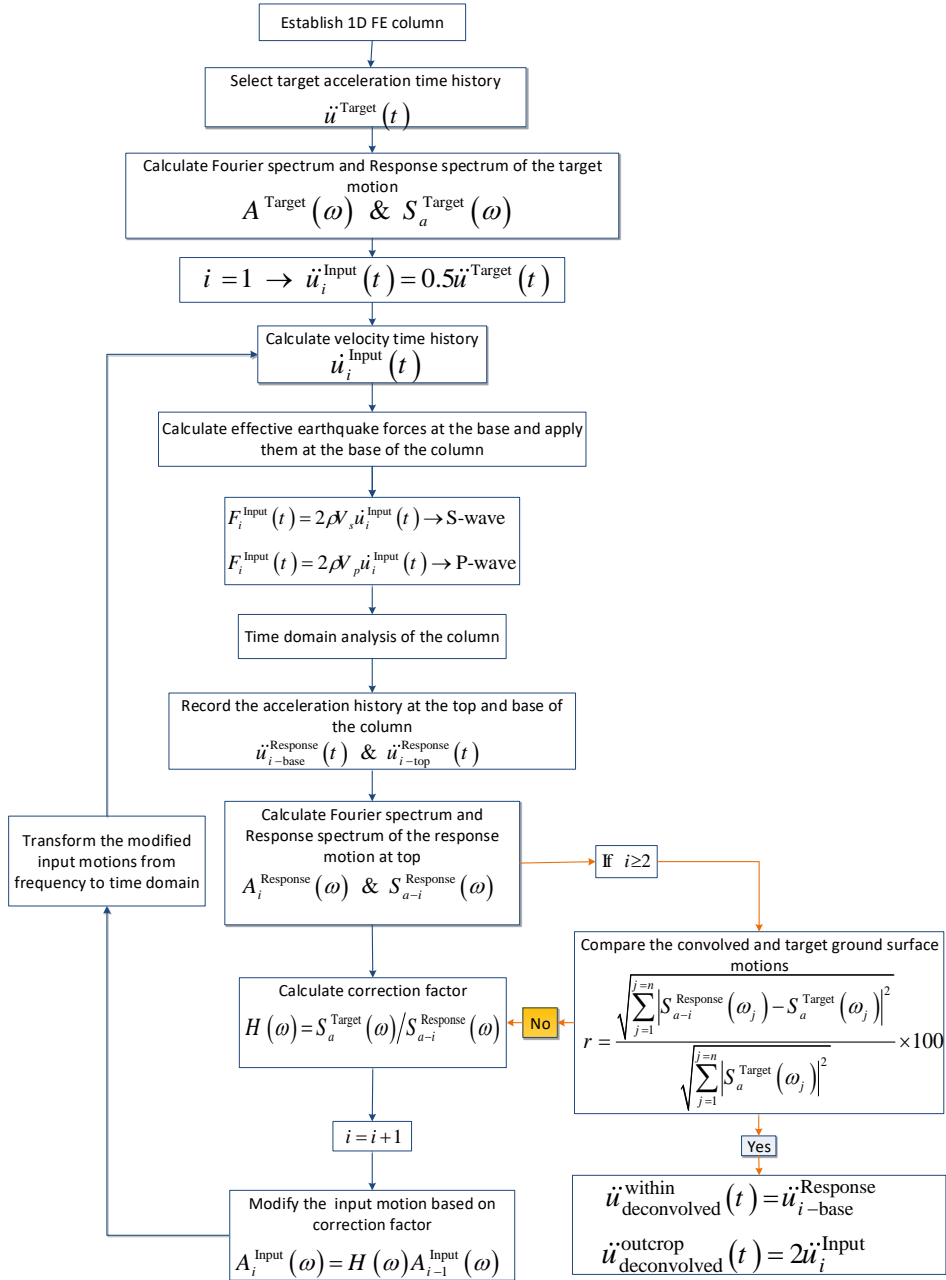


Figure 3.9: Deconvolution of the seismic surface ground motions using time domain iteration method.

To validate the iteration procedure described above, the deconvolution of the Taft earthquake [127] is performed for the foundation shown in Figure 3.4 and compared with within motion at the foundation base provided by the formulators of the 15th ICOLD benchmark workshop [140], which was computed based on the frequency domain analysis. Figure 3.10 shows the deconvolution of the Taft earthquake using the iteration method in the time domain. At each iteration, the recorded motion at the base and free surface of the column is recorded. As can be seen from the figure, the free surface motion recorded in the second iteration agrees with the target free surface motion with an error of $r=1.5\%$.

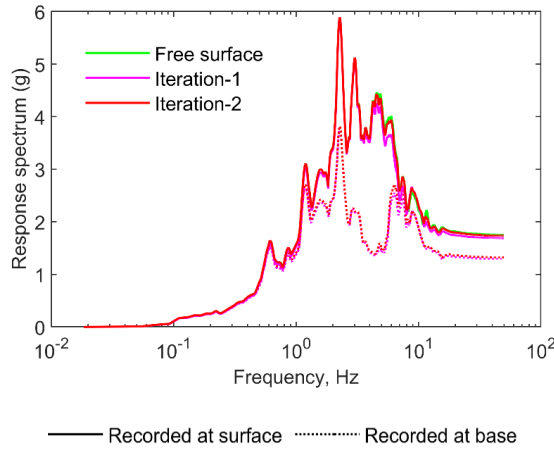


Figure 3.10: Deconvolution of the Taft earthquake using time domain iteration procedure.

The within motion recorded in the iteration procedure is compared in Figure 3.11 with the deconvolved motion computed by frequency method (ICOLD) [140]. It can be seen from the figure that the deconvolved motions determined by the two methods are very similar. To compare the free surface motions produced by the deconvolved motions, a 1D convolution analysis was performed. As can be seen in the figure, the recorded motions of the free surface in the iteration method match the target surface motion. For the frequency method (ICOLD) [140], there are only minor deviations at high frequencies. The reason for this could be related to the input defined for the deconvolution method in the frequency domain. For example, the time domain analysis uses Rayleigh damping, which is frequency dependent, while the frequency domain analysis uses frequency-independent damping. The advantage of deconvolution in the time domain is that the material properties considered in the FE column are the same as in the FE model. With the iteration method in the time domain, the non-linear material behaviour can be taken into account in the case of strong ground motion. Furthermore, the available deconvolution software is based on the vertical propagation of shear waves. Here, deconvolution is performed for both P- and S- waves. However, this method should be extended to take into account the angle of incidence of the waves, as the

angle of incidence is not vertical for soft soil layers near the surface. The inclusion of the non-linearity of the material should also be investigated.

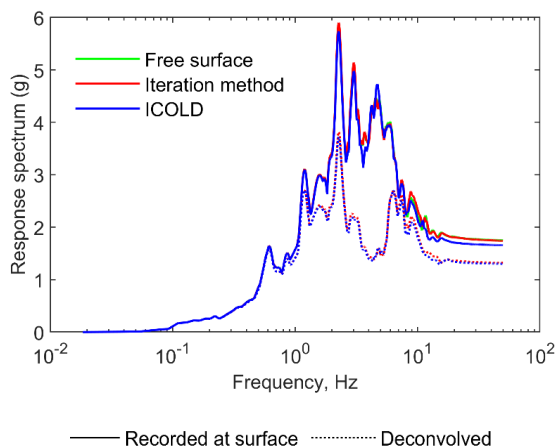


Figure 3.11: Comparison between deconvolved Taft response spectras computed with iteration method and provided by ICOLD [140] and the corresponding produced surface response spectra from 1D convolution analysis.

CHAPTER 4

Numerical Modelling

This chapter describes numerical aspects for the FE modelling of underground pipelines and dam-foundation-reservoir systems. Numerical examples for these types of hydraulic structures are then presented.

4.1 Underground pipelines

For seismic analysis of buried pipelines, accounting for the soil-pipe interaction, the following types of modelling approaches can be found in the literature:

- 1) Quasi-static analysis with soil-structure interaction, where a soil-pipeline system is modelled as a beam embedded in an infinite isotropic homogeneous elastic-plastic medium or surrounded by soil springs, thereby neglecting inertia and damping terms in the dynamic equation [159; 161].
- 2) Dynamic analysis considering the theory of beams on elastic foundations. In this method, the pipe is modelled as a lumped mass and the interaction between the soil and the pipe is considered through a spring-dashpot system whose reactions are derived from static and dynamic continuum theories [43; 44; 82; 83; 120].
- 3) Dynamic analysis by considering shell theory with soil-structure interaction [46; 90; 91; 117; 153; 168].
- 4) Three-dimensional FE analysis where the pipe is modelled by shell elements with soil-pipe interaction considered in the model including the soil around the pipe [167].
- 5) The Beam on Non-linear Winkler Foundation (BNWF) model, in which the pipe is modelled with beam or shell elements and the soil is represented by independent springs lumped at discrete locations on the pipe. This method was proposed by the American Lifelines Alliance (ALA) and has recently been implemented by many authors, e.g., [84; 85; 96; 133; 136; 137; 138].

Models 1 and 2 cannot be used for evaluation of the stress distribution around the cross section of the pipeline. Models 3 and 4 offer the possibility to consider the deformation of the cross section. However, the solution procedures contain a number of equations, which in turn require a large computational effort. Model 5 can be used to derive the cross-sectional deformation of the pipeline, but it has some limitations, e.g., in modelling the lateral variation of the local soil. To address this, this project implements two-dimensional plain strain models where the interaction at the soil-pipe interface is modelled by springs with the behaviour proposed in the ALA guideline. With this model, both longitudinal and cross sections of pipelines are modelled taking into account the lateral variation of the local soil.

4.2 Soil-pipe interface

The soil-pipe interface formulation is modelled using a method proposed by the American Lifeline Alliance (ALA) [9]. This model consists of springs that are distributed in three perpendicular directions with respect to the pipe (see Figure 4.1). The springs have an elastic-plastic behaviour that can describe the sliding of pipelines in the soil during strong earthquakes. The equations corresponding to the spring elements are described below. A full description of how to calculate the parameters can be found in Papers I and II.

Maximum soil resistance to movement in the pipe axial direction is given in units of force per unit length of pipe, as:

$$t_u = \pi D c \alpha_a + \pi D H_B \bar{\gamma}_s \frac{1 + K_0}{2} \tan \delta' \quad (4.1)$$

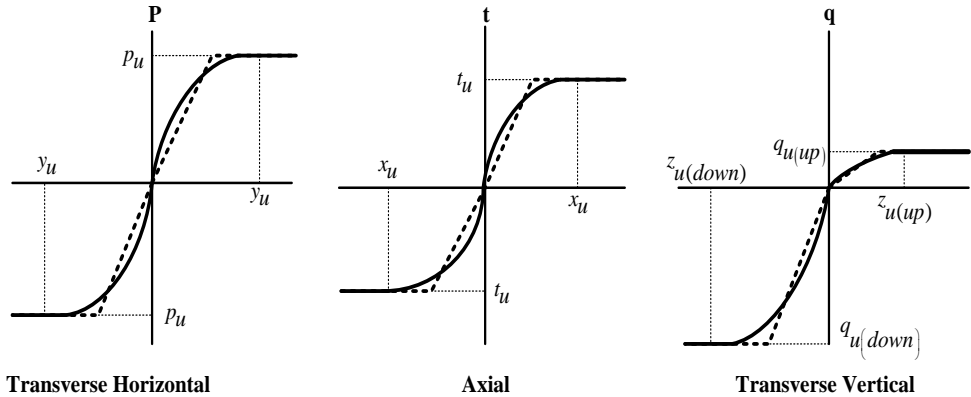


Figure 4.1: Load-deformation relationships for spring elements representing soil-pipeline interaction [9].

These soil springs are based on pile shaft load transfer theory, where D is the outside diameter of the pipe, c the coefficient of cohesion of backfill soil, H_B the depth of soil above the center of the pipeline, $\bar{\gamma}_s$ the effective unit weight of soil, α_a an adhesion factor, δ' the interface angle of friction between pipe and soil, and K_0 a coefficient of soil pressure at rest. An ultimate relative displacement (x_u) corresponding to maximum soil resistance (t_u) is 3-5 mm for sand and 8-10 mm for clays. The maximum lateral resistance of soil per unit length of pipe can be calculated as:

$$p_u = N_{ch}c D + N_{qh}\bar{\gamma}_s H_B D \quad (4.2)$$

These soil springs are picked up from footing and vertical anchor plate pull-out capacity theory and laboratory tests on model pipelines simulating horizontal pipe movements. Here, N_{ch} and N_{qh} are the horizontal bearing capacity factor for clay and sandy soil, respectively. Relative displacement y_u at p_u can be determined by:

$$y_u = 0.04 \left(H_B + \frac{D}{2} \right) \leq 0.01D \text{ to } 0.02D \quad (4.3)$$

The soil spring properties are different for uplift and bearing cases. The maximum soil resistance per unit length of the pipeline in vertical uplift can be calculated as:

$$q_{u(up)} = N_{cv}cD + N_{qv}\bar{\gamma}_s H_B D \quad (4.4)$$

The properties of these soil springs are from pull-out capacity theory and laboratory tests on anchor plates and models of buried pipelines, where N_{cv} and N_{qv} are the vertical uplift factor for clay and sand, respectively. The mobilising displacement of soil, $z_{u(up)}$ at $q_{u(up)}$, can be taken as $0.01H_B$ to $0.02H_B$ for sands and $0.1H_B$ to $0.2H_B$ for clay. The maximum soil resistance per unit length of pipeline in vertical bearing can be calculated as:

$$q_{u(down)} = N_c c D + N_q \bar{\gamma}_s H_B D + N_\gamma \gamma_s \frac{D^2}{2} \quad (4.5)$$

These soil springs are based on bearing capacity theory for footings, where N_c , N_q and N_γ are bearing capacity factors and γ_s is the total unit weight of soil. The soil displacement, $z_{u(down)}$ at $q_{u(down)}$, can be taken as $0.1D$ for granular soils and $0.2D$ for cohesive soils.

4.3 Numerical example for underground concrete pipeline

In this example, a reinforced concrete pipeline with a nominal diameter of 1200 mm and a wall thickness of 135 mm was used for the analyses [135]. The concrete pipeline segments are 2 m long and the 10 cm joints are sealed with cement mortar. Material types B500B and C45/55 are used for the reinforcement and concrete, respectively [22; 56]. The joints of the pipelines are bell and spigot type which are sealed with cement mortar. The pipe joints are

modelled based on Shi's model [145]. The performance of the joints is influenced by the pull-out capacity of the joints, which depends on the tensile strength. Therefore, the joints are modelled by elastic spring elements that take into account the axial and the bending stiffness of the joints depending on the cement mortar properties. A modulus of elasticity of 24.9 GPa, based on [21], is assumed for the mortar. For the simulation of the soil around the pipelines, three types of friction soils with similar properties to Swedish soil types are assumed: the first with low, the second with medium and the third with high stiffness, see Table 4.1 [6; 75].

Table 4.1: Soil and rock properties.

Soil-rock type	Density (kg/m³)	Average shear wave velocity (m/s)	Friction angle	Young's modulus (GPa)
Loose	1400	75	28°	0.021
Medium	1800	250	38°	0.293
Dense	2200	450	45°	1.158
Granite	2500	2600	-	40

As for the damping ratio in the soil according to Eurocode 8 [57], the internal soil damping should be measured by appropriate field or laboratory tests. If there are no direct measurements and the ground acceleration ratio is less than 0.1g, a damping ratio of 0.03 should be used. For ground acceleration ratios of 0.1g-0.2g and 0.2g-0.3g, a damping ratio of 0.03-0.06 and 0.06-0.10 respectively can be used. Here, for a seismic excitation with amplitude of 0.146g, a material damping ratio of 0.05 was assumed for soil and pipeline [58].

Two-dimensional (2D) plane strain FE models were developed for the seismic analysis of concrete pipelines. The models describe two cross sections of the pipelines: longitudinal and transverse cross sections. The FE domain for these cross sections is shown in Figures 4.2-4.4. For the longitudinal cross section, two cases are considered. The first describes the pipeline buried in uniform ground (see Figure 4.2) and the second shows the pipeline buried in non-uniform ground caused by inclined bedrock (see Figure 4.3). The FE models are discretised with four-node bilinear plane strain quadrilateral (CPE4R) elements for the soil medium and the pipe cross section, three-node quadratic 2D truss (T2D3) elements for the reinforcement and two-node linear 2D beam (B21) elements for the longitudinal cross sections of the pipelines. A fine mesh is used near the soil-pipe interfaces, while a coarser mesh is used away from pipe-soil interfaces. The interaction between the reinforcement and the concrete elements is assumed to be fully bonded. The soil-pipe interaction is modelled with SPRING2 elements at the soil-pipe interface. Infinite elements (CINPE4) were placed at the lateral boundaries.

The length of the pipeline has been chosen to capture the longest possible incoming seismic wavelength, where $L=150$ m is an adequate length for the analyses. See Section 4.4 for a sensitivity analysis of the pipeline length. The relevant soil width Z for the transverse cross

section of the pipe is considered to be $Z/2 = 3W$ [3]. Using the above models, the effects of burial depth, soil layer thickness and inclined bedrock are investigated in Paper II (see Table 4.2). The influence of water mass is investigated in Paper I. Wave effects in the water and the interaction between the water and the inside of the pipe are not considered in the model. The water effect is taken into account by increasing the mass of the pipe system.

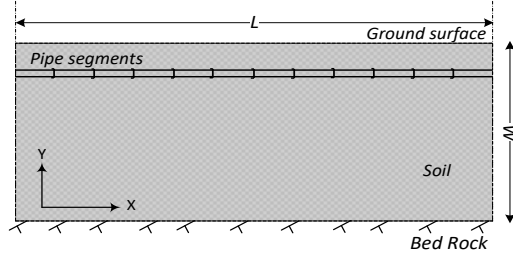


Figure 4.2: Schematic view of FE domain for longitudinal cross section of the pipelines with uniform ground (model 1), from Paper II.

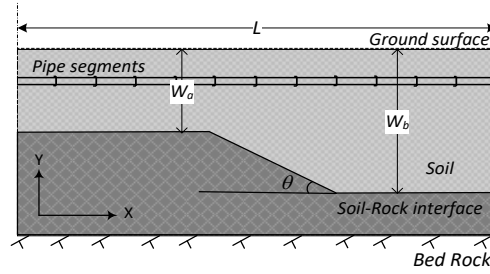


Figure 4.3: Schematic view of FE domain for longitudinal cross section of the pipelines with non-uniform ground (model 2), from Paper II.

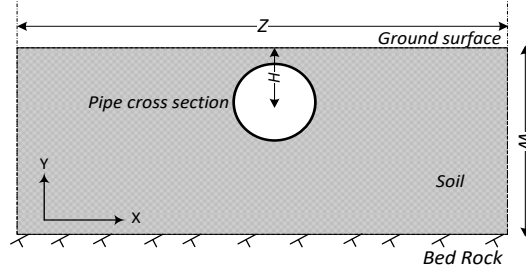


Figure 4.4: Schematic view of FE domain for transverse cross section of the pipelines (model 3), from Paper II.

Table 4.2: Model description for parametric study of concrete pipeline.

Parameter	Model description			
	Model	Rock slope (degrees)	Burial depth (m)	Soil depth (m)
Burial depth	1 and 3	0	$H=1$, $H=5$	$W=25$
Soil layer thickness	1 and 3	0	$H=1$	$W=25$, $W=12$
Inclined bedrock	2	$\alpha=45^\circ$, $\alpha=90^\circ$	$H=1$	$W_a=5$, $W_b=25$

4.4 Sensitivity analysis for pipeline length

For the dynamic analysis of buried pipelines, it is practically impossible to simulate the actual length of a long pipeline. On the other hand, modelling a small segment of the pipeline cannot provide accurate results because the other parts of the pipeline are completely neglected. Therefore, in this study, a sensitivity analysis was performed to find a relevant length for the FE modelling of the studied pipelines. In this regard, four lengths of 75 m, 150 m, 300 m and 600m were selected, corresponding to 0.5, 1, 2 and 4 times the longest wavelength (dominant wavelength) for the cases studied. The analyses were carried out for a uniform ground with dense soil, which gives the longest possible wavelength. The models were subjected to the Swedish design earthquake and the Chi-Chi earthquake [127; 146]. Figures 4.5 and 4.6 show acceleration time history and response spectra of the horizontal component of the Swedish design and Chi-Chi earthquake, respectively.

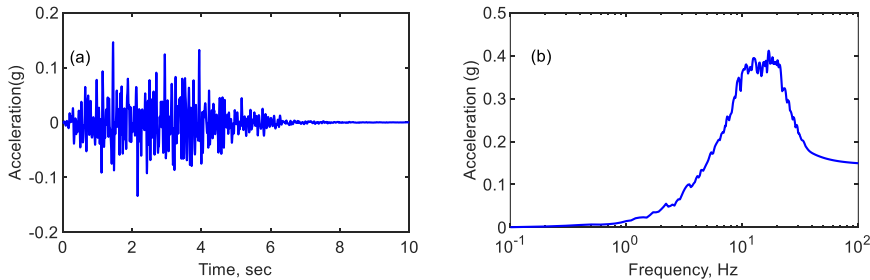


Figure 4.5: Horizontal component (H1) of the Swedish design earthquake: a) acceleration time history and b) response spectra, from Paper II.

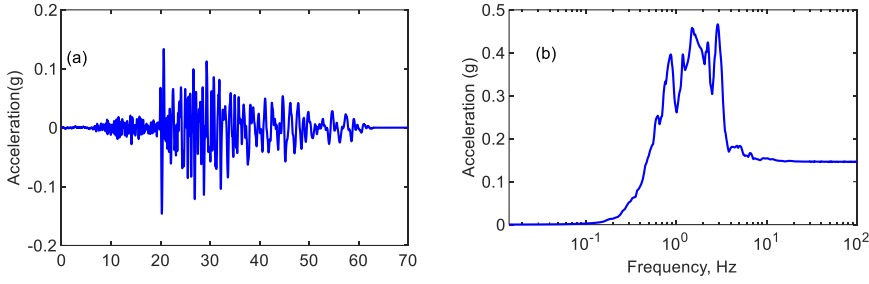


Figure 4.6: Horizontal component (EW) of the Chi-Chi earthquake: a) acceleration time history and b) response spectra, from Paper II.

Figures 4.7 and 4.8 show examples of the maximum envelopes of tensile stresses for axial and bending stresses, respectively. As shown, the maximum stresses occur near the pipeline ends. In Figure 4.7, the maximum axial stresses show some convergence with increasing pipeline length, until the pipelines reach the same stress level at $L=300$ m and $L=600$ m. Similar results are obtained for the Swedish earthquake. In Figure 4.6, the maximum bending stresses occur near the pipeline ends in almost all cases, but with internal peaks along the pipelines. As can be seen in this figure, the maximum stresses for $L=150$ m have converged. For the Chi-Chi earthquake, the results are similar, but with a larger number of internal stress peaks, possibly indicating the occurrence of resonant oscillations.

The results of the sensitivity analysis indicate that the axial and bending stresses converge at pipeline lengths L between 150 and 300 m. In some cases convergence is evident already at $L=150$ m, but in other cases it occurs close to $L=300$ m. In the latter case, which is twice the 150 m that corresponds to the largest wavelength, this relationship is such that the results can be due to the signal sampling, which is governed by the Nyquist sampling theorem that specifies that the sampling rate should be twice the highest frequency present in the signal [166]. This needs to be thoroughly investigated in future work, but for the purpose of the numerical work put forth in this thesis, pipe lengths of $L=150$ m will give adequate precision for the seismic analysis examples that are compared.

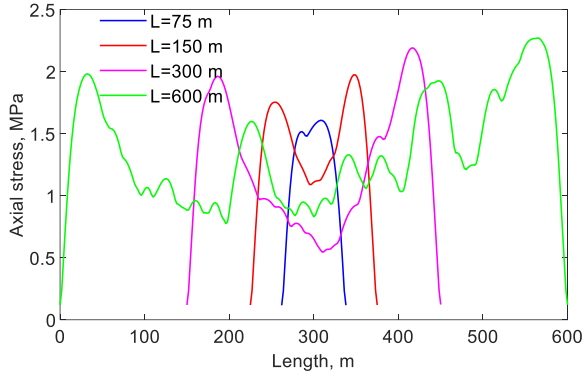


Figure 4.7: Examples of calculated axial stresses for the longitudinal plane section model with varying lengths of pipelines subjected to the Chi-Chi earthquake [3].

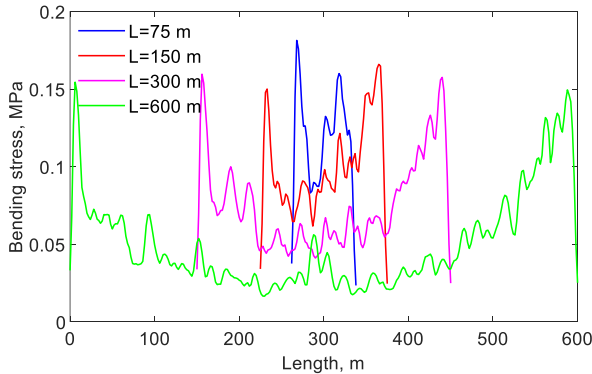


Figure 4.8: Examples of calculated bending stresses for the longitudinal plane section model subjected to the Swedish design earthquake [3].

4.5 Reservoir modelling

The interaction between the reservoir, the dam and the rock foundation during seismic excitation results in hydrodynamic pressure. A simplified method to account for hydrodynamic pressure is the added mass approach [162; 169], where point masses are added to the structure. This method neglects the water-foundation interaction and the compressibility of water. Chopra [33] has shown that neglecting the compressibility of water leads to unreliable seismic evaluation of dams, and stresses are underestimated for some dams but overestimated for others. Numerical modelling of water with finite solid elements was introduced around 1980 and offered the possibility to take into account certain phenomena such as the compressibility of water. However, solid elements can cause other numerical problems, such as instability of the analysis due to the introduction of zero-energy modes.

Modelling water with acoustic elements is more advantageous because there are hardly any numerical problems. Moreover, most phenomena of dynamic fluid-structure interaction can be modelled [108]. The acoustic fluid method has recently been used by many researchers for numerical modelling of the reservoir in the dam-water-foundation system, e.g., [20; 115; 140]. The acoustic fluid is used to simulate the propagation of sound waves, but considering the following assumption, the acoustic wave equation can also be used to simulate fluid-structure interaction problems [70]:

- the fluid is compressible (density changes due to pressure variations)
- the fluid is irrotational
- the fluid viscosity is neglected
- there are only small translations and small velocity (no mean flow of the fluid)
- there are no body forces

The equation for acoustic fluids is derived by using conservation of mass (continuity equation) and conservation of momentum. Expressing the stresses in the acoustic fluid only in terms of pressure, ignoring all external forces and taking into account the above assumptions, yields conservation of momentum:

$$\nabla \cdot p_r + \rho_r \ddot{u}_r = 0 \quad (4.6)$$

where \ddot{u}_r is fluid particle acceleration and p_r is acoustic pressure. With a constant water density ρ_r , the continuity equation for an acoustic medium gives:

$$\frac{\partial \rho_r}{\partial t} + \rho_r \nabla \cdot \dot{u}_r = 0 \quad (4.7)$$

where \dot{u}_r is fluid particle velocity. The two aforementioned equations consist of three unknowns which another equation is needed for solving this set of equations. A constitutive equation or constitutive law describing the differential pressure-density relationship in a compressible fluid is used as an auxiliary equation defined as:

$$\partial p_r = V_r^2 \partial \rho_r \quad (4.8)$$

where V_r is the velocity of wave propagation in water. The time derivative of Eq. (4.7) gives

$$\frac{\partial^2 \rho_r}{\partial t^2} + \rho_r \nabla \cdot \ddot{u}_r = 0 \quad (4.9)$$

The acoustic wave equation is obtained by combining Eqs. (4.6), (4.8) and (4.9), with the fluid pressure as the independent variable:

$$\frac{\partial^2 p_r}{\partial t^2} - V_r^2 \nabla^2 \cdot p_r = 0 \quad (4.10)$$

In FE modelling of acoustic fluids using an FE software, such as ABAQUS, there are special proposed elements called acoustic elements. These elements have only one degree of freedom (pressure), which can be used to simulate the hydrodynamic pressure that occurs in water. In the following, the coupling between a structural-acoustic fluid and the boundary conditions of the reservoir is introduced.

4.6 Reservoir boundary conditions

In the dam-rock-reservoir system, acceleration of the boundaries in contact with the reservoir results in hydrodynamic pressure. The reservoir is in contact with the dam on the upstream side Γ_h and with the rock foundation on the bottom and sides Γ_b , (see Figure 4.9).

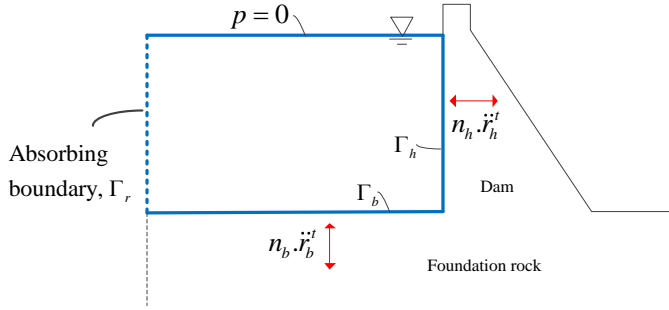


Figure 4.9: Schematic view of the dam-rock-reservoir FE model, with boundary conditions at the reservoir boundaries, reproduced from [103].

The boundary conditions at the fluid–solid interface relate hydrodynamic pressures to the total accelerations $\ddot{\mathbf{r}}^t$:

$$\nabla p_r \cdot \mathbf{n}_h = -\rho_r \mathbf{n}_h \cdot \ddot{\mathbf{r}}_h^t, \quad \text{at } \Gamma_h, \text{ the upstream face of the dam} \quad (4.11)$$

$$\nabla p_r \cdot \mathbf{n}_b + q\dot{p} = -\rho_r \mathbf{n}_b \cdot \ddot{\mathbf{r}}_b^t, \quad \text{at } \Gamma_b, \text{ the reservoir bottom and sides} \quad (4.12)$$

where \mathbf{n}_b and \mathbf{n}_h are the outward normal vectors to the fluid boundaries Γ_b and Γ_h , respectively; ρ_r is the density of water; and q represents the partial absorption of the incident hydrodynamic pressure waves by the sediments at the bottom of the reservoir, the damping coefficient q is given by:

$$q = \frac{1}{V_r} \frac{1 - \alpha_r}{1 + \alpha_r} \quad (4.13)$$

where α_r is the wave reflection factor that is defined by the ratio of the reflected to the incident pressure wave amplitude [103]. The effects of the reservoir bottom sediments can be modelled by using the impedance values of the materials as boundary conditions on the reservoir bottom [4]:

$$C_{\text{sediments}} = \frac{1 + \alpha_r}{1 - \alpha_r} \sqrt{\rho_r K_r} \quad (4.14)$$

where K_r is the bulk modulus. In an advanced method, the sediments of the reservoir are modelled directly and discretised by finite elements [49; 104; 111]. However, in the direct FE method, where the water-foundation interaction and associated radiation damping are included in the analysis, the additional vibrational energy dissipated by the sediments is insignificant. Therefore, the effect of the sediments can be ignored [102].

The boundary condition at the free surface is simply defined as $p_{r=0}$ when neglecting the effects of surface waves, as they have little influence on the seismic response of concrete dams [34].

In FE modelling of reservoirs, it is impractical to do a full modelling of the reservoir as it may be kilometres long due to its nature. Therefore, a truncated region with a suitable radiation condition at the truncated boundary Γ_r should be considered. To avoid reflection problems, Goldgruber [70] recommends a reservoir length that is at least twice the reservoir depth.

4.7 Dam-foundation-reservoir system

In the FE discretisation, the coupled equation of the dam-rock-reservoir system with truncated fluid and foundation regions is given as follows:

$$\begin{aligned} \begin{bmatrix} \mathbf{M} & \mathbf{0} \\ \rho_r (\mathbf{Q}_h^T + \mathbf{Q}_b^T) & \mathbf{S} \end{bmatrix} \begin{Bmatrix} \dot{\mathbf{r}}' \\ \dot{\mathbf{p}}_r' \end{Bmatrix} + \begin{bmatrix} \mathbf{C} + \mathbf{C}_f & \mathbf{0} \\ \mathbf{0} & \mathbf{B} + \mathbf{C}_r \end{bmatrix} \begin{Bmatrix} \mathbf{r}' \\ \mathbf{p}_r' \end{Bmatrix} \\ + \begin{bmatrix} \mathbf{K} & -(\mathbf{Q}_h + \mathbf{Q}_b) \\ \mathbf{0} & \mathbf{H} \end{bmatrix} \begin{Bmatrix} \mathbf{r}' \\ \mathbf{p}_r' \end{Bmatrix} = \begin{Bmatrix} \mathbf{f}_f^0 \\ \mathbf{f}_r^0 \end{Bmatrix} \end{aligned} \quad (4.15)$$

where \mathbf{M} , \mathbf{K} and \mathbf{C} are the standard mass, stiffness and damping matrices, respectively, for the dam–foundation system; \mathbf{S} , \mathbf{B} and \mathbf{H} are the mass, damping and stiffness matrices, respectively, for the water; \mathbf{C}_f and \mathbf{C}_r are the damping matrix at the non-reflected boundaries of the foundation and the reservoir, respectively; \mathbf{r}^t is the total displacement vector in the dam and foundation rock; and \mathbf{p}_r^t is the total hydrodynamic pressure vector in the fluid. The

matrices \mathbf{Q}_b and \mathbf{Q}_h couple accelerations to the hydrodynamic pressures at the water–foundation rock interface and the dam–water interface, respectively:

$$\mathbf{Q}_h = \int_{\Gamma_h} \bar{\mathbf{N}}_h^T \mathbf{n}_h \mathbf{N}_h d\Gamma \quad (4.16)$$

The shape functions of the dam and fluid nodes are $\bar{\mathbf{N}}_h$ and \mathbf{N}_h , respectively, at the interface Γ_h . The matrix \mathbf{Q}_b is constructed in the same way, but integrated over Γ_b .

The effective earthquake forces associated with the absorbing boundary at the truncated boundaries of the foundation and reservoir are \mathbf{f}_f^0 and \mathbf{f}_r^0 , respectively [103]. The effective earthquake forces at the upstream fluid boundary are ignored in analyses that include a sufficiently long fluid domain. This requirement is usually met because long domains are needed to accurately model dam–water interaction and radiation damping when the upstream boundary is modelled by a non-reflected boundary [102].

Damping at the dam is determined from low-amplitude motions within the linear range of response recorded during forced vibration tests, ambient vibrations or small earthquakes. These measured values represent the total damping in the system, which includes material damping, radiation damping and energy loss at the reservoir boundaries – see Lokke and Chopra [102], who summarise the data for damping measured at 32 concrete dams during forced vibration tests and estimated from ambient vibration measurements (see Figure 4.10). The data are for both gravity and arch dams and cover a wide range of system parameters.

As the figure shows, the overall damping values measured at these dams are all in the range of about 1-5%. Based on the measured data, the total damping in the numerical model should not exceed 5% unless a higher value was measured at a particular dam. Lokke and Chopra [102] recommend setting viscous damping ratios in the range of 1-2% for the dam alone and 1-4% for the foundation domain to achieve a total damping of 5% or less in 3D numerical models. Material damping in direct-integration dynamic analyses is considered by Rayleigh damping, which defines a mass and stiffness proportional damping ratio for the i -th mode described by the following equation:

$$\xi_i = \frac{\alpha}{2\omega_i} + \frac{\beta\omega_i}{2} \quad (4.17)$$

where α and β are a mass damping coefficient and a stiffness damping coefficient, respectively. This equation yields a curve that is a function of the circular natural frequency of the i -th mode of vibration $\omega_i = 2\pi f$, [32].

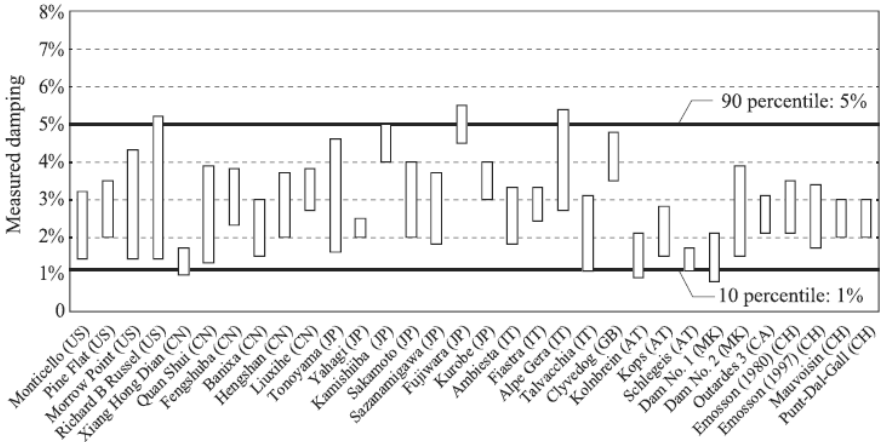


Figure 4.10: Damping at 32 concrete dams measured during forced vibration field tests and estimated from ambient vibration measurements. The range for each dam shows the minimum and maximum damping values measured in the first few (1 to 5) resonant frequencies [102].

4.7.1 Contraction joints

The monoliths and blocks of concrete dams are divided by contraction joints to allow relative movement between the monoliths due to thermal expansion or contraction. These joints are constructed with a water-stop, which is often consisting of bitumen, PVC or steel and has low or no shear resistance in the stream direction. There are also dams where the joints have shear keys. Shear key contraction joints are used in the construction of many dams, especially large arch dams. Shear keys result in a high shear resistance in the stream direction [107].

However, it is likely that the contraction joints will open and close during intense ground motion. A common method for modelling joints is a contact formulation on the surfaces between monoliths [70; 160; 171]. The opening and closing of a joint in the normal direction is modelled by a zero-tensile strength contact constraint with an exponential pressure-overclosure relationship. In an exponential (soft) contact pressure-overclosure relationship, the surfaces begin to transmit contact pressure once the clearance between them, measured in the contact (normal) direction, reduces to c_0 . The contact pressure transmitted between the surfaces then increases exponentially as the clearance decreases further (see Figure 4.11a and the corresponding formula in Eq. (4.13), [1]). Here, p is the contact pressure, d the overclosure and p_0 the contact pressure at zero opening. In practice, p_0 may be better selected based on the elastic modulus of the contacting bodies, the element size, and the element height normal to the contact interface which results in a high value. A large value of p_0 may reduce penetration, but also cause a problem in convergence [118; 158]. However,

if c_0 is set to zero, Eq. (4.18) becomes a hard contact relationship (Figure 4.11b), which does not help improve convergence.

$$p = \begin{cases} 0 & \text{for } d \leq -c_0 \\ \frac{p_0}{(e-1)} \left[\left(\frac{d}{c_0} + 1 \right) \left(e^{\left(\frac{d}{c_0} + 1 \right)} - 1 \right) \right] & \text{for } d > -c_0 \end{cases} \quad (4.18)$$

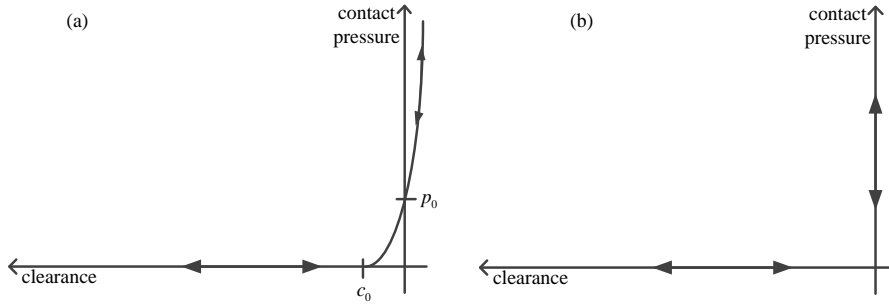


Figure 4.11: Pressure-overclosure relationship: a) exponential and b) hard contact, reproduced from [1].

In the tangential directions, frictional sliding can be modelled by the penalty contact formulation, which is based on the Coulomb friction model [1]. In the ideal Coulomb friction model (Figure 4.12a), two surfaces in contact can carry shear stresses up to a certain magnitude across their interface before they begin to slide relative to each other. This state is called sticking. The Coulomb friction model defines this critical shear stress, τ_{crit} , at which sliding of the surfaces starts as a fraction of the contact pressure p , $\tau_{crit} = \mu p$. The fraction, μ , is known as the coefficient of friction.

Penalty friction formulation based on the Coulomb friction model includes a stiffness that allows some relative motion, i.e., elastic slip of the actual surfaces when they are in the sticking phase (see Figure 4.12b). This can be understood as linear spring stiffness. In ABAQUS, elastic slip can be specified either as a fraction of the element length (slip tolerance) or as an absolute distance. By default, elastic slip is defined as 0.5% of the average length of all contact surface elements in the model. If the value for elastic slip is smaller than the default value, it can be used to increase accuracy [70].

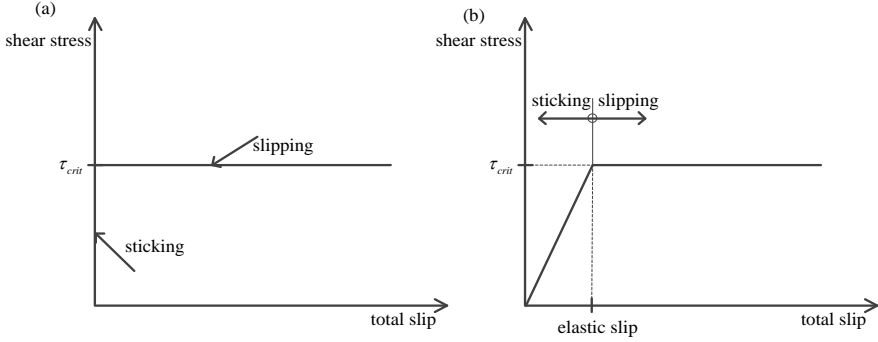


Figure 4.12: Friction curve: (a) ideal Coulomb friction model and (b) general friction curve with penalty formulation, reproduced from [1].

4.7.2 Dam-foundation interface

There are various methods for modelling the interface between dam and foundation. A common assumption is that there is a full bond between the dam and the rock. This assumption can be valid if the rock surface is irregular (blasted), cleaned and free of loose particles [107]. A more realistic modelling of the dam-foundation interface can be achieved by joint interface elements [97] or by a contact formulation described above.

4.8 Numerical example for concrete gravity dam

A concrete gravity dam and concrete buttress dam are studied within Papers IV and V, respectively. The case of the concrete gravity dam includes an analysis of monolith 16 of Pine Flat Dam, which is the tallest non-overflow monolith. Pine Flat Dam is located on the King's River, east of Fresno, California, USA, and was built in 1954. The dam has a length of 561 m with 37 monoliths. The case has been extensively studied before, e.g., [25; 26; 31; 51; 61; 62; 131], which makes it a good choice for comparing analysis methods. Therefore, the formulators of the 15th ICOLD benchmark chose monolith 16 for analyses [139]. Figure 4.13 shows the cross-section geometry of the monolith. As can be seen from the figure, the monolith has a height of 121.91 m and a width of 95.80 m and 9.75 m at the base and the crest, respectively. The width of the monolith (out-of-plane thickness) is 15.24 m. The material properties for the concrete and rock material are summarised in Table 4.3.

Table 4.3: Material properties for both concrete and rock [139].

Density (kg/m ³)	Young's modulus (GPa)	Poisson's ratio	Material damping (%)
2483	22.4	0.2	2

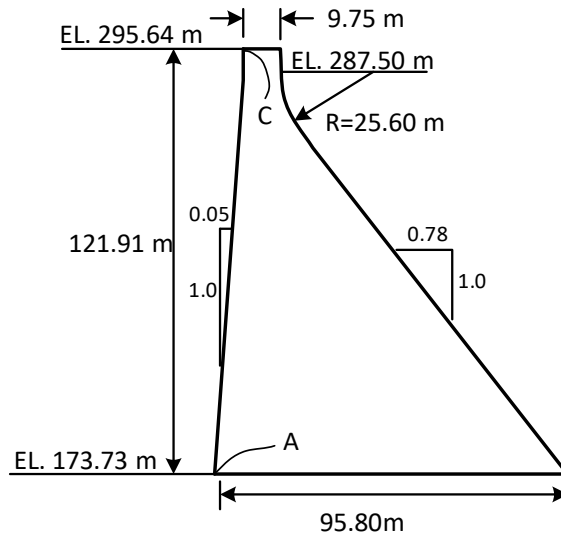


Figure 4.13: Cross-section geometry of monolith 16 of the Pine Flat dam, reproduced from [139].

Figure 4.14 shows a 2D FE domain of Pine Flat Dam. The size of the foundation was given by the formulators as 700 m long and 122 m deep. The foundation is discretised by 2,340 elements of CPE4R. A total of 157 infinite elements of CINPE4 are placed at the lateral and bottom boundaries of the foundation. The monolith is discretised by 11862 three-node linear plain strain (CPE3) elements. A tie constraint has been defined between the intersections of the dam, the foundation and the reservoir. The reservoir has a length of 305 m. The formulators specified three different reservoir levels: the winter reservoir water level (WRWL) at El. 268.2 m, the summer reservoir water level (SRWL) at El. 278.6 m and the normal reservoir level (NRWL) at El. 290.0 m. The influence of the different reservoir levels on the dam's response is described in Section 4.9. In Paper IV, the water level of the winter reservoir was considered. The reservoir is discretised by 28,858 acoustic elements of AC2D4. At the end of the reservoir there are absorbing boundaries.

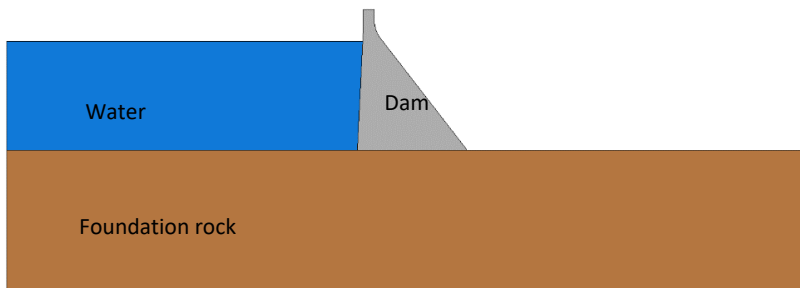


Figure 4.14: FE domains in 2D of the Pine Flat concrete gravity dam, from Paper IV.

4.9 Effect of reservoir level on seismic response of concrete gravity dam

The FE model shown in Figure 4.14 was used to investigate the influence of reservoir depth on the seismic response of the dam. The de-convolved Taft earthquake in the stream direction described in the previous chapter is applied as the effective earthquake forces at the base and sides of the foundation, calculated using an analytical method. From dynamic analysis, the responses of the dam are computed at the heel, point A and crest point C (see Figure 4.13).

Figure 4.15 shows the response spectra of acceleration time histories at the heel and crest of the dam for different reservoir levels. As can be seen from this figure, the maximum acceleration at point A at the heel decreases with increasing water level. The same trend can be seen at the dam crest, but the decrease in acceleration is more pronounced with increasing elevation from 278.6 m to 290.0 m.

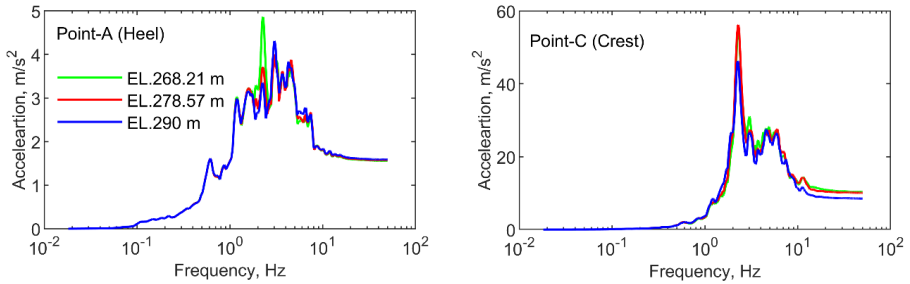


Figure 4.15: Response spectra of acceleration time histories at the heel and crest of the dam for different reservoir levels.

Figure 4.16 shows the time histories of the displacements at the heel and crest of the dam for different reservoir levels. The positive values of the time histories indicate a displacement in the downstream direction. The negative values indicate a displacement in the upstream direction. As can be seen from the figure, the change in reservoir level has no significant effect on the time history of the displacement at the heel. For point C at the crest, a rising water level leads to a decreasing displacement in the upstream direction. A different trend is seen for the displacement in the downstream direction, which may be due to initial static displacement. Figure 4.17 illustrates the hydrodynamic pressure in the reservoir at point A. As can be seen from the figure, there is no clear dependence between hydrodynamic pressure and water level.

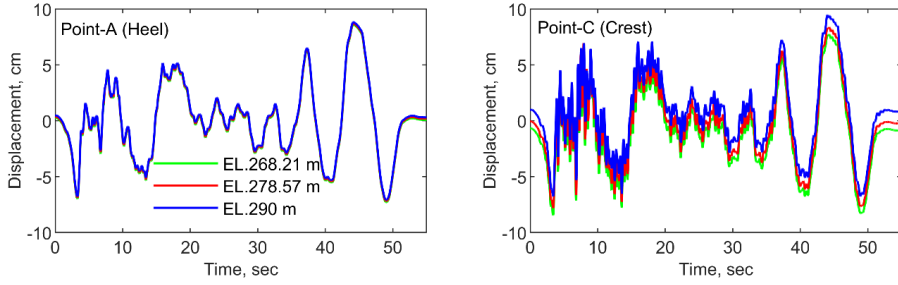


Figure 4.16: Displacement time histories at the heel and crest of the dam for different reservoir levels.

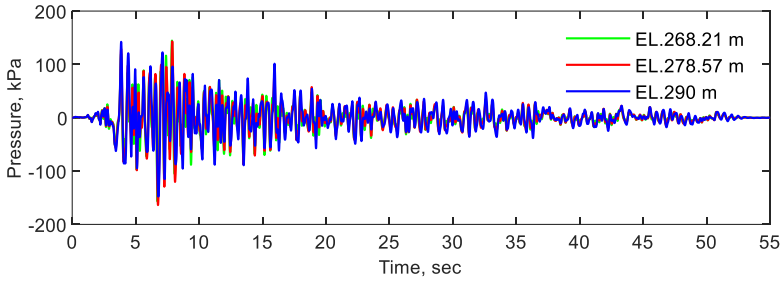


Figure 4.17: Hydrodynamic pressures at the heel for different reservoir levels.

4.10 Numerical example for concrete buttress dam

The concrete buttress dam considered in the following example is representative of a typical large concrete buttress dam in Sweden. There are about 25 concrete buttress dams with similar geometry in Sweden [12]. The example dam is about 100 m long and consists of 13 almost identical concrete monoliths (see Figure 4.18). Each monolith consists of a 2 m-thick and 8 m-wide front plate facing the water and a 40 m-high supporting buttress, 2 m thick and 34 m wide near the bedrock. The upper 10 m of the front plate is vertical, while the lower part is inclined at an angle of 56.3° with respect to the horizontal axis, and the downstream edge of the buttress has an inclination of 68.2° . The crest of the dam, the horizontal upper part of the buttress and front plate, is 4.5 m wide. There is a $2.0 \text{ m} \times 1.5 \text{ m}$ inspection gangway that passes through all buttresses.

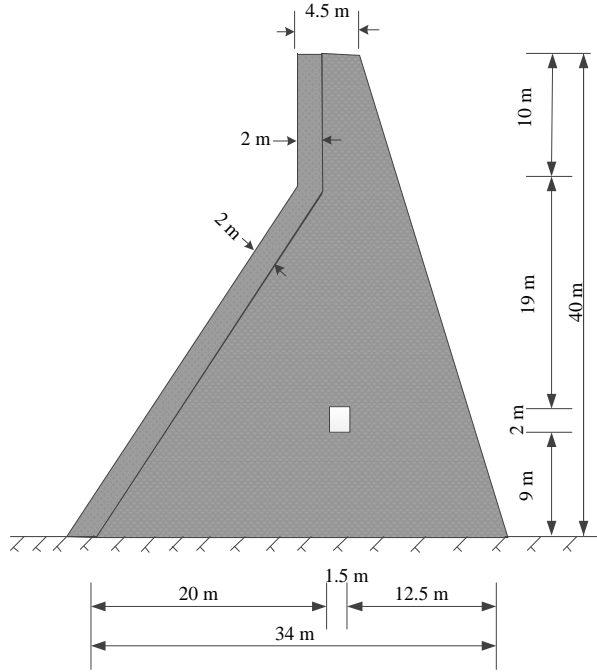


Figure 4.18: Geometry of the concrete monolith, reproduced from [12].

The concrete material has the following parameters: modulus of elasticity $E_s=25$ GPa, density $\rho_s=2400$ kg/m³ and Poisson's ratio $\nu_s=0.2$ [12]. The concrete buttress dam is founded on a rock foundation in a rectangular canyon where the rock material has the following material parameters: $E_f=25$ GPa, density $\rho_f=2400$ kg/m³ and Poisson's ratio $\nu_f=0.2$. For numerical modelling, the elastic modulus and density of hard rock in Sweden are typically between 16-40 GPa and 2500-2800 kg/m³, respectively [13]. The higher limit corresponds to intact rock. The rock foundation of the dam is typically an old riverbed, which is likely to be fractured to some extent, and the rock mass also contains discontinuities. Therefore, the same stiffness is assumed here as for concrete. A viscous damping of 1% and 2% is assumed for the dam and the rock foundation, respectively [102].

In the FE modelling of the concrete buttress dam, the monoliths are discretised by solid elements (C3D8). Contraction joints in the tangential direction have no shear strength and are modelled as frictionless interaction. Joints in the normal direction are modelled by using soft contact constraint when assuming $p_0 = 5$ MPa and $c_0 = 0.1$ mm [70]. The interface between the dam and foundation in the normal direction is modelled using a hard contact constraint with zero tensile strength to allow this joint to open and close. A friction coefficient and slip tolerance of 1 and 0.0001 respectively are used here [70; 132].

Figure 4.19 shows the FE model of the rock foundation for the dam. The FE domain is discretised by 14,355 solid elements. Infinite elements are placed at the side boundaries to prevent seismic waves from reflecting into the FE domain. An acceptance place for infinite elements is obtained by extending the rock foundation to twice the height of the dam, along the lateral sides in the cross-stream direction and from the bottom of the dam (see the convergence analysis in Section 4.11). In the stream direction, the rock foundation is extended to the length of the reservoir. A minimum length of twice the height of the reservoir is recommended. In this case, a reservoir length of 3.5 times the depth is assumed. Therefore, the total size of the foundation is 264 m in the stream and cross-stream direction and 120 m in the vertical direction. A full reservoir with a depth of 38.5 m is considered. The reservoir is discretised with 10,816 acoustic elements (AC3D8), with a non-reflective boundary defined at the upstream end of the reservoir. A tie constraint is used at the interfaces between the water of the reservoir and the foundation of the dam.

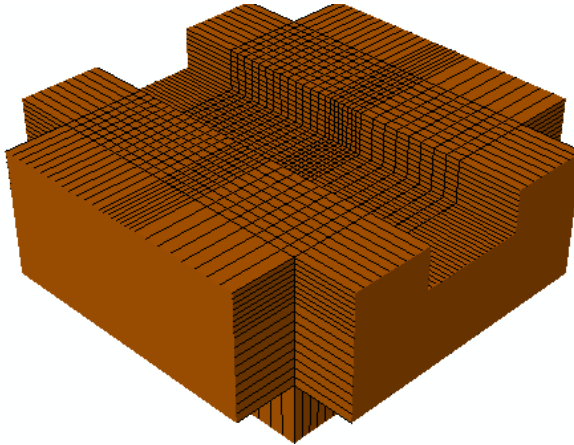


Figure 4.19: FE model of rock foundation for concrete buttress dam.

4.11 Sensitivity analysis for foundation size

To find a suitable place for infinite elements in the cross-stream direction of the dam foundation, a 2D model of a rectangular canyon is analysed under the horizontal (SV -wave) and vertical (P-wave) components of the Swedish design earthquake and the Taft earthquake. The non-reflected boundaries are in the horizontal direction at the distance $n_x H$ from the canyon sides and in the vertical direction at the $n_y H$ distance from the free surface (see Figure 4.20).

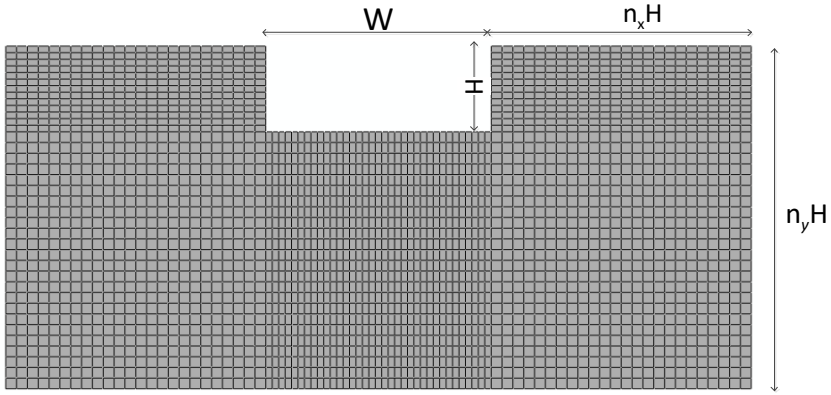
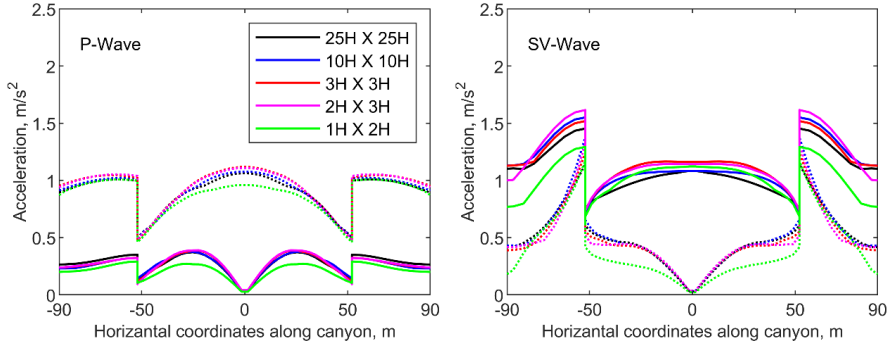


Figure 4.20: FE model of rock foundation with rectangular canyon by $H=40$ m and $W=104$ m.

The analyses are carried out for different combinations of $n_x H \times n_y H$ with $25H \times 25H$, $10H \times 10H$, $3H \times 3H$, $2H \times 3H$ and $1H \times 2H$. Figures 4.21a and 4.21b show the distribution of peak ground acceleration (PGA) along the free surface of the foundation generated by the Swedish design earthquake and the Taft earthquake, respectively.

Figure 4.21a shows that the Swedish design earthquake underestimates the PGA in the canyon due to the small size of $1H \times 2H$. It can also be seen that there is no significant difference between the domain sizes of $3H \times 3H$ and $2H \times 3H$. However, the size of the domains of $3H \times 3H$ and $2H \times 3H$ overestimates the PGA compared to the larger domains. For the Taft earthquake in Figure 4.21b, it can be seen in the canyon that the difference between the PGAs for different domain sizes is insignificant. Thus, increasing the size of the domain is not beneficial. Therefore, in the analyses in Paper V, the domain size of $2H \times 3H$ was chosen, which has acceptable accuracy for both high-frequency and low-frequency excitations compared to the enlarged domains.

(a) Swedish design earthquake



(b) Taft earthquake

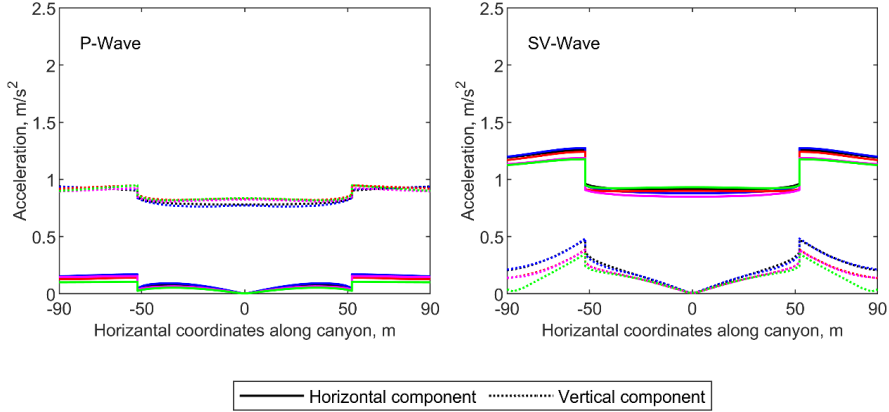


Figure 4.21: Distribution of PGA along the rectangular canyon surface for domain sizes of $25H \times 25H$, $10H \times 10H$, $3H \times 3H$, $2H \times 3H$ and $1H \times 2H$ generated from the (a) the Swedish design earthquake and (b) the Taft earthquake.

CHAPTER 5

Summary of Appended Papers

This chapter contains a summary of the appended papers that have contributed to answering the research questions of this thesis.

Paper I: Abbasiverki, R., Ansell, A., Malm, R., Analysis of shallowly buried reinforced concrete pipelines subjected to earthquake loads. *Nordic Concrete Research* 51, 111-130, 2014.

Paper II: Abbasiverki, R., Ansell, A., Seismic response of large diameter buried concrete pipelines subjected to high frequency earthquake excitations, *Int. J. Structural Engineering*, 10(4), 307-329, 2020.

Paper III: Abbasiverki, R., Malm, R., Ansell, A., Implementation of free-field modelling of foundations for large dam structures exposed to high-frequency vibrations, submitted for review.

Paper IV: Enzell, J., Malm, R., Abbasiverki, R., Ahmed, L., Non-linear behaviour of a concrete gravity dam during seismic excitation, A case study of the Pine Flat Dam, In: *Numerical Analysis of Dams: Proceedings of the 15th ICOLD International Benchmark Workshop*, , Milan, Italy, Springer Nature, 2021.

Paper V: Abbasiverki, R., Malm, R., Ansell, A., Nordström, E., Nonlinear Behaviour of Concrete Buttress Dams under High-Frequency Excitations Taking into Account Topographical Amplifications, *Shock and Vibration*, Vol 2021, Article ID 4944682, 1-22, 2021.

5.1 Paper I: Analysis of shallowly buried reinforced concrete pipelines subjected to earthquake loads

In this paper, two-dimensional FE models were developed to investigate the influence of high-frequency excitations on buried concrete pipelines. Two models were considered: the first model represents the longitudinal cross section of the pipeline, and the second model represents the transverse cross section. It was assumed that the joints have the same properties as the pipe, so that the whole concrete pipeline has continuous properties. The effects of soil stiffness and water mass were studied for two earthquake excitations: the Swedish design earthquake (high-frequency excitation) and the Northridge earthquake (low-frequency excitation). It was shown that the stiffness of the soil has a significant influence on the dynamic characterisation of the soil-pipe system. The dynamic response of concrete pipeline subjected to high-frequency excitation is significantly affected by soil stiffness, with the maximum stresses in the pipeline occurring in stiff soil. The water mass has only a minor influence on the axial stresses, but a greater influence on the bending and ring stresses.

5.2 Paper II: Seismic response of large diameter buried concrete pipelines subjected to high-frequency earthquake excitations

This paper investigates the influence of rock geometry on the response of buried concrete pipelines when subjected to high-frequency excitations. The influence of soil stiffness, burial depth and soil layer thickness is also investigated. The longitudinal plane model described in Paper I was developed taking into account the inclined bedrock and the pipeline joints. The analyses were carried out for the Swedish design earthquake (high-frequency excitation) and the Chi-Chi earthquake (low-frequency excitation). It was shown that inclined bedrock causes critical stress conditions in the pipelines for both earthquake excitations. Increasing the soil stiffness and considering inclined rock resulted in a stress increase that was higher for high-frequency excitation. Inclined bedrock reduces the safety of the concrete pipeline, especially due to bending deformations in the pipe and in the joints of the pipeline. The safety against high-frequency damage was more than ten times higher than the assumed tensile strength for all soil types considered in uniform soil. When pipe joints were considered, the safety was reduced to three times due to axial tensile failure at the joints. For the inclined bedrock, this safety was reduced to about three times the tensile strength in the pipeline barrel and 1.5 times the tensile strength in the pipe joints. With increasing installation depth, the ring stresses increased. However, the risk of pipeline failure due to local cross-sectional damage within the pipe segments was low. The thickness of the soil layer influenced the bending stresses induced by high-frequency excitation. Decreasing thickness of the soil layer reduces the safety of the pipeline.

5.3 Paper III: Implementation of free-field modelling of foundations for large dam structures exposed to high-frequency vibrations

This paper investigates the implementation of free-field modelling to describe vibrations at dam foundations in the presence of high-frequency excitations. Two methods for free-field modelling of dam foundations are presented: 1) the direct FE method and 2) the analytical method. A rock foundation with semi-cylindrical canyon is considered for the study. First, verification analyses were performed for vertical harmonic P-, SV- and SH- waves with unit amplitude and frequency f . It was shown that the free-field modelling based on the direct FE method accurately calculates the topographic amplification due to high-frequency excitation. However, the analytical method is not accurate for all frequencies and wave types. In order to consider different frequency ranges in the analyses, the topographic amplification due to earthquake excitations was determined. Two groups of earthquakes with low- and high-frequency content were considered. The topographic amplification was also calculated using other simplified methods popular in dam design: the massless method and neglecting the effective forces at the lateral boundaries. Here, the direct FE method was used as a reference solution. The analytical method has been shown to produce errors at high-frequency excitations. The massless method produces significant errors in the rock surface motion due to high-frequency excitations. Ignoring the effective forces at the lateral boundaries leads to energy losses and underestimates the surface motions. For high-frequency excitations, the energy loss was less than for low-frequency excitations.

5.4 Paper IV: Non-linear behaviour of a concrete gravity dam during seismic excitation: a case study of the Pine Flat Dam

In this paper, a 2D model of the Pine Flat concrete gravity dam was used to investigate considerations to be made in numerical modelling of rock foundations in free vibration and dynamic analysis of a concrete gravity dam. It was shown that the natural frequencies obtained from FE analysis using mass and massless foundation models agree well with the measured frequencies. The advantage of using a massless foundation was that the non-structural modes originating from the rock mass were removed.

Wave propagation in the rock foundation was investigated for low- and high-frequency impulsive excitation. The effects of considering and neglecting the effective earthquake forces at the lateral boundaries were investigated. The effective earthquake forces were calculated using an analytical method. When free-field conditions were used, the velocity along the surface was more or less identical, which is a clear indication that the implementation of free-field input data at the boundaries works as intended. Neglecting the lateral forces, on the other hand, resulted in significant differences in the velocity along the surface. A linear dynamic analysis of the dam-water-foundation system due to the Taft earthquake was performed. The analyses were performed for a massless foundation and a mass foundation considering and neglecting the effective earthquake forces at the lateral boundaries. The massless approach provided accurate displacements at the base of the dam,

but overestimated the accelerations in the dam compared to the more realistic case with mass foundation. Neglecting the lateral forces, on the other hand, resulted in an underestimated displacement at the upstream heel of the dam.

5.5 Paper V: Nonlinear Behaviour of Concrete Buttress Dams under High-Frequency Excitations Taking into Account Topographical Amplifications

The fifth paper investigates how high-frequency excitations affect the structural response of a concrete buttress dam. First, the dynamic characterisation of a concrete dam was investigated. Then, the dynamic response of the dam to vibrations in the stream direction was calculated and compared with the case where vibrations in the stream and cross-stream directions were considered. The response to low-frequency excitations was also compared with high-frequency excitations. The non-linear effect of contraction joints was also included in the dynamic analyses. However, in the linear free vibration analysis, this effect was taken into account by modelling the joints with hinges. It was found that the natural frequency of the concrete buttress dam was relatively high. High natural frequencies resulted in a higher amplification of acceleration between the dam crest and the dam base with high-frequency excitation than with low-frequency excitation. The free vibration analysis of the monoliths revealed two types of bending modes: lateral bending and bending in the stream direction. The lateral bending modes had higher natural frequencies. Therefore, the inclusion of vibrations in the cross-stream direction led to an increase in the stresses in the monoliths. This increase due to the high-frequency excitation was higher than that due to the low-frequency excitation.

Due to the importance of free-field modelling of the foundation for high-frequency excitations, the dynamic response of the dam was compared for different free-field modelling approaches using the direct FE method, the analytical method and the massless approach. The calculated dynamic response of the dam was significantly influenced by the free-field modelling approach used for the foundation. The results underline the importance of using an accurate foundation modelling approach, especially in cases where non-linearity is considered. The analytical method resulted in unreliable joint openings, while the massless method gave unreliable results, especially for high-frequency excitations.

CHAPTER 6

Results and Discussion

In this study, first, frequency analyses were performed to investigate the mechanical properties of the FE models. The models were then subjected to earthquakes with different frequency contents in order to study the dynamic response. The following sections describe the results and discuss the numerical examples presented in Papers I-V which have contributed to answering the research questions of this thesis.

6.1 Effective two-dimensional FE models for underground pipelines

Underground pipelines are long tubular structures. In three-dimensional FE analysis of such systems, it is computationally intensive to simulate the propagation of high-frequency waves in the soil-pipe system. Since high-frequency excitations have a shorter wavelength than low-frequency excitations (see Eq. (2.24)), a finer element size is required to capture high-frequency waves, resulting in a large number of degrees of freedom that increase the computational cost. Therefore, in Papers I and II, the use of two-dimensional plain strain models was evaluated. The models effectively consider the behaviour of the pipeline in the longitudinal and cross-sectional planes. The axial and bending stresses are obtained from a model for the longitudinal plane and the ring stresses from a model for the cross-sectional plane. These models can also be further developed to include details of the geological conditions; for example, the geometry of irregular bedrock as considered in the examples in Paper II.

The dynamic characterisation of the soil-pipeline system was investigated by eigenvalue analysis and the results were presented as cumulative effective mass. Figure 6.1 shows the comparison between the effective mass for the models of the longitudinal plane section with 25 m and 12 m soil layer thickness. Three levels of soil stiffness were considered: loose, medium and dense. For the model with 25 m soil layer thickness, the dominant natural frequencies for dense, medium and loose soil are 8.59 Hz, 4.08 Hz and 1.27 Hz, respectively. For the model with a soil layer thickness of 12 m, the corresponding frequencies are 17.61 Hz, 9.80 Hz and 2.34 Hz. It can be seen that the dynamic characterisation of the soil-pipeline system is significantly influenced by the stiffness of the soil. The highest natural frequencies correspond to a dense soil. The predominant frequency is almost twice as high for a soil layer

thickness of 12 m as for 25 m soil. This is due to the inverse relationship between the natural frequency of the soil deposit and the thickness of the soil layer [93]:

$$\omega_n = \frac{V_s}{H} \left(\frac{\pi}{2} + n\pi \right) \quad n = 0, 1, 2, \dots, \infty \quad (6.1)$$

Thus, for underground structures dominated by stiffness, the dynamic characterisation of the soil-structure system is significantly influenced by the stiffness of the soil. The thickness of the soil layer also has a significant influence on the natural frequency content of the soil-pipeline system.

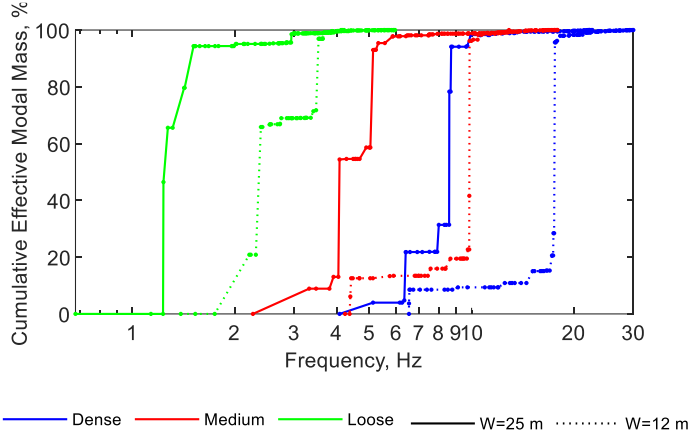


Figure 6.1: Cumulative effective modal mass for the longitudinal plane models with 25 m and 12 m soil layer thickness.

The dynamic response of pipelines is described by the maximum tensile stress. For the longitudinal plane section model, the maximum axial tensile stress and the maximum bending tensile stress are calculated. For the cross-section model, the maximum principal tensile stress is calculated. The influences of soil layer thickness and pipeline installation depth were investigated in Paper II. Figures 6.2 and 6.3 show the influence of soil layer thickness and installation depth on the maximum axial, bending and ring stresses of the concrete pipeline from the Swedish design earthquake and the Chi-Chi earthquake, respectively.

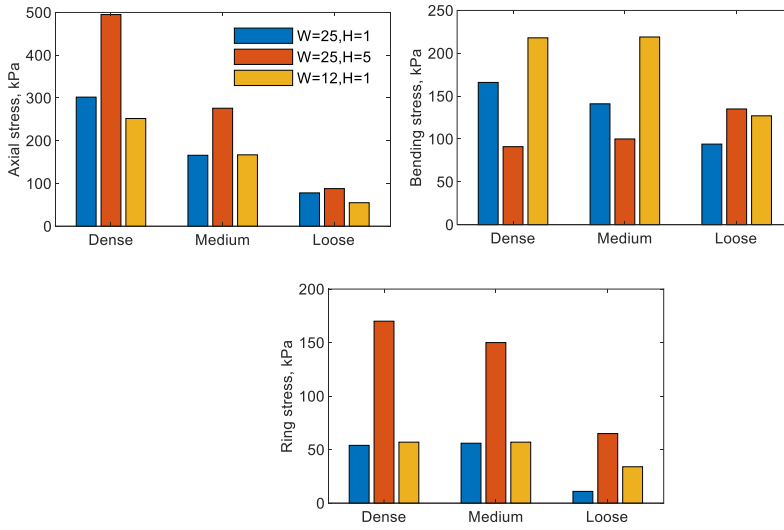


Figure 6.2: The maximum axial, bending and ring stresses developed in a concrete pipeline due to the Swedish design earthquake for the models with a soil layer thickness of $W=25$ m and $W=12$ m and a burial depth of $H=1$ m and $H=5$ m.

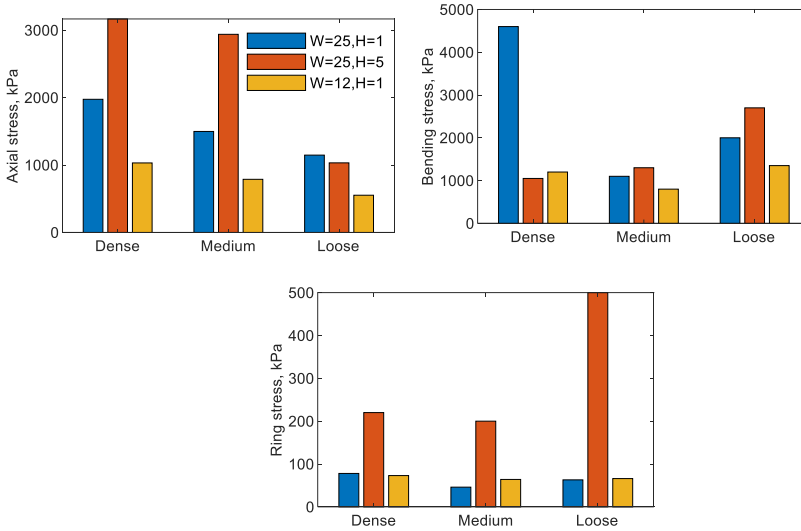


Figure 6.3: The maximum axial, bending and ring stresses developed in a concrete pipeline as a result of the Chi-Chi earthquake for the models with soil layer thickness of $W=25$ m and $W=12$ m and a burial depth of $H=1$ m and $H=5$ m.

Figure 6.2 shows that a decrease in the thickness of the soil layer from $W=25$ m to $W=12$ m increases the bending stresses due to the high-frequency excitation. The maximum bending stresses of the pipeline with 12 m soil layer thickness in dense, medium and loose soil are 1.30, 1.50 and 1.35 times, respectively, that of the cases with 25 m soil layer thickness, but for the low-frequency excitation in Figure 6.3, they are 0.26, 0.72 and 0.67. Figure 6.2 also shows that as the depth of the pipeline increases from $H=1$ m to $H=5$ m, the axial and ring stresses caused by the high-frequency excitation increase, with the effect on the ring stress being greater than the axial stress. In dense, medium and loose soil, the ring stresses in the pipeline at a laying depth of 5 m are 3.0, 2.6 and 6.0 times higher, respectively, than at a laying depth of 1 m. For low-frequency excitation, increasing burial depth increased the ring stresses, being 2.8, 4.3 and 8.0 times for dense, medium and loose soil. Therefore, the concrete pipelines are susceptible to bending deformations under high-frequency excitation when the thickness of the soil layer decreases and the burial depth increases.

In Paper I, the influence of water mass on seismic response of concrete pipelines was investigated. Table 6.1 shows this influence on the maximum tensile stresses induced in the concrete pipelines from the Swedish design earthquake and the Northridge earthquake [127]. Table 6.1 shows that the inclusion of the water mass has a relatively small effect on the amplification of the axial stresses generated by the high-frequency excitation. On the other hand, it has a greater influence on the bending and ring stresses of the pipeline. The reason for this could be the lower stiffness of the concrete pipeline during bending deformations. The maximum amplification factor of 2 was determined for the bending and ring stresses in dense soil. For the low-frequency excitation, a maximum amplification of 1.5 was determined for the bending and ring stresses in the medium soil. Therefore, the water mass may reduce the safety of the pipeline in stiff soil due to bending deformations.

Table 6.1: The influence of water mass on the maximum tensile stress induced in concrete pipelines from the Swedish design earthquake and the Northridge earthquake.

Soil type		Axial stress (kPa)		Bending stress (kPa)		Ring stress (kPa)	
		Sweden	Northridge	Sweden	Northridge	Sweden	Northridge
Medium soil	With water	150	1350	190	900	58	62
	Without water	155	1600	120	600	55	40
	Amplification factor	0.96	0.84	1.58	1.50	1.05	1.55
Dense soil	With water	320	1300	320	600	110	2500
	Without water	300	1550	150	610	55	4000
	Amplification factor	1.06	0.83	2.13	0.98	2.00	0.62

In Paper II, the influence of the joints was investigated. Figures 6.4a and 6.4b show the maximum axial and bending stresses that occur in the continuous and segmented pipeline models with a soil layer thickness of 25 m and a burial depth of 1 m for the Swedish design earthquake and the Chi-Chi earthquake, respectively. It can be seen that considering the joints in the pipeline reduces the stresses in both excitations. This is because the relative displacement at the pipe joints accommodates the ground strain induced by seismic waves along the segmented pipelines [145]. It can also be seen in the figures that the influence on the bending stresses is greater than the axial stresses. However, the joints are critical parts of the mechanical system that reduce the safety of the concrete pipeline. In Paper II, it was shown that for a continuous pipeline with uniform bedrock geometry, the safety from high-frequency damage is about ten times the assumed tensile strength, while this was reduced to three times when the pipe joints were considered due to axial tensile failure at the joints.

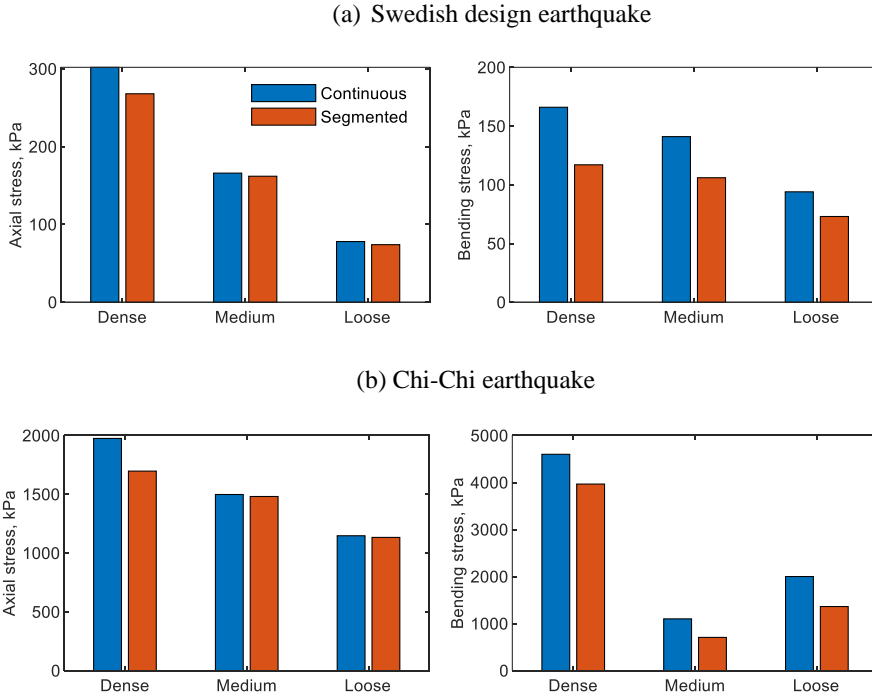


Figure 6.4: Comparison between the maximum axial and bending stresses in continuous and segmented pipelines with $W=25$ m, $H=1$ m generated by (a) the Swedish design and (b) the Chi-Chi earthquake.

It is shown that a two-dimensional model can effectively account for the axial and bending deformations in the pipeline. The most important aspect of the models is the capture of bending deformations in the concrete pipeline, as these structures are vulnerable in this respect. As described in Section 2.5.2, there are different methods for modelling seismic sources. For the two-dimensional models, a method that uses only non-reflective boundary

conditions was used. As shown in Paper III, the errors using this method were lower for high-frequency excitations than for low-frequency contents, but it is recommended to improve two-dimensional models by considering effective earthquake forces at the lateral boundaries.

6.2 Influence of rock geometry variations on buried concrete pipelines

Underground pipelines generally cross large areas with varying geological conditions. Damage to buried pipelines often occurs in areas with irregular topography [10; 87; 98; 151]. The influence of inclined bedrock on the propagation of high-frequency waves and thus on concrete pipelines was investigated in Paper II. A two-dimensional longitudinal plane model from Paper I was implemented to account for variations in bedrock geometry. According to the work of O'Rourke and Liu [122] on the effects of variable subsurface conditions, the maximum soil strain occurs at a slope angle of 45° . Therefore, for $\theta > 45^\circ$, the soil strain is assumed to be the value corresponding to an angle of inclination of 45° . In this paper, an angle of inclination of 45° was chosen, but $\theta = 90^\circ$ was also investigated for comparison. Paper II also showed an insignificant difference between the 45° inclination angle and the 90° inclination angle.

Inclined rock affects the dynamic characterisation of the soil-pipeline system. Figure 6.5 shows the comparison between the cumulative effective modal mass for the longitudinal plane section models with uniform rock and inclined bedrock $\theta=45^\circ$. It can be seen that considering inclined bedrock results in active higher free vibration modes than with uniform rock, and this effect is more pronounced for dense soil. Therefore, for concrete pipelines installed in regions with hard rock, it is important to investigate how high-frequency excitations can affect the response of concrete pipelines depending on the geological conditions.

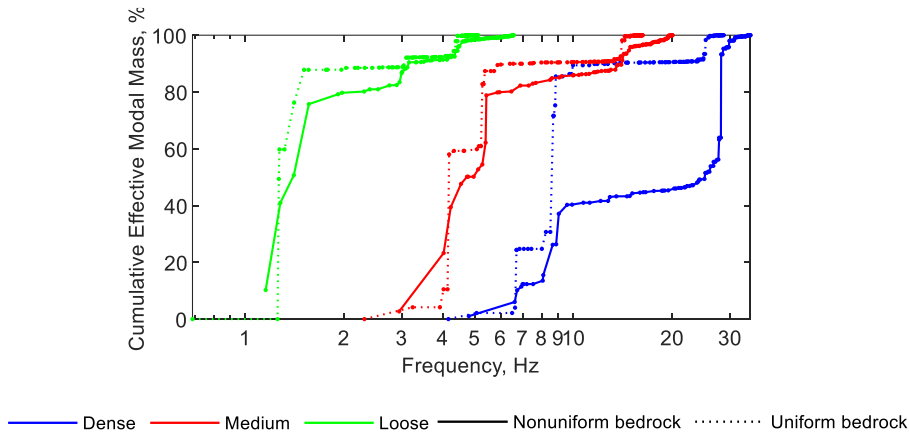


Figure 6.5: Cumulative effective modal mass for the longitudinal models, taking into account the joint effect. For the model with uniform bedrock and 25 m soil layer thickness and inclined bedrock $\theta=45^\circ$.

The dynamic response is presented here in terms of stress envelopes, i.e., the maximum tensile stress at each section of the pipelines reached during the analysis period. Figures 6.6a and 6.6b show the comparison of the axial stresses for the longitudinal models with uniform and inclined bedrock generated from the Swedish design earthquake and the Chi-Chi earthquake, respectively. Figures 6.7a and 6.7b show the comparison between the bending stresses of the longitudinal models of uniform and inclined bedrock, from the Swedish design earthquake and the Chi-Chi earthquake, respectively.

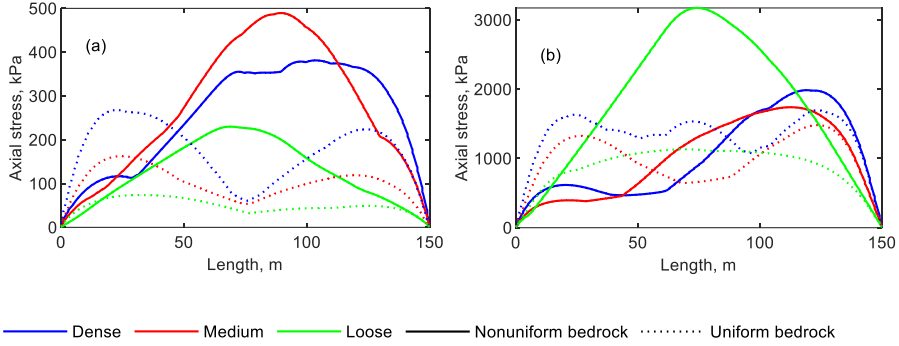


Figure 6.6: Effect of the inclined bedrock on the axial stress for the longitudinal plane section model with consideration of the joint effect. From (a) the Swedish design earthquake and (b) the Chi-Chi earthquake.

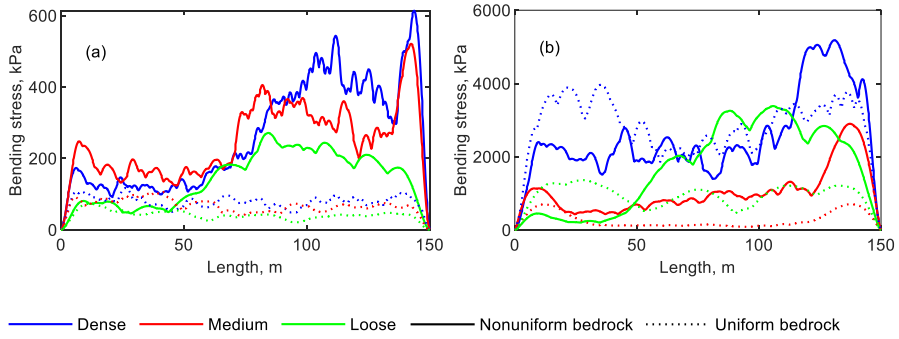


Figure 6.7: Effect of the inclined bedrock on the bending stress for the longitudinal plane section model with consideration of the joint effect. From (a) the Swedish design earthquake and (b) the Chi-Chi earthquake.

Figure 6.6a shows that for high-frequency excitation, the maximum axial stress generated in a model with an inclined bedrock is 3.1, 3.0 and 1.4 times the stress of a uniform ground for loose, medium and dense soils, respectively. For low-frequency excitation, the amplifications are 2.80, 1.18 and 1.17 (see Figure 6.6b). It can be seen that the stresses are concentrated around the slope for non-uniform ground, which was also observed by [10; 152]. For the

bending stresses generated by the high-frequency excitation in Figure 6.7a, the maximum bending stress generated by the high-frequency excitation in a model with inclined bedrock is 3.7, 4.9 and 5.2 times that of the uniform ground for loose, medium and dense soils, respectively. The amplification of the bending stress for low-frequency excitation is 2.4, 4.1 and 1.3 times, respectively (see Figure 6.7b). Thus, for high-frequency excitations, there is a significant amplification of stresses between non-uniform and uniform soils, where the higher stresses occur due to the inclined bedrock. The amplifications occur for both axial and bending stresses.

Figure 6.8 shows the maximum axial stresses in the pipeline joints in the uniform and non-uniform bedrock caused by the Swedish design earthquake. The maximum bending stresses in the joints are shown in Figure 6.9.

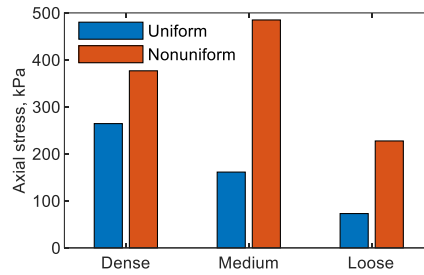


Figure 6.8: Comparison between the maximum axial tensile stress in the pipeline joints in uniform and non-uniform bedrock. From the Swedish design earthquake.

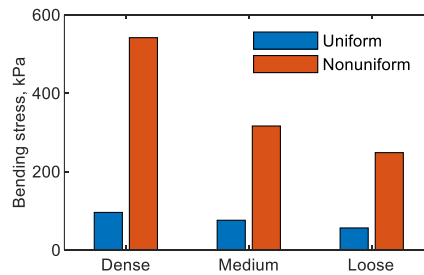


Figure 6.9: Comparison between the maximum bending tensile stress in the pipeline joints in uniform and non-uniform bedrock. From the Swedish design earthquake.

It can be seen from Figures 6.8 and 6.9 that the safety due to tensile failure in the joints was significantly reduced because of the inclined rock. Considering a characteristic tensile strength of the cement mortar as 0.76 MPa, the maximum axial tensile stresses experienced in the joints of the pipeline in dense, medium and loose soil are 50%, 60% and 30% of the tensile strength of the cement mortar, respectively (see Figure 6.8). For the bending stresses, they are 70%, 40% and 30% respectively (see Figure 6.9). The maximum axial and bending

stresses in the joints occurred at the joints connected to pipe segments with high stress. It can thus be seen that different soil depths along the pipeline reduce the safety of the concrete pipeline, especially due to bending deformations in the pipeline barrel and joints. Compared to the parameters studied with uniform rock geometry, there were critical stress conditions for pipelines in non-uniform ground. The models with non-uniform ground did not consider the effects of water mass or burial depth, which reduce safety due to bending deformations. Therefore, the inclusion of the above parameters and consideration of geological conditions reduce the safety of concrete pipelines. Due to the significant influence of inclined bedrock, it is recommended that special attention be paid to other irregularities in the ground, such as rock outcrops.

6.3 Implementation of free-field modelling of dam foundations

Concrete dams are commonly founded on an irregular rock surface. Previous numerical and analytical studies have shown that the irregular surface topography and frequency of excitation can have a significant effect on the wave patterns at a given site [157; 164]. One of the major challenges in numerical modelling of seismic wave propagation in dam foundations is the modelling of the foundation free field. Section 2.5.2 presented a method for seismic source modelling. The influence of implementing different approaches to modelling seismic source on the motion of the free surface of the rock foundation was studied in Papers III-V. Figure 6.10 shows the distribution of surface displacement amplitudes along the free surface of the 2D FE model of a semi-cylindrical canyon. The foundation is excited by vertical harmonic P- and SV- waves with unit amplitude and frequency f . Four dimensionless frequencies $\eta = 2fR/V_s = 0.5, 1.0, 1.5, 2.0$ were chosen, where R is the canyon radius. The surface motion of the rock is determined by free-field modelling of the foundation using the direct FE method and the analytical method. The numerical results obtained by Wong [164] are used for comparison. It is found that for the two-dimensional foundation, the difference between the surface motions obtained by the direct FE method and by the analytical method for both SV- and P-waves is insignificant. The reason is that for the two-dimensional model, both the direct FE method and the analytical method calculate the effective earthquake forces based on the 1D column. In Paper III, it was shown that the free-field modelling with the direct FE method accurately calculates the motion of the free surface of the 3D foundation with semi-cylindrical canyon due to SH-, SV- and P-waves. This is because this method obtains the effective earthquake forces at the absorbing boundaries from the free-field system, which is identical to the actual system in the area outside the non-reflected boundaries. The effective earthquake forces were determined by the direct FE method using auxiliary analyses of a 1D column and a 2D system. In the analytical method, where the free-field system is simplified to a one-dimensional column and the effective earthquake forces are calculated analytically, errors occur, especially due to SV- and P-wave excitations. Therefore, for the three-dimensional foundations with irregular surface topography, the direct FE method accurately calculates the topographic amplifications.

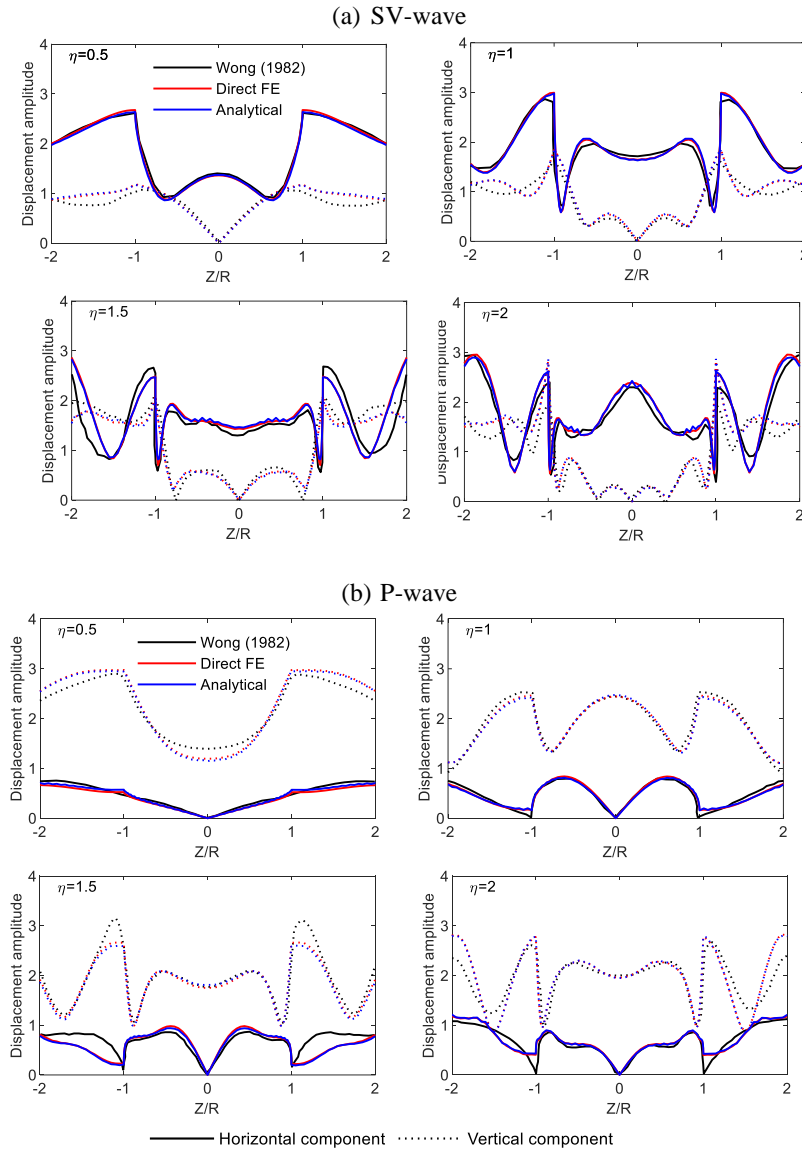


Figure 6.10: Surface displacement amplitudes for incident plane SV- and P- waves with dimensionless frequencies of $\eta = 0.5, 1.0, 1.5$ and 2.0 in a 2D FE model of the semi-cylindrical canyon foundation calculated by the direct FE method and the analytical method, compared with results from Wong [164]. The responses are plotted against the dimensionless distance Z/R , where Z is the distance in the transverse direction from the centre and R is the radius.

Figures 6.11a and 6.11b show the response spectra of the time history of acceleration at the centre of the semi-cylindrical canyon considered in Paper III caused by the LaMalbaie and

Livermore earthquakes [127], respectively. The responses are calculated by the foundation modelling approaches using the massless method, the direct FE method, the analytical method and exclusion of the lateral effective forces. Taking the direct FE method as a reference solution, the error tolerance of the different methods is calculated.

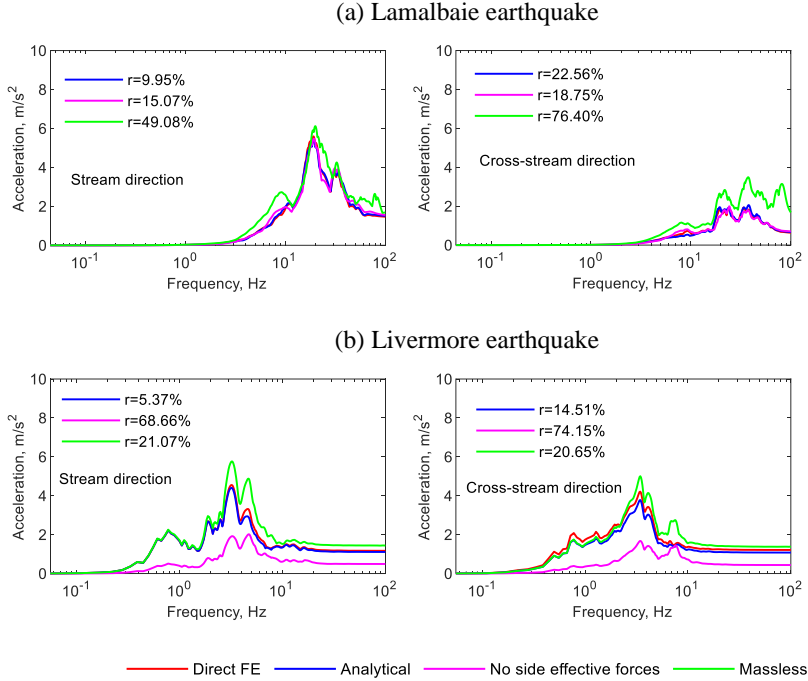


Figure 6.11: Response spectra of the acceleration time history in the centre of the semi-cylindrical canyon in the stream and cross-stream directions caused by (a) the Lamalbaie earthquake and (b) the Livermore earthquake. The responses are calculated by the foundation modelling approaches using the massless, direct FE, analytical and no lateral effective forces methods. The error tolerance r was calculated using the direct FE method as a reference solution.

As shown in Figure 6.11a, for the high-frequency excitation, the maximum errors of 22.56%, 18.75% and 76.40% were produced by the analytical method, the method excluding lateral effective forces and the massless method, respectively. For the low-frequency excitation in Figure 6.11b, the maximum errors of 14.51%, 74.15% and 21.07% were generated by the analytical method, the method excluding lateral effective forces and the massless method, respectively. It can be seen that the massless method produces a significant error for the high-frequency excitation. In Paper III, the distribution of the maximum acceleration and the corresponding error tolerance along the foundation surface were shown. A high error tolerance was found for higher-frequency excitations with the massless foundation modelling approach. For the high-frequency excitations, a maximum error tolerance of 130% was determined. For excitations with lower frequencies, the maximum error tolerance was 40%.

A significant error introduced by the massless method for the high-frequency excitations is due to the fact that the recorded motions at the foundation surface due to high-frequency excitations are non-uniform compared to the low-frequency excitations. This behaviour cannot be captured when modelling the foundation using a massless approach. This approach neglects topographic amplifications and the free surface motion is identical for all points. This leads to a high error tolerance for excitations with higher frequency. Modelling the foundation mass by excluding lateral effective forces leads to significant errors for low-frequency excitations due to energy leakage.

It was shown that the errors are lower when the foundation mass and the free-field modelling by the analytical method are taken into account than with the massless method. However, the errors for the analytical method are above the acceptance criterion of 5%. The errors for the high-frequency excitation are greater than for the low-frequency excitation. In Paper III, it was shown that the errors for the high-frequency excitations are between 8-45%. Paper V also investigated the influence of the free-field modelling method on the calculation of the free rock surface motion in a rectangular canyon. Figures 6.12a and 6.12b show the distribution of error tolerance along the rectangular canyon generated by the analytical and massless methods due to the Swedish design earthquake and the Taft earthquake, respectively.

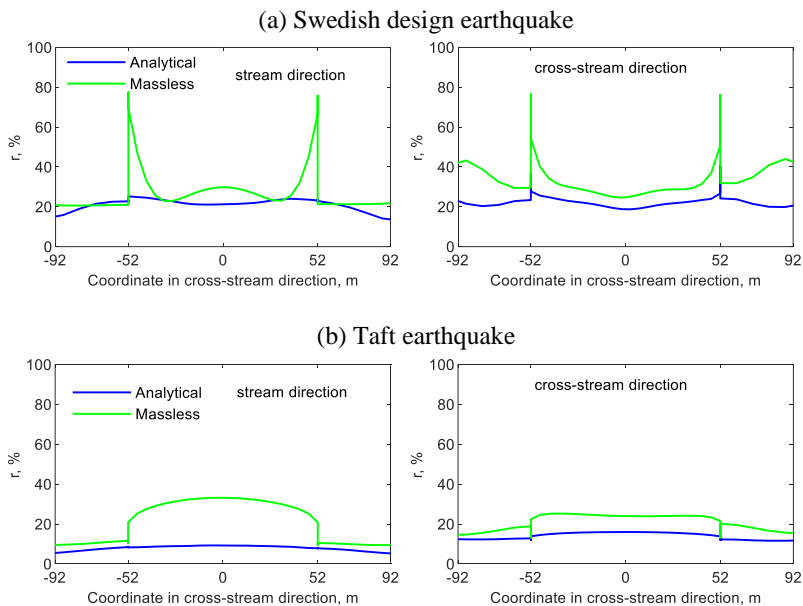


Figure 6.12: Distribution of error tolerance along a rectangular canyon in the stream and cross-stream directions determined by the analytical and massless methods, from (a) the Swedish design earthquake and (b) the Taft earthquake.

For the high-frequency excitation in Figure 6.12a, it can be seen that the foundation modelling with the massless method gives an error between 20-80%, and for the analytical method between 14-32%. For the low-frequency excitation, the errors are between 10-33% for the massless method and 5-16% for the analytical method (see Figure 6.12b). The comparison between the results of the high-frequency and low-frequency excitation shows that the massless method produces significant errors in the high-frequency excitation compared to the low-frequency excitation. This is due to the non-uniform surface motion produced by the high-frequency excitation (see Paper V). The errors for the analytical method are also higher for the high-frequency excitation than for the low-frequency excitation. The errors for the analytical method are lower than for the massless method, still exceed the acceptance criterion of 5%.

The results obtained from examples of foundations with irregular surface topography in Papers III and V show that the massless method produces significant errors, especially for high-frequency excitations. It should be noted that for foundations with a uniform surface, such as the 2D FE model of the foundation in Paper IV, there are no amplifications due to irregularities on the surface. Consequently, the motion of the free surface is the same for the massless method and the methods considering the foundation mass and the effective earthquake forces. In the analytical method, where the free-field system is simplified to a one-dimensional column and the effective earthquake forces are calculated analytically, errors occur especially for high-frequency excitations. Therefore, for high-frequency excitations, it is important to implement an accurate foundation modelling procedure that uses free-field modelling by the direct FE method to capture topographic amplifications. It is worth noting that the bedrock considered in the analyses is homogeneous. Therefore, non-linearities, such as those created by sliding rock fractures, are neglected. This is expected to affect the foundation surface motions and may increase the errors obtained by simplified rock foundation modelling methods. However, the influence of the non-linearity of the dam was investigated in Paper V. It was found that simplified foundation modelling methods cannot reliably capture the non-linear behaviour of the dam.

6.4 Implementation of 2D and 3D FE models (concrete gravity dams)

Relatively long and straight concrete gravity dams are usually represented with a 2D FE model. However, for curved gravity dams and those built in narrow canyons, 3D models are usually required [69]. For a concrete buttress dam, which is a lighter version of the gravity dam, 3D FE modelling is required because the dam responds weakly to cross-stream vibrations due to its slenderness. This was investigated in Paper V. In Paper IV, the Pine Flat gravity dam was investigated using a 2D FE model. It was shown that a 2D FE model can capture the natural frequencies that agree well with the results obtained from field testing. During field tests, six modes of vibration were excited [131]. Figure 6.13 shows the natural frequency and normalised mode shapes on the upstream side of the dam obtained from free vibration analysis for the first six mode shapes.

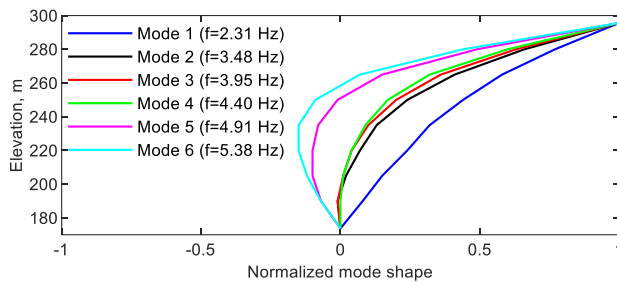


Figure 6.13: Normalised mode shapes for the six lowest modes of the 2D FE model of the Pine Flat gravity dam.

As seen from Figure 6.13, a 2D FE model gives similar mode shapes for the different modes. However, the experiments showed that the modes have different mode shapes [131]. Harrison and Nöjd [79] investigated a comparison between 2D and 3D FE models for the dynamic characterisation of concrete gravity dams. It was found that the 3D FE model is the most effective method for determining the dynamic characterisations of a dam. This is because the 3D FE model captures the mode shapes of the dam accurately. The influence of the mass and massless foundation modelling on the calculated dynamic characterisation of the dam was investigated in Paper IV. There were slight differences between the natural frequencies obtained with the mass model and the massless model of the foundation. However, the advantage of using a massless foundation is that all non-structural modes emanating from the rock mass are suppressed and therefore post-processing is much easier than with the mass model.

In Paper IV, a 2D FE model was implemented and the sensitivity of the calculated response of a concrete gravity dam in relation to the foundation modelling approach was investigated. The seismic response of a concrete gravity dam was calculated based on stream vibrations. Free-field modelling of the foundation was performed using an analytical method. The results were then compared with the massless method and with neglecting the effective earthquake forces at the absorbing boundaries. The sensitivity of the dam response with respect to the foundation modelling approach was investigated by linear analysis. Table 6.2 shows the peak acceleration at the heel and crest and the amplification factor from different free-field modelling approaches.

Table 6.2: Peak acceleration at the heel and crest of the concrete gravity dam and amplification factor.

		Massless foundation	Mass foundation		
			Analytical	Direct FE*	Without free field BCs
Peak acceleration (m/s ²)	Heel	2.10	1.47	1.47	1.30
	Crest	23.20	10.20	10.10	7.30
Amplification factor	-	11.04	6.93	6.90	5.61

* Computed in [79]

As shown in Table 6.2, modelling the mass foundation using the analytical and direct FE methods results in a similar amplification factor between the heel and crest, but neglecting the effective earthquake forces at the lateral boundaries of the foundation leads to an underestimation of the dam response. The massless method overestimates the responses with a 60% higher amplification factor than the cases with mass foundation and considering free-field boundary conditions. Therefore, the mass foundation modelling approach based on the analytical and direct FE methods reliably calculates the dam response.

Figure 6.14 illustrates the comparison between the response spectra of the acceleration time histories at the heel and crest of the dam and the record of the free surface of the foundation due to the Taft earthquake. It can be seen that at the base of the dam, at frequencies above 2 Hz, there are differences between the dam response and the record at the free surface, showing the influence of the dam-reservoir system. As seismic waves propagate towards the dam crest, a frequency interval of 2-6 Hz is amplified. The first peak in the response spectra has a frequency of 2.3 Hz, which corresponds to the first mode of the dam (see Figure 6.13).

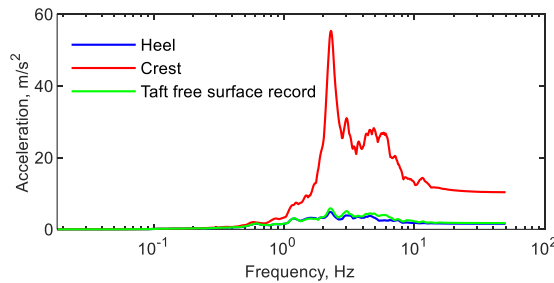


Figure 6.14: Response spectra of acceleration time history at the heel and crest and the free surface of the foundation due to the Taft earthquake.

Harrison and Nöjd [79] studied the response of a dam to low-frequency and high-frequency impulsive loading. The characterisation frequency of the low-frequency impulsive loading was 4 Hz and that of the high-frequency 40 Hz. Table 6.3 shows the amplification factor between the dam crest and the heel due to the impulsive loading. It can be seen that the amplification factor for the low-frequency impulsive loading is about 8.5, while for the high-frequency loading it is about 2. Thus, due to the lower natural frequencies of the dam, a higher amplification factor occurred for the low-frequency load compared to the high-frequency load. Table 6.3 also shows that the direct FE method and the analytical method give similar results. The massless method overestimates the dam's response to low-frequency impulsive loading, as its amplification factor is about 20% higher than in cases where the foundation mass is taken into account. For high-frequency loading, the amplification factor is about 43% higher than in cases where the mass is taken into account. However, in this case Harrison and Nöjd [79] found that the massless method underestimates the responses.

Table 6.3: Amplification factor between the dam crest and the heel due to impulsive loading [79].

	Massless	Analytical	Direct FE method
Low-frequency	10.1	8.5	8.4
High-frequency	3.0	2.1	2.1

It can thus be seen that concrete gravity dams are significantly affected by low-frequency excitations due to their low natural frequencies. For a linear 2D FE model, the foundation mass provides reliable results using both the direct FE and analytical methods compared to the massless method. However, the non-linear effect associated with the foundation and dam could influence the differences between the methods. Consideration of three-dimensional effects, such as the non-linear behaviour of contraction joints, could also affect the results of the different foundation modelling methods. This was investigated in Paper V for a concrete buttress dam.

6.5 Stiffness-dominated concrete structures on the ground (buttress dams)

In Paper V, the non-linear behaviour of a typical concrete buttress dam was investigated with respect to variations in dominant load frequencies. Figure 6.15 shows the bending mode shapes for the buttress monoliths. There are two types of bending modes for the monoliths of the dam, namely lateral bending and bending in the stream direction. The natural frequencies of a typical buttress dam considered here are above 6 Hz. This is much higher than a concrete gravity dam. At Pine Flat, for example, the first six modes were below 6 Hz. Concrete buttress dams are a stiffness-dominated concrete structure due to their slenderness. This results in higher natural frequencies compared to a concrete gravity dam where mass is the primary concern.

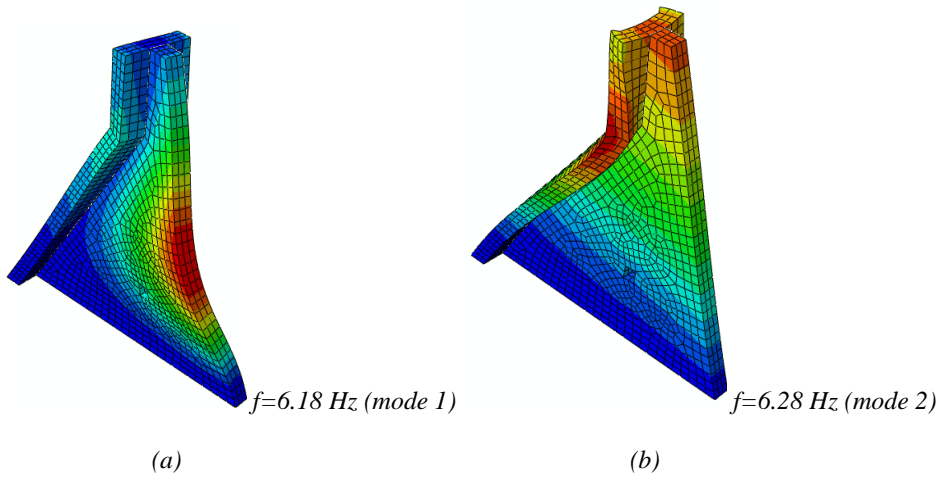


Figure 6.15: Bending mode shapes for the central monolith: (a) lateral bending mode shape and (b) bending in the stream direction.

The existing literature dealing with the seismic response of concrete buttress dams is mainly focused on low-frequency vibrations in the stream direction using a simplified foundation model with the massless method, which does not consider topographic amplifications [30; 68; 76; 88]. To account for the effects of topography on the dam's response, the mass of the foundation should be considered with appropriate free-field modelling. In Paper V, free-field modelling was used with the direct FE method and the analytical method, and the responses were compared with the massless method. Figures 6.16 and 6.17 show the response spectra of the acceleration time histories at the centre of the heel and the crest of the dam in the stream and cross-stream directions for the free-field modelling of the rock foundation using the direct FE method, the analytical method and the massless method, generated by the Swedish design earthquake and the Taft earthquake, respectively.

Figure 6.16 shows that the massless method leads to sliding failure because contact between the foundation and the dam is lost. In contrast, the analyses performed with a mass foundation approach, which model the foundation more realistically, result in significant radiation damping, which reduces the risk of sliding failure. Many researchers have also found that the vibrations induced in the dam are significantly overestimated with the massless approach, for example [28; 35; 140]. To overcome this problem, an unrealistically high damping ratio of about 15% was used to fit the results to the measurements [65]. It was also shown in Paper V that the risk of sliding failure decreases with increasing damping. Figure 6.16 also shows that the analytical method at the dam heel gives a similar answer to the direct FE method, while the difference between the two methods becomes greater at the dam crest. These differences are greater in the cross-stream direction due to the non-linear behaviour at the joints. For low-frequency excitation, the massless method overestimates the responses at the heel, but at the crest of the dam it overestimates the responses in the stream direction and

underestimates them in the cross-stream direction (see Figure 6.17). As can be seen from the figure, there are insignificant differences between the responses of the analytical method and the direct FE method at the heel. At the crest, however, the free-field modelling with the analytical method significantly underestimates the response in the cross-stream direction. This is due to the effect of joint opening, which the analytical method underestimates compared to the direct FE method.

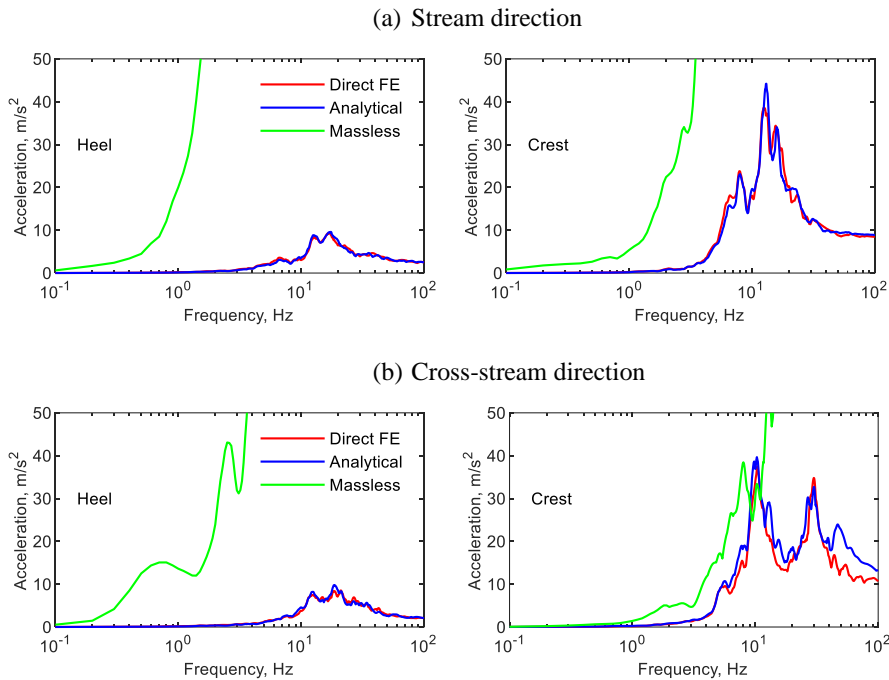


Figure 6.16: Response spectra of the acceleration time histories generated by the Swedish design earthquake at mid-heel and dam crest for free-field modelling of the rock foundation using the direct FE method, the analytical method and the massless method in the (a) stream and (b) cross-stream directions.

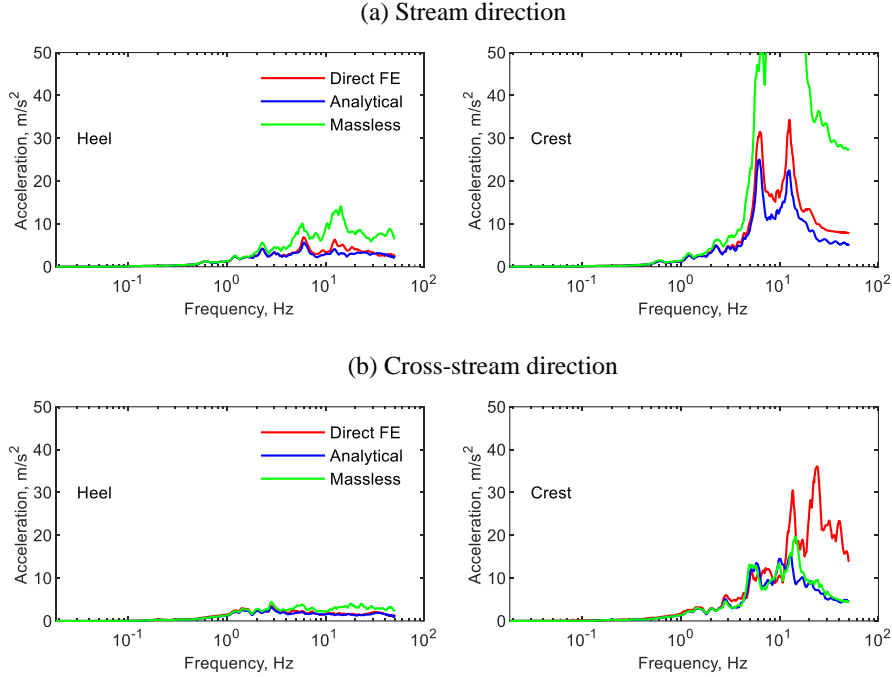


Figure 6.17: Response spectra of the acceleration time histories generated by the Taft earthquake at mid-heel and dam crest for free-field modelling of the rock foundation using the direct FE method, the analytical method and the massless method in the (a) stream and (b) cross-stream directions.

Figures 6.18a and 6.18b show the time history of the joint opening at joint 6 in the middle of the dam caused by the Swedish design earthquake and the Taft earthquake, respectively. Figures 6.19a and 6.19b show the time history of the joint opening at joint 12 near the abutment caused by the Swedish design earthquake and the Taft earthquake, while Figures 6.20a and 6.20b show the response spectra of the acceleration time histories at coordinate +44 m at the crest, generated by the Swedish design earthquake and the Taft earthquake. It can be seen from Figure 6.18 that the analytical method and direct FE method result in similar responses in the middle of the dam for the high-frequency excitation, but for the low-frequency excitation the differences between the two methods are greater, with the analytical method underestimating the joint opening. The same behaviour was observed for the joints near the abutments. Figure 6.19 shows that for the low-frequency excitation there are significant differences between the analytical method and the direct FE method. The opening and closing of the joints affects the acceleration at the crest. High-frequency accelerations in a short time are generated by triggering an impact load at the joints. In the case of low-frequency excitation, the analytical method was not able to capture the high-frequency vibrations. Therefore, the differences in the dam's response are greater for low-frequency excitation than for high-frequency excitation (see Figure 6.20). Therefore, it is important to use an accurate modelling approach for the rock foundation, especially in cases

where non-linearity is considered. The calculated response of the dam is significantly influenced by the modelling approach used for the foundation. The massless method produces an unreliable estimate of the behaviour of the dam, especially for high-frequency excitations. Free-field modelling with the analytical method resulted in unreliable joint openings, especially for the low-frequency excitation.

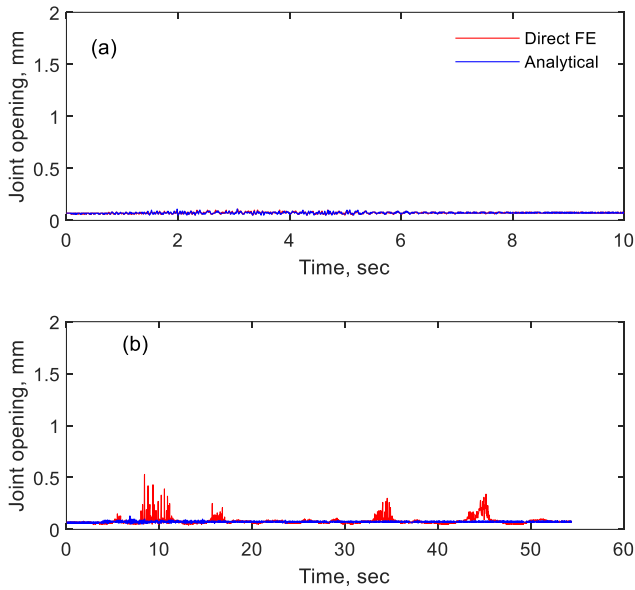


Figure 6.18: Time history of the joint opening at joint 6 (coordinate -4 m) with foundation modelling using direct FE method and analytical method, triggered by (a) the Swedish design earthquake and (b) the Taft earthquake.

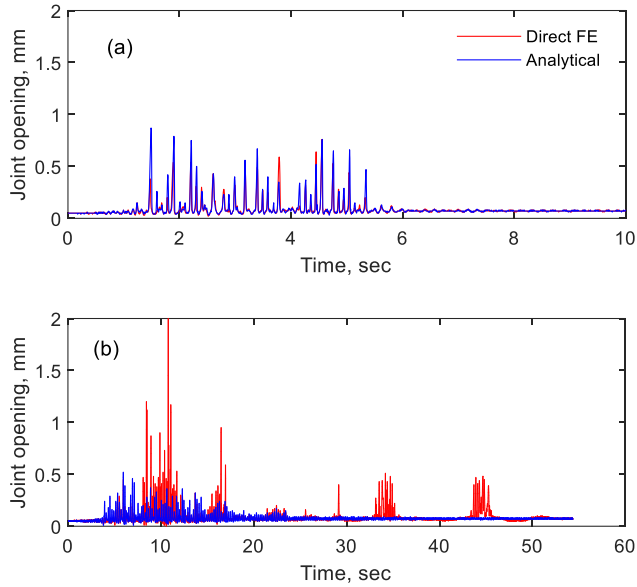


Figure 6.19: Time history of the joint opening at joint 12 (coordinate +44 m) with foundation modelling using direct FE method and analytical method, triggered by (a) the Swedish design earthquake and (b) the Taft earthquake.

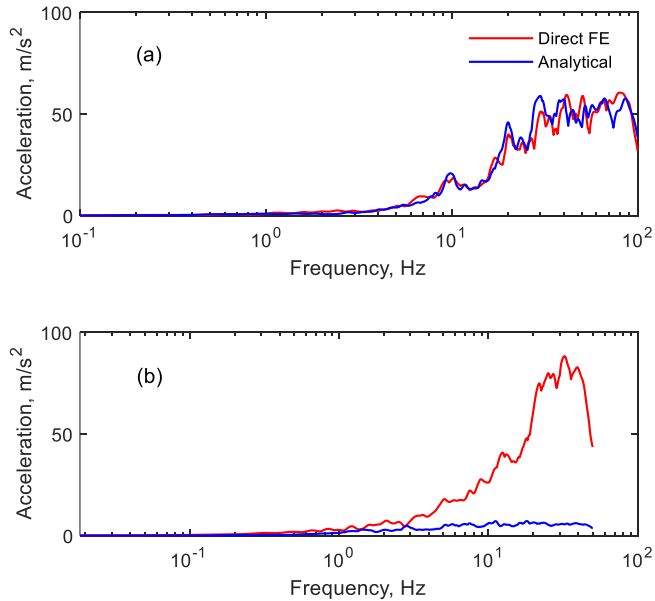
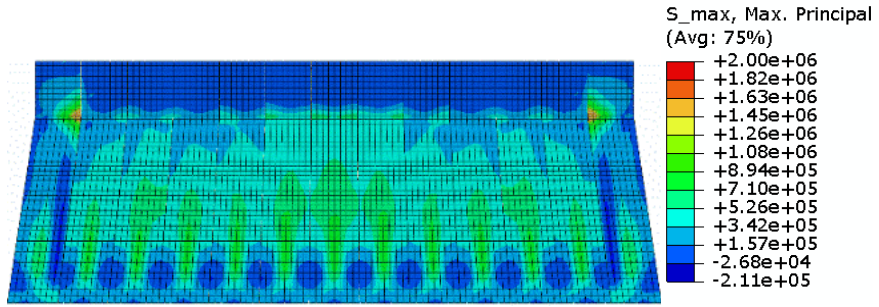


Figure 6.20: Response spectra of the acceleration time histories at the crest, the coordinate +44 m, generated by (a) the Swedish design earthquake and (b) the Taft earthquake.

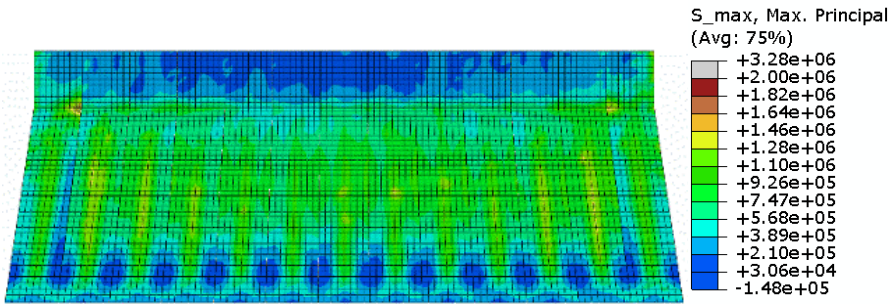
It should be noted that the high-frequency acceleration in the dam response is not only due to the opening and closing of the joints. The opening of the joints in the middle of the dam is smaller than near the abutments (see Figures 6.18-6.19). Moreover, the opening of the joints due to high-frequency excitation is smaller than that due to low-frequency excitation. Therefore, for the high-frequency excitation in Figure 6.16, the influence of the joint opening on the acceleration response spectra is very small. As can be seen, frequencies between 10-30 Hz are excited at the crest, with the higher frequencies related to the excitation of the higher bending eigenmodes. This is due to the slenderness of the structure and the higher natural frequencies excited at high-frequency excitation. With low-frequency excitation, however, a frequency interval of 5-13 Hz is excited (see Figure 6.17). As mentioned earlier, the openings of the joints are larger with low-frequency excitation than with high-frequency excitation, so that high-frequency accelerations are generated in the cross-stream direction.

The sensitivity of the buttress dam due to the cross-stream excitation was investigated by comparing the responses of a model of the dam subjected only to the vibrations in the stream direction and a model that considered all components of the earthquake. Figures 6.21a-b show the maximum envelope of the maximum principal stresses at upstream of the dam caused by the Swedish design earthquake when only the stream motion and all components of the earthquake are considered, respectively. Figures 6.22a and 6.22b show the maximum envelope of the maximum principal stresses at upstream of the dam caused by the Taft earthquake when only the stream motion and all components of the earthquake were considered.

It can be seen that the inclusion of the cross-stream oscillations leads to an increase in stresses for both excitations, with a higher increase in stress for high-frequency excitation than for low-frequency excitation (see Figures 6.21 and 6.22). As mentioned earlier, this is due to the high natural frequencies of the dam, which are more excited by the high-frequency excitation. In addition, the inclusion of cross-stream vibrations causes the joints to open, which significantly reduces safety during strong seismic excitations. The uneven topographical amplification of the high-frequency excitations at the foundation surface also resulted in uneven stress distribution between the monoliths (see Figure 6.21). However, for low-frequency excitations, the stress distribution between the monoliths is more uniform (see Figure 6.22). Therefore, for stiffness-dominated structures such as concrete buttress dams built in areas where high-frequency excitations are prevalent, it is important to consider the cross-stream vibrations, taking into account the topographic amplifications of the foundation surface using the effective foundation modelling method.

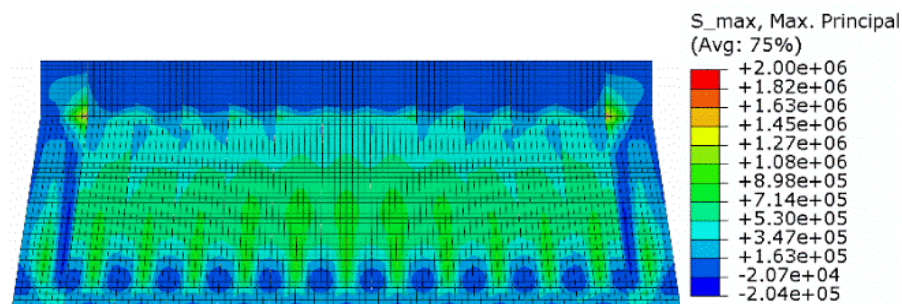


(a)

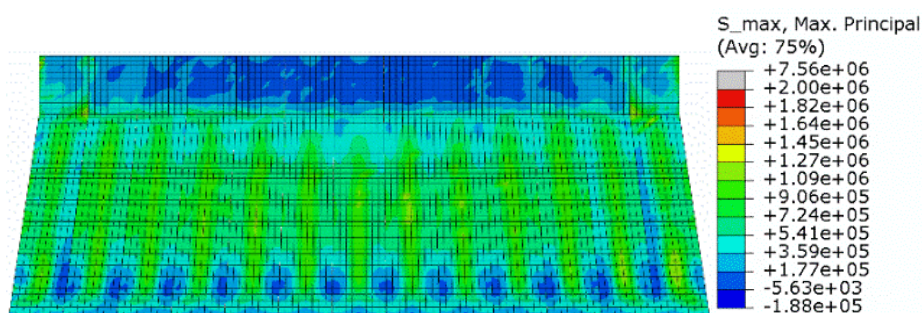


(b)

Figure 6.21: Maximum envelope of maximum principal stresses at upstream of the buttress dam triggered by the Swedish design earthquake considering (a) stream motion only and (b) all components of the earthquake.



(a)



(b)

Figure 6.22: Maximum envelope of maximum principal stresses at upstream of the buttress dam triggered by the Taft earthquake considering (a) stream motion only and (b) all components of the earthquake.

CHAPTER 7

Conclusions

The main contribution of the work of this thesis was to identify and investigate special considerations to be made when conducting analyses of concrete hydraulic structures subjected to seismic loading with relatively high dominant frequencies. In this context, two-dimensional FE models for underground structures (pipelines) were developed and the interaction between the bedrock and the surrounding soil was studied. With this method, the influence from the ground geometries can be taken into account. One of the major challenges in numerical analysis of the propagation of seismic waves in structures on the ground is modelling the free field of the foundation. Therefore, the free-field modelling methods were adapted to accurately describe the propagation of earthquake vibrations from the source to the ground surface. Two- and three-dimensional FE models were implemented and evaluated to investigate the dynamic behaviour of hydraulic structures on the ground (gravity dams and buttress dams) during the propagation of high-frequency seismic waves. In the following sections, the major conclusions related to the research questions of this thesis are summarised, and suggestions for future research are presented.

7.1 Two-dimensional FE models for underground pipelines

It was demonstrated that a two-dimensional model can effectively account for the behaviour of pipelines in the longitudinal and cross-sectional planes. The most important aspect of the models is the ability to capture bending deformations in the concrete pipelines, as these segmented structures are vulnerable in this respect. Due to the low stiffness of concrete pipelines during bending deformations, it could be concluded that the consideration of the water mass, a decreasing thickness of the soil layer and an increasing burial depth reduce the safety of a pipeline.

7.2 Influence of variations in rock geometry and soil stiffness on buried pipelines

An increase in soil stiffness and the modelling consideration of non-uniform effects lead to a greater amplification of the stresses calculated under high-frequency excitation compared to when the frequencies are lower. Varying soil depths along the pipeline reduce the safety

of the concrete pipeline, especially due to bending deformations in its barrel and joints. For a pipeline above a uniform bedrock geometry, the safety against high-frequency damage when in dense soil is about ten times the assumed tensile strength of the pipeline barrel and three times that of the pipe joints. A non-uniform bedrock reduces the safety to about three times in the pipeline barrel and 1.5 times in the joints.

7.3 Implementation of free-field modelling for dam foundations

A new time-domain deconvolution method was developed for both shear and pressure wave propagation based on an iterative procedure using a one-dimensional FE column to transform the earthquake motion from the foundation surface to the corresponding input motion at depth. It was concluded that free-field modelling of dam foundations had significant impact on computing the amplification of the high-frequency excitations due to the irregular surface topography. Free-field modelling of the foundation using the direct FE method was able to accurately capture the topographic amplifications of the seismic excitations. Free-field modelling of the foundation using an analytical method leads to errors in surface motions which exceed the acceptance criteria. Neglecting the effective earthquake forces at non-reflecting boundaries leads to a significant underestimation of the surface motion, especially for excitations with lower frequencies. The massless approach leads to extremely large errors in surface motion due to high-frequency excitations compared to those found for low-frequency excitations. A significant error was determined for excitations with a frequency of more than 20 Hz.

7.4 Implementation of 2D FE models for on the ground structures (gravity dams)

Concrete gravity dams are mass-dominated structures that have low natural frequencies and are therefore susceptible to low-frequency excitations. A two-dimensional model is able to capture the natural frequencies of such a dam. In contrast to the dynamic analysis, the massless foundation method is suitable for an eigenvalue analysis. For a linear dynamic analysis of a two-dimensional model, both the free-field modelling of the foundation with the direct FE method and the analytical method are accurate when calculating the dam response. It was found that neglecting the effective earthquake forces at non-reflecting boundaries leads to an underestimation of the dam response, while the massless method gives an overestimation.

7.5 Structural response of stiffness-dominated concrete structures (buttress dams)

Concrete buttress dams are stiffness-dominated structures that have high natural frequencies due to their slenderness. This type of structure is therefore more sensitive to high-frequency excitations. In the typical buttress dam studied in this work, high-frequency waves excited free vibration frequencies above 10 Hz, while low-frequency seismic vibrations only affected free vibration modes up to 13 Hz. The stresses in the concrete monoliths were higher during high-frequency excitations than with low frequencies. A three-dimensional model is required

for seismic evaluation of concrete buttress dams, as the cross-stream vibrations reduce the safety of the dam due to the increase in the stresses in the monoliths and the opening of the contraction joints. Topographical amplification of high-frequency waves at the surface of canyons has a significant effect on the response of this type of dam. High-frequency excitation also leads to a non-uniform stress distribution between the monoliths, which is not the case during low-frequency excitation. It was seen that the foundation modelling approach has a significant impact on the calculated response of the dam while the massless method leads to unreliable results, especially for high-frequency excitations. It could also be concluded that free-field modelling using the analytical method leads to unreliable joint openings.

7.6 Future research

Based on the results obtained for the soil-pipeline system, and considering the significant effect of non-uniform ground due to inclined bedrock, future studies including more examples with non-uniform ground, such as cases with rock outcrop, are motivated. The analyses performed with the simplified method ignore effective forces at non-reflected side boundaries. This will result in energy leakage and attenuation of incoming seismic waves, and when this effect is considered, the evaluated safety will decrease. Therefore, for future research it is highly recommended to consider effective earthquake forces at non-reflecting boundaries. Furthermore, by defining nonlinear soil behaviour and introducing varying soil material properties with ground depth, it can be expected that the accuracy of the FE models will be significantly improved. For verification of numerical results, it is difficult to obtain in-situ pipe stresses from seismic events, and therefore scale model tests should be considered.

Effective earthquake forces were calculated based on vertical propagation of seismic waves. The influence of the incidence angle should be investigated. This is more important for soft soils as the angle of incidence is not vertical for soft soil layers near the surface. For the dam-water-foundation systems, the foundation was in this case modelled for one rock stiffness. For future work, it is recommended to consider different rock stiffnesses and to study this effect with respect to the following rock foundation modelling methods: massless method and massed foundation using effective earthquake forces. For the buttress dam considered here, the effect from spillways was not included. Spillways are slender structures and a study of their response during high-frequency excitation is recommended. An investigation of the effect of slenderness of the buttress dam also is of interest for high-frequency excitations. The type of buttress dam considered here has a partly inclined front plate. The other type of buttress dam has an all inclined front plate, the Ambursen buttress dam type, which should also be considered in future studies. The effect from struts that are built between buttresses for lateral supports is also recommended as a future research topic.

REFERENCES

- [1] ABAQUS, ver.6.14 Documentation. Dassault Systèmes Simulia Corporation Providence, Rhode Island, USA, 2014.
- [2] Abbasiverki, R., Ahmed, L., Nordström, E., Analysis of load and response on large hydropower draft tube structures. Energiforsk, Stockholm, Sweden, 2019.
- [3] Abbasiverki, R., Analysis of underground concrete pipelines subjected to seismic high-frequency loads. Licentiate thesis, KTH Royal Institute of Technology, Stockholm, Sweden, 2016.
- [4] Abbasiverki, R., Nordström, E., Ansell, A., Initial study on seismic analyses of concrete and embankment dams in Sweden. Report 164, KTH Royal Institute of Technology, Stockholm, Sweden, 2017.
- [5] Ahmadi, M., Khoshrang, G., Mokhtarzadeh, A., Jalalzadeh, A., Behavior of a large concrete dam to an actual maximum credible earthquake. Proceeding of the 10th world conference on earthquake engineering, vol 7, Madrid, Spain, 1992.
- [6] Ahmed, L., Models for analysis of young cast and sprayed concrete subjected to impact-type loads. PhD thesis, KTH Royal Institute of Technology, Stockholm, Sweden, 2015.
- [7] Alembagheri, M., Ghaemian, M., Seismic performance evaluation of a jointed arch dam. Structure and Infrastructure Engineering, 12 (2), 256-274, 2016. DOI: 10.1080/15732479.2015.1009124
- [8] Alterman, Z., Karal, F.C., Propagation of elastic waves in layered media by finite difference methods. Bulletin of the Seismological Society of America, 58(1), 367-398, 1968. DOI: 10.1785/BSSA0580010367
- [9] American Lifelines Alliance (ALA), Buried steel pipes. American Society of Civil Engineers (ASCE) and Federal Emergency Management Agency (FEMA), Washington DC, USA, 2001.
- [10] Ando, H., Sato, S., Takagi, N., Seismic observation of a pipeline buried at the heterogeneous ground. Proceedings of the Tenth World Conference on Earthquake Engineering, Madrid, Spain, 1992.

- [11] Ansell, A., Dynamically loaded rock reinforcement. PhD thesis, KTH Royal Institute of Technology, Stockholm, Sweden, 1999.
- [12] Ansell, A., Malm, R., Modelling of thermally induced cracking of a buttress dam. *Nordic Concrete Research*, 38(2), 69-88, 2008a.
- [13] Ansell, A., Malmgren, L., The response of shotcrete to blast induced vibrations in mining. 10th Congress of the ISRM, Technology roadmap for rock mechanics, Sandton City, South Africa, 2003.
- [14] Archuleta, R.J., Frazier, G.A., Three-dimensional numerical simulations of dynamic faulting in a half-space. *Bulletin of the Seismological Society of America*, 68(3), 541-572, 1978. DOI: 10.1785/BSSA0680030541
- [15] Asghari, E., Taghipour, R., Bozorgnasab, M., Seismic analysis of concrete gravity dams considering foundation mass effect. *KSCE Journal of Civil Engineering*, 22, 4988-4996, 2018. DOI: 10.1007/s12205-017-0278-6
- [16] Basu, U., Chopra, A.K., Perfectly matched layers for transient elastodynamics of unbounded domains. *International Journal for Numerical Methods in Engineering*, 59(8), 1039-1074, 2004. DOI: 10.1002/nme.896.
- [17] Basu, U., Perfectly matched layers for acoustic and elastic waves: Theory, finite-element implementation and application to earthquake analysis of dam-water-foundation rock systems. PhD thesis, University of California, Berkeley, USA, 2004.
- [18] Berenger, J.P., A perfectly matched layer for the absorption of electromagnetic waves. *Journal of Computational Physics*, 114(2), 185-200, 1994. DOI: 10.1006/jcph.1994.1159.
- [19] Bielak, J., Loukakis, K., Hisada, Y., Yoshimura, C., Domain reduction method for three-dimensional earthquake modelling in localized regions, part I: theory. *Bulletin of the Seismological Society of America*, 93(2), 817-824, 2003. DOI:10.1785/0120010251
- [20] Bougacha, S., Tassoulas, J.L., Seismic analysis of gravity dams. I: Modeling of sediments. *Journal of Engineering Mechanics*, 117(8), 1826-1837, 1991. DOI: 10.1061/(ASCE)0733-9399(1991)117:8(1826).

- [21] Bryne, L.E., Time dependent material properties of shotcrete for hard rock tunnelling. PhD thesis, KTH Royal Institute of Technology, Stockholm, Sweden, 2014.
- [22] BS 4449, Steel for the reinforcement of concrete. British Standard Publications, London, UK, 2005.
- [23] BS EN 641, Reinforced concrete pressure pipes, cylinder type, including joints and fittings. British Standards Institution, European Standard, London, UK, 1995.
- [24] BS EN 642, Prestressed concrete pressure pipes, cylinder and non-cylinder, including joints, fittings and specific requirement for prestressing steel for pipes. British Standards Institution, European Standard, London, UK, 1995.
- [25] Chavez, J.W., Fenves G.L., EAGD_SLIDE: A computer program for the earthquake analysis of concrete gravity dams including base sliding. Report No. UCB/SEMM-1994/02, Department of Civil Engineering, University of California, Berkeley, USA, 1994.
- [26] Chavez, J.W., Fenves G.L., Earthquake analysis and response of concrete gravity dams including base sliding. Report No. UCB/EERC-93/07, Earthquake Engineering Research Centre, University of California, Berkeley, USA. 1993.
- [27] Chen, D., Hou, C., Wang, F., Influences on the seismic response of the gravity dam-foundation-reservoir system with different boundary and input models. Shock and Vibration, Vol 2021, 1-15, 2021. DOI:10.1155/2021/6660145
- [28] Chen, D.H., Du, C.B., Yuan, J.W., Hong, Y.W., An investigation into the influence of damping on the earthquake response analysis of a high arch dam. Journal of Earthquake Engineering, 16 (3), 329-349, 2012. DOI: 10.1080/13632469.2011.638697
- [29] Chen, Y., Simplified and refined earthquake analyses for buried pipes. Mathematical and Computer Modelling, 21(11), 47-60, 1995. DOI: 10.1016/0895-7177(95)00078-G

- [30] Chi-fai, W., Jason, H., Andrew, R., John, S., Oberon dam-failure hazard of a buttress dam and its vulnerability to earthquake damage. ANCOLD (Australian National Committee on Large Dams), Conference, Perth, Australia, 2012.
- [31] Chopra, A.K., Chakrabarti, P., Gupta, S., Earthquake response of concrete gravity dams including hydrodynamic and foundation interaction effects. Report No. UCB/EERC-80/01, 1980.
- [32] Chopra, A.K., Dynamics of structures, Theory and applications to earthquake engineering. Prentice-Hall, Berkley, USA, 2001.
- [33] Chopra, A.K., Earthquake analysis of concrete dams: Factors to be considered. Tenth U.S. National Conference on Earthquake Engineering, Anchorage, USA, 2014.
- [34] Chopra, A.K., Hydrodynamic pressures on dams during earthquakes. Journal of the Engineering Mechanics Division, 93(6), 205-224, 1967.
- [35] Chuhan, Z., Jianwen, P., Jinting, W., Influence of seismic input mechanisms and radiation damping on arch dam response. Soil Dynamics and Earthquake Engineering, 29 (9), 1282-1293, 2009. DOI: 10.1016/j.soildyn.2009.03.003
- [36] Chung, D.H., Bernreuter, D.L., The effect of regional variation of seismic wave attenuation on the strong ground motion from earthquakes. Lawrence Livermore Laboratory, Washington DC, USA, 1981.
- [37] Clough, R.W., Non-linear mechanisms in the seismic response of arch dams. Proceedings of the international research conference earthquake engineering, Skopje, Yugoslavia, 1980.
- [38] Cohen, M., Jennings, P.C., Silent boundary methods for transient analysis. Computational Methods for Transient Analysis, 1, 301-357, 1983.
- [39] COMET, http://kejian1.cmatc.cn/vod/comet/hydro/damfailure/applications_int/print.php.htm#page_3-0-0, Boulder University Corporation for Atmospheric Research, Boulder, USA, 2021.
- [40] Connor, J., Faraji, S., Fundamentals of structural engineering. Springer, ISBN 978-1-4614-3262-3 (eBook), 2013, DOI 10.1007/978-1-4614-3262-3

- [41] Curtis, D.D., Sooch, G., Brewer, T., Schildmeyer, A., Explicit seismic analysis of Mossyrock dam. Proceedings for the 33rd Annual USSD Conference. Phoenix AZ, USA, 2013.
- [42] Cvijanovic, V., Schultz, M., Armstrong, R., Application of nonlinear analysis methods to hydraulic structures subject to extreme loading conditions. Proceedings for 34th Annual USSD Conference, San Francisco, USA, 2014.
- [43] Datta, T.K., Mashaly, E.A., Pipeline response to random ground motion by discrete model. International journal of Earthquake Engineering and Structural Dynamics, 14, 559-572, 1986. DOI: 10.1002/eqe.4290140406
- [44] Datta, T.K., Mashaly, E.A., Seismic response of buried submarine pipelines. Transactions of the ASME, Journal of Energy Resources Technology, 208-218, 1988.
- [45] Datta, T.K., Seismology, seismic analysis of structures. John Wiley & Sons, New Delhi, India, 2010. DOI:10.1002/9780470824634
- [46] Datta, S.K., O'Leary, P.M, Shah, A.H., Three-dimensional dynamic response of buried pipelines to incident longitudinal and shear waves. Journal of Applied Mechanics, 52(919), 915-926, 1985. DOI: 10.1115/1.3169169
- [47] Davis, C., Bardet, J., Seismic analysis of large-diameter flexible underground pipes. Journal of Geotechnical and Geoenvironmental Engineering, 124(10), 1005-1015, 1998.
- [48] Deeks, A.J., Randolph, F.M., Axisymmetric time-domain transmitting boundaries. Journal of Engineering Mechanics, 120(1), 25-42, 1994.
- [49] Domínguez, J., Gallego, R., Japón, B.R., Effects of porous sediments on seismic response of concrete gravity dams. Journal of Engineering Mechanics, 123(4), 302-311, 1997. DOI: 10.1061/(ASCE)0733-9399(1997)123:4(302)
- [50] Dowrick, D., The nature of earthquakes, earthquake resistant design and risk reduction. John Wiley & Sons, Tauranga, New Zealand, 2009.

- [51] DSO-19-13: Evaluation of numerical models and input parameters in the analysis of concrete dams, USSD Workshop, Miami, USA, 2018. <https://www.usbr.gov/ssle/damsafety/TechDev/DSOTechDev/DSO-2019-13.pdf>
- [52] Du, X., Tu, J., Nonlinear seismic response analysis of arch dam-foundation systems-part II opening and closing contact joints. *Bulletin of Earthquake Engineering*, 5 (1), 121-133, 2007.
- [53] Du, X., Zhang, Y., Zhang, B., Nonlinear seismic response analysis of arch dam-foundation systems, part I: Dam-foundation rock interaction. *Bulletin of Earthquake Engineering*, 5 (1), 105-119, 2007.
- [54] Eidinger, J.M., Avila, E.A., Guidelines for the seismic evaluation and upgrade of water transmission facilities. American Society of Civil Engineers, Reston, USA, 1999.
- [55] Eriksson, D., Multiphase models for freeze-thaw actions and mass transport in concrete hydraulic structures. PhD thesis, KTH Royal Institute of Technology, Stockholm, Sweden, 2021.
- [56] Eurocode 2, Design of concrete structures. European Committee for Standardisation (CEN), EN 1992-1-1, Brussels, Belgium, 2004.
- [57] Eurocode 8, Design of structures for earthquake resistance, Part 5: Foundations, retaining structures and geotechnical aspects. European Committee for Standardisation (CEN), EN 1998-5, Brussels, Belgium, 2004.
- [58] Eurocode 8, Design of structures for earthquake resistance, Part 4: Soils, tanks and pipelines. European Committee for Standardisation (CEN), EN 1998-4, Brussels, Belgium, 2006.
- [59] Faccioli, E., Maggio, F., Paolucci, R., Quarteroni, A., 2D and 3D elastic wave propagation by a pseudo-spectral domain decomposition method. *Journal of Seismology*, 1(3), 237-251, 1997.
- [60] FEMA: HAZUS-MH MR4, Multi-hazard loss estimation methodology, earthquake model. Technical Manual, National Institute of Building Science, Washington DC, USA, 2003.
- [61] Fenves G., Chopra A.K., EADG-84: A computer program for earthquake analysis of concrete gravity dams. Report No. UCB/EERC-84/11, University of California, Berkeley, USA, 1984.

- [62] Fenves G., Chopra A.K., Simplified analysis for earthquake Resistance design of concrete gravity dams. Report No. UCB/EERC-85/10, University of California, Berkeley, USA, 1986.
- [63] Fenves, G., Chopra, A.K., Earthquake analysis of concrete gravity dams including reservoir bottom absorption and dam-water-foundation rock interaction. *Earthquake Engineering and Structural Dynamics*, 12(5), 663-680, 1984. DOI: 10.1002/eqe.4290120507.
- [64] Frankel, A., Three-dimensional simulations of ground motions in the San Bernardino Valley, California, for hypothetical earthquakes on the San Andreas fault. *Bulletin of the Seismological Society of America*, 83(4), 1020-1041, 1993.
- [65] Fry, J.J., Matsumoto, N., Validation of dynamic analyses of dams and their equipment. *International Symposium on the Qualification of Dynamic Analyses of Dams and their Equipments*, Saint-Malo, France, 2016.
- [66] Fukuyama, E., Madariaga, R., Dynamic rupture front interaction on 3D planar fault. *National Institute for Earth Sciences and Disaster Prevention*, Tsukuta, Japan, 1999.
- [67] Galvez, P., Ampuero, J.P., Dalguer, L.A., Somala, S.N., Nissen-Meyer, T., Dynamic earthquake rupture modelled with an unstructured 3-D spectral element method applied to the 2011 M9 Tohoku earthquake. *Geophysical Journal International*, 198(2), 1222-1240, 2014. DOI: 10.1093/gji/ggu203
- [68] Ghaemmaghami, A., Ghaemian, M., Experimental seismic investigation of sefid-rud concrete buttress dam model on shaking table. *Earthquake Engineering and Structural Dynamics* 37, 809-23, 2008. DOI: 10.1002/eqe.791
- [69] Ghanaat, Y., Failure modes approach to safety evaluation of dams. *Proceedings of the 13th world conference on earthquake engineering*, Vancouver, Canada, 2004.
- [70] Goldgruber, M., Nonlinear seismic modelling of concrete dams. *Technical University, Graz*, 2015. DOI: 10.13140/RG.2.1.3001.6485.

- [71] Gorai, S., Maity, D., Seismic performance evaluation of concrete gravity dams in finite-element framework. *Practice Periodical on Structural Design and Construction*, 27(1), 1-18, 2022.
- [72] Graves, R.W., Simulating seismic wave propagation in 3D elastic media using Staggered-grid finite differences. *Bulletin of the Seismological Society of America*, 86(4), 1091-1106, 1996.
- [73] Graves, R.W., Three-dimensional finite difference modelling of the San Andreas fault: Source parameterization and ground-motion levels. *Bulletin of the Seismological Society of America*, 88(4), 881-897, 1998.
- [74] Hall, J.F., Chopra, A.K., Dynamic analysis of arch dams including hydrodynamic effects. *Journal of Engineering Mechanics*, ASCE, 109(1), 149-163, 1983.
- [75] Hall, L., Simulations and analyses of train-induced ground vibrations; a comparative study of two- and three-dimensional calculations with actual measurements. PhD thesis, KTH Royal Institute of Technology, Stockholm, Sweden, 2000.
- [76] Hariri-Ardebili, M., Seyed-Kolbadi, S., Seismic cracking and instability of concrete dams: smeared crack approach. *Engineering Failure Analysis*, 52, 45-60, 2015. DOI: 10.1016/j.engfailanal.2015.02.020
- [77] Hariri-Ardebili, M.A., Concrete dams: from failure modes to seismic fragility. *Encyclopedia of Earthquake Engineering*, Springer-Verlag Berlin Heidelberg, Germany, 2016.
- [78] Hariri-Ardebili, M.A., Seyed-Kolbadi, S.M. and Kianoush, M.R., FEM-based parametric analysis of a typical gravity dam considering input excitation mechanism. *Soil Dynamics and Earthquake Engineering*, 84, 22-43, 2016. DOI:10.1016/j.soildyn.2016.01.013.
- [79] Harrison, S., Nöjd, S., Influence of foundation modelling on the seismic response of a concrete dam. Master thesis, KTH Royal Institute of Technology, Stockholm, Sweden, 2021.
- [80] Hashash, Y.M. A., Hook, J.J., Schmidt, B., Yao, J.I.C., Seismic design and analysis of underground structures. *Tunnelling and Underground Space Technology*, 16(4), 247-293, 2001. DOI: 10.1016/S0886-7798(01)00051-7

- [81] Hashash, Y.M.A., Groholski, D.R., Phillips, C.A., Park, D., Musgrove, M., DEEPSOIL user manual and tutorial, Version 5.0. University of Illinois, Urbana, IL, USA, 2011.
- [82] Hindy, A., Novak, M., Earthquake response of underground pipelines. *International journal of Earthquake Engineering and Structural Dynamics*, 7, 451-476, 1979.
- [83] Hindy, A., Novak, M., Pipeline response to random ground motion. *Journal of the Engineering Mechanics Division*, 106, 339-360, 1980.
- [84] Hosseini, M., Jalili, S., Azizpour, O., Alikhani, M., Evaluating the functionality of water distribution networks in the aftermath of big earthquakes based on nonlinear modelling of pipes connections. *ASCE Pipeline Conference*, Kingston. Colorado, USA, 2010.
- [85] Hosseini, M., Roudsari, M.T., A study on the effect of surface transverse waves on buried steel pipelines considering the nonlinear behaviour of soil and pipes. *ASCE Pipeline Conference*, Kingston, Colorado, USA, 2010.
- [86] Houqun, C., Seismic safety analysis of tall concrete dams, investigation and insights on critical challenges. *Earthquake Engineering and Engineering Vibration*, 19, 533-539, 2020. DOI: 10.1007/s11803-020-0578-6
- [87] Ichimura, T., Fujita, K., Yoshiyuki, A., Quinay P.E., Hori, M., Sakanoue, T., Performance enhancement of three-dimensional soil structure model via optimization for estimating seismic behavior of buried pipelines. *Journal of Earthquake and Tsunami*, 11(5), 2017. DOI: 10.1142/S1793431117500191
- [88] Ilinca, C., Vârvorea, R., Popovici, A., Influence of dynamic analysis methods on seismic response of a buttress dam. *Mathematical Modelling in Civil Engineering*, 10(3), 12-26, 2014. DOI:10.2478/mmce-2014-0012
- [89] Jianwen, P., Yanjie, X., Feng, J. Jinting, W., Seismic stability assessment of an arch dam-foundation system. *Earthquake Engineering and Engineering Vibration*, 14, 517-526, 2015. DOI: 10.1007/s11803-015-0041-2

- [90] Kouretzis, G.P., Bouckovalas, G.D., Gantes, C.J., 3-D shell analysis of cylindrical underground structures under seismic shear (S) wave action. *Soil Dynamic and Earthquake Engineering*, 26, 909-921, 2006.
- [91] Kouretzis, G.P., Bouckovalas, G.D., Karamitros, D.K., Seismic verification of long cylindrical underground structures considering Rayleigh wave effects. *Tunnelling and Underground Space Technology*, 26 (6), 789-794, 2011.
- [92] Kozlov, D., Some provisions of calculations of hydraulic structures according to Russian norms and American standards. *MATEC Web of Conferences* 251, 02004, 2018. DOI:10.1051/mateconf/201825102004.
- [93] Kramer, S.L., *Geotechnical earthquake engineering*. Prentice Hall, Upper Saddle River NJ, USA, 1996. DOI: 10.1007/978-3-540-35783-4.
- [94] Kuhlemeyer, R.L. and Lysmer, J., Finite element method accuracy for wave propagation problems. *Journal of the Soil Mechanics and Foundations Division*, 99(5), 421-427, 1973.
- [95] Lanzano, G., Salzano, E., Santucci De Magistris, F., Fabbrocino, G., An observational analysis of seismic vulnerability of industrial pipelines. *Chemical Engineering Transaction*, 26, 567-572, 2012.
- [96] Lee, D.H., Kim, B.H., Lee, H., Kong, J.S., Seismic behaviour of a buried gas pipeline under earthquake excitations. *Journal of Engineering Structures*, 31, 1011–1023, 2009. DOI: 10.1016/j.engstruct.2008.12.012
- [97] Léger, P., Katsouli, M., Seismic stability of concrete gravity dams. *Earthquake Engineering and Structural Dynamics*, 18(6), 889-902, 1989. DOI: 10.1002/eqe.4290180611.
- [98] Liang, J.W., Sun, S.P., Site effects on seismic behaviour of pipelines: a review. *Journal of Pressure Vessel Technology*, 122 (4), 469-475, 2000.
- [99] Liu, J.B., Wang, Z.Y., Du, X.L. and Du, Y.X., Three-dimensional visco-elastic artificial boundaries in time domain for wave motion problems. *Journal of Engineering Mechanics*, 22(6), 46-51, 2005.
- [100] LS-DYNA Keyword User's Manual, Livermore Software Technology Corporation (LSTC). California, USA, 2017.

- [101] Løkke, A., Chopra, A.K., Direct finite element method for nonlinear earthquake analysis of 3-dimensional semi-unbounded dam-water-foundation rock systems. *Earthquake Engineering and Structural Dynamics*, 47(5), 1309-1328, 2018. DOI:10.1002/eqe.3019.
- [102] Løkke, A., Chopra, A.K., Direct finite element method for nonlinear earthquake analysis of concrete dams: Simplification, modelling, and practical application. *Earthquake Engineering Structural Dynamic*, 48, 818-842, 2019. DOI:10.1002/eqe.3150
- [103] Løkke, A., Chopra, A.K., Direct-finite-element method for nonlinear earthquake analysis of concrete dams including dam–water–foundation rock interaction. Report No. 2019/02, Pacific Earthquake Engineering Research Center, University of California, Berkeley, USA, 2019.
- [104] Lotfi, V., Roesset, J.M., Tassoulas, J.L., A technique for the analysis of the response of dams to earthquakes. *Earthquake Engineering and Structural Dynamics*, 15(4), 463-489, 1987. DOI: 10.1002/eqe.4290150405.
- [105] Lysmer, J., Drake, L.A., A finite element method for seismology. *Methods in Computational Physics: Advances in Research and Applications*, Elsevier, 11, 181-216, 1972. DOI:10.1016/B978-0-12-460811-5.50009-X
- [106] Lysmer, J., Kulemeyer, R.L., Finite dynamic model for infinite media. *Journal of Engineering Mechanics*, ASCE, 95, 759-877, 1969.
- [107] Malm, R., Guidelines for structural FE analyses of concrete dams. Elforsk, Stockholm, Sweden, 2016.
- [108] Maltidis, G., Stempniewski, L., Fluid structure interaction arch dam-reservoir at seismic loading. 12th International Benchmark Workshop on Numerical Analysis of Dams, Graz, Austria, 2013.
- [109] Mandal, A., Maity, D., Fluid structure interaction analysis under earthquake loading and its application to concrete gravity dam. Recent Advances in Computational and Experimental Mechanics, Vol II. Lecture Notes in Mechanical Engineering, Springer, Singapore, 2022. DOI: 10.1007/978-981-16-6490-8_9
- [110] MATLAB, version R2018a. The MathWorks Inc., Natick MA, USA, 2018.

- [111] Medina, F., Dominguez, J., Tassoulas, J.L., Response of dams to earthquakes including effects of sediments. *Journal of Structural Engineering*, 116(11), 3108–3121, 1990. DOI: 10.1061/(ASCE)0733-9445(1990)116:11(3108).
- [112] Mejia, L.H., Dawson, E.M., Earthquake deconvolution for FLAC. *Proceedings. Fourth International FLAC Symposium on Numerical Modeling in Geomechanics*, Madrid, Spain, 2006.
- [113] Messaad, M., Bourezane, M., Latrache, M., Berrabah, A.T., Ouzendja, D., Three-dimensional seismic analysis of concrete gravity dams considering foundation flexibility. *Mechanics and Mechanical Engineering*, 25 (1), 88-98, 2021. DOI: 10.2478/mme-2021-0012
- [114] Meyer, P., The impact of high frequency/low energy seismic waves on unreinforced masonry. *Massachusetts Institute of Technology*, Cambridge MA, USA, 2006.
- [115] Mohammadnezhad, H., Ghaemian, M., Noorzad, A., Seismic analysis of dam-foundation-reservoir system including the effects of foundation mass and radiation damping. *Earthquake Engineering and Engineering Vibration*, 18, 203-218, 2019. DOI: 10.1007/s11803-019-0499-4.
- [116] Moser, A.P., Buried pipe design. *The McGraw-Hill Companies*, Logan, Utah, USA, 2001.
- [117] Muleski, G.E., Ariman, T., Aumen, C.P., A shell model for buried pipes in earthquakes. *Journal of soil dynamics and earthquake engineering*, 4, 43-51, 1985.
- [118] Nam-Ho, K., Introduction to nonlinear finite element analysis, ISBN 978-1-4419-1746-1, Springer, New York NY, USA, 2015. DOI: 10.1007/978-1-4419-1746-1.
- [119] Nielsen, A.H., Absorbing boundary conditions for seismic analysis in ABAQUS. *Proceedings of the 2006 ABAQUS Users' Conference*, Boston, MA, USA, 359-376, 2006.
- [120] Novak, M., Hindy, A., Seismic analysis of underground tubular structures. *Proceeding of the Seventh World Conference Earthquake Engineering*, 8, Istanbul, Turkey, 1980.

- [121] Nowak, P.S., Hall, J.F., Arch dam response to nonuniform seismic input. *Journal of Engineering Mechanics*, 116(1), 125-139, 1990. DOI: 10.1061/(ASCE)0733-9399(1990)116:1(125)
- [122] O'Rourke, M.J., Liu X., Response of buried pipelines subjected to earthquake effects. MCEER, University of New York, Buffalo, USA, 1999.
- [123] O'Rourke, M.J., Liu, X., Seismic design of buried and offshore pipelines. MCEER, University of New York, Buffalo, USA, 2012.
- [124] Ohtsuki, A., Harumi, K., Effect of topography and subsurface inhomogeneities on seismic SV waves. *Earthquake Engineering and Structural Dynamics*, 11(4), 441-462, 1983.
- [125] Olsen, K.B., Archuleta, R.J., Matarrese, J.R., Three-dimensional simulation of a magnitude 7.75 earthquake on the San Andreas fault. *Science*, 270(5242), 1628-1632, 1995.
- [126] Pan, J., Xu, Y., Jin, F., Wang, J., Seismic stability assessment of an arch dam-foundation system. *Earthquake Engineering and Engineering Vibration*, 14, 517–526, 2015. DOI: 10.1007/s11803-015-0041-2
- [127] PEER, Pacific Earthquake Engineering Research Center, University of California, Berkeley, 2020, <http://peer.berkeley.edu/>
- [128] Poul, M.K., Zerva, A., Efficient time-domain deconvolution of seismic ground motions using the equivalent-linear method for soil-structure interaction analyses. *Soil Dynamics and Earthquake Engineering*, 112, 138-151, 2018. DOI:10.1016/j.soildyn.2018.04.032.
- [129] Poursartip, B., Topographic amplification of seismic motion, PhD thesis, University of Texas, Austin, Texas, USA, 2017.
- [130] Python Language Reference, version 2.7. Python Software Foundation, Amsterdam, Netherlands, 2010.
- [131] Rea, D., Liaw C.Y., Chopra, A.K., Dynamic properties of Pine Flat dam. Report No. UCB/EERC-72/7, University of California, Berkeley, USA, 1972.
- [132] RIDAS, Swedish hydropower companies guidelines for dam safety, application guideline Concrete dams (In Swedish), Swedenergy AB, Stockholm, Sweden, 2011.

- [133] Roudsari, M.T., Hosseini, M., Using neural network for reliability assessment of buried steel pipeline networks subjected to earthquake wave propagation. *Journal of Applied Sciences*, 11(18), 3233-3246, 2011. DOI: 10.3923/jas.2011.3233.3246
- [134] Rydell, C., Seismic high-frequency content loads on structures and components within nuclear facilities. Licentiate thesis, KTH Royal Institute of Technology, Stockholm, Sweden, 2014.
- [135] S:T Eriks, Underground infrastructures. Handbook for water and waste water networks (in Swedish). S:T Eriks, Stockholm, Sweden, 2013.
- [136] Saberi, M., Behnamfar, F., Vafaeian, M., A semi-analytical model for estimating seismic behavior of buried steel pipes at bend point under propagating waves. *Bulletin of Earthquake Engineering Journal*, 11, 1373-1402, 2013. DOI: 10.1007/s10518-013-9430-y
- [137] Sadat Shokouhi, S.K., Dolatshah, A., Vosoughifar, H.R., Hosseinienejad, S.Z., Rahnavard, Y., Optimal sensor placement of TYTON joints in the water pipeline networks Subjected to near-fault and far-fault earthquakes. *Proceedings of the Pipelines Conference*, Fort Worth, Texas, USA, 2013.
- [138] Sadat Shokouhi, S.K., Mokhlespour, M.E. Optimal sensor placement for bolted-gland joints in the water pipeline networks subjected to near-fault and far-fault earthquakes. *International Conference on Pipelines and Trenchless Technology*, Xi'an, China, 2013.
- [139] Salamon, J., Hariri-Ardebili, M.A., Malm, R., Wood, C., Faggiani G, Theme a–formulation: seismic analysis of Pine Flat Concrete Dam. 15th international benchmark workshop on numerical analysis of dams, Milan, Italy, 2019.
- [140] Salamon, J.W., Wood, C., Hariri-Ardebili, M.A., Malm, R., Faggiani, G., Seismic Analysis of Pine Flat Concrete Dam: Formulation and Synthesis of Results, Numerical Analysis. *Proceedings of the 15th ICOLD International Benchmark Workshop*, Milan, Italy, Springer, 2021. DOI:10.1007/978-3-030-51085-5_1
- [141] Sanchez-Sesma, F.J., Campillo, M., Diffraction of P, SV, and Rayleigh waves by topographic features: A boundary integral formulation. *Bulletin of the Seismological Society of America*, 81(6), 2234-2253, 1991. DOI: 10.1785/BSSA0810062234

- [142] Sarkhel, S., Padhi, J., Dash, A.K., Seismic analysis of a concrete gravity dam using ABAQUS. Recent Developments in Sustainable Infrastructure, Lecture Notes in Civil Engineering, Springer, Singapore, 75, 2021. DOI:10.1007/978-981-15-4577-1_21
- [143] Schnabel, P.B., Lysmer, J. and Seed, H.B., SHAKE: A computer program for earthquake response analysis of horizontally layered sites. Report No. UCB/EERC-72/12, Earthquake Engineering Research Centre, University of California, Berkeley, USA, 1972.
- [144] Shen, C., Chen, H., Chang, C., Huang, L., Zi, T., Yang, C., Wang, T., Lo, H., Earthquake induced by reservoir impounding and their effect on Hsinfengkiang dam. Scientia Sinica, 17(2), 239-272, 1974.
- [145] Shi, P., Seismic wave propagation effects on buried segmented pipelines. Soil Dynamics and Earthquake Engineering, 72(1), 89-98, 2015. DOI: 10.1016/j.soildyn.2015.02.006
- [146] SKI, Seismic safety-Characterization of seismic ground motions for probabilistic safety analyses of nuclear facilities in Sweden. SKI, Swedish Nuclear Power Inspectorate, Stockholm, Sweden, 1992.
- [147] Song, Z., Wang, F., Liu, Y., Su, C., Infinite element static-dynamic unified artificial boundary. Shock and Vibration, Vol 2018, Article ID 7828267, 1-14, 2018. DOI: 10.1155/2018/7828267
- [148] Sooch, G.S., Bagchi, A., A new iterative procedure for deconvolution of seismic ground motion in dam-reservoir-foundation systems. Journal of Applied Mathematics, Vol 2014, 1-10, 2014. DOI:10.1155/2014/287605
- [149] Svinkin, M.R., Prediction and calculation of construction vibrations. 24th Annual Member's Conference of the Deep Foundations Institute in Dearnorn, Michigan, USA, 1999.
- [150] Tadda, M.A., Ahsan, A., Imteaz, M., Shitu, A., Danhassan, U.A., Muhammad, A.I., Hydraulic Structures-Theory and Applications: Operation and maintenance of hydraulic structures. IntechOpen, London, UK, 2020.
- [151] Takada, S., Hassani, N., Fukuda, K., Damage directivity in buried pipelines of Kobe City during the 1995 earthquake. Journal of Earthquake Engineering, 6(1), 1-15, 2002. DOI: 10.1080/13632460209350407

- [152] Takada, S., N. Hassani, N., Tsuyoshi, T, Ozaki, R., A new proposal for simplified seismic response analysis of pipes in ground with inclined bed-rock. Twelfth World Conference of Earthquake Engineering, Auckland, New Zealand, 2000.
- [153] Takada, S., Tanabe, K., Three dimensional seismic response analysis of buried continuous or jointed pipelines. *Pressure Vessel Technology*, ASME, 109, 80–87, 1987.
- [154] Tan, H., Chopra, A.K., Earthquake analysis of arch dam including dam-water foundation rock interaction. *Earthquake Engineering and Structural Dynamic*, 24, 1453-1474, 1995.
- [155] Toffoli, A., Bitner-Gregersen, E.M., Types of ocean surface waves, wave classification, In *Encyclopedia of Maritime and Offshore Engineering*. John Wiley & Sons, Chichester, UK, 2017.
- [156] Towhata, I., *Geotechnical earthquake engineering*. Springer-Verlag Berlin Heidelberg, Germany, 2008. DOI:10.1007/978-3-540-35783-4_5
- [157] Trifunac, M.D., Scattering of plane SH waves by a semi-cylindrical canyon. *Earthquake Engineering and Structural Dynamics*, 1(3), 267-281, 1972. DOI: 10.1002/eqe.4290010307.
- [158] U.S. Army Corps of Engineers, Engineering and design-earthquake design and evaluation of concrete hydraulic structures. Report No. EM1110-2-6053, Department of the Army, Washington, D.C., USA, 2007.
- [159] Vassilev, V.H., Flores-Berrones, R., Seismic analysis of segmented buried pipelines. *Proceeding of Eleventh World Conference on Earthquake Engineering*, Acapulco, Mexico, 1986.
- [160] Wang, J.T., Zhang, C.H., Jin, F., Nonlinear earthquake analysis of high arch dam-water-foundation rock systems, *Earthquake Engineering and Structural Dynamics*, 41(7), 1157–1176, 2012. DOI:10.1002/eqe.1178.
- [161] Wang, L.R.L., Cheng, K. M., Seismic response behavior of buried pipelines. *Journal of Pressure Vessel Technology*, 101(1), 21-30, 1979.
- [162] Westergaard, H.M., Water pressure on dams during earthquakes. *Transactions*, ASCE, 98, 418-472, 1933.

- [163] Wolf, J.P., Dynamic soil-structure interaction. Prentice-Hall, Englewood Cliffs NJ, USA, 1985.
- [164] Wong, H.L., Effect of surface topography on the diffraction of P, SV, and Rayleigh waves. Bulletin of the Seismological Society of America, 72(4), 1167-1183, 1982.
- [165] Worland, R.S., Wilson, D., The speed of sound in air as a function of temperature. The Physics Teacher, 37(1), 53-57, 1999.
- [166] Wikipedia, Nyquist rate. Wikimedia Foundation, Inc., 2015. www.wikipedia.org/wiki/Nyquist_rate
- [167] Xu, L., Ye, Z.C., Ren, Q.W., Zhang, L., FEM analysis of dynamic response of buried fiber reinforced plastic matrix pipe under seismic load. Mathematical Problems in Engineering, Vol 2013, 1-8, 2013. DOI:10.1155/2013/875376
- [168] Yang, R., Kameda, H., Takada, S., Shell model FEM analysis of buried pipelines under seismic loading. Bulletin of the Disaster Prevention Research Institute, Kyoto University, 38(336), 115-146, 1988.
- [169] Zangar, C., Hydrodynamic pressures on dams due to horizontal earthquake effects. Engineering monograph, Denver, Colorado, USA, 1952.
- [170] Zangeneh, A., Dynamic soil structure interaction of high speed railway bridges. PhD thesis, KTH Royal Institute of Technology, Stockholm, Sweden, 2021.
- [171] Zhang, C.H., Pan, J.W., Wang, J.T., Influence of seismic input mechanisms and radiation damping on arch dam response. Soil Dynamics and Earthquake Engineering, 29(9), 1282-1293, 2009. DOI: 10.1016/j.soildyn.2009.03.003.
- [172] Zhang, J., Li, M., Han, S., Seismic analysis of gravity dam-layered foundation system subjected to earthquakes with arbitrary incident angles. International Journal of Geomechanics, 22 (2), 1-15, 2022. DOI:10.1061/(ASCE)GM.1943-5622.0002268
- [173] Zhang, W., Seylali, E., Taciroglu, E., An ABAQUS toolbox for soil-structure interaction analysis. Computers and Geotechnics, 114, 103143, 2019. DOI: 10.1016/j.compgeo.2019.103143.

- [174] Zhou, J., Wang, T., Chen, W., Lina, B., Xie, X., Emerging investigator series: locally enhanced electric field treatment (LEEFT) with nanowire-modified electrodes for water disinfection in pipes. *Environmental Science: Nano*, 7, 397-403, 2020. DOI: 10.1039/c9en00875f
- [175] Zienkiewicz, O.C., Bicanic, N., and Shen, F.Q., Earthquake input definition and the transmitting boundary conditions. In *Advances in Computational Nonlinear Mechanics*, Springer-Verlag Berlin Heidelberg, Germany, 1989.

NOMENCLATURE

Latin letters-upper case

A	tributary area for the boundary node
B	damping matrix for reservoir
C	damping matrix for dam-foundation
C_f	matrix of damper coefficients c_p and c_s
C_{sediments}	impedance values for sediments
D	outside diameter of pipe
E	Young's modulus
G	shear modulus
H	distance from bottom boundary of foundation to free surface
H	stiffness matrix for reservoir
H_B	depth of soil above centre of the pipeline
K₀	coefficient of soil pressure at rest
K_r	bulk modulus
M	constrained modulus
M	mass matrix
\bar{N}_h	shape functions of dam nodes
N_h	shape functions of reservoir nodes
N_{ch}	horizontal bearing capacity factor for clay
N_{qh}	horizontal bearing capacity factor for sandy soil
N_{cv}	vertical uplift factor for clay
N_{qv}	vertical uplift factor for sand
N_c, N_q, N_γ	bearing capacity factors
Q_h	coupling matrix at reservoir-dam interface
Q_b	coupling matrix at reservoir-foundation interface
R	canyon radius
S	mass matrix for reservoir

S_a^{Target}	target response acceleration
$S_{a-i}^{\text{Response}}$	response acceleration of the recorded motion
T	time
U	particle motion in normal direction
V	wave propagation velocity
V_p	P-wave propagation velocity
V_s	S- wave propagation velocity
V_r	velocity of wave propagation in reservoir water
V	particle motion
W	particle motion in transverse direction
X	spatial coordinate
Y	spatial coordinate
Z	spatial coordinate

Latin letters-lower case

a_s^k	surface control motion in $k = x, y, z$ direction
c	the coefficient of cohesion for backfill soil
c_p, c_s	coefficient for viscous damper in normal and tangential directions
\mathbf{f}^0	effective earthquake forces
\mathbf{f}_f^0	effective earthquake forces at absorbing boundary of foundation
\mathbf{f}_r^0	effective earthquake forces at absorbing boundary of reservoir
f	excitation frequency (Hz)
f_w	arbitrary function
g	gravity constant
g_w	arbitrary function
l_{el}	element length
\mathbf{n}	cosine vectors of the outer normal direction of artificial boundary
\mathbf{n}_h	outward normal vectors to reservoir-dam interface
\mathbf{n}_b	outward normal vectors to reservoir-foundation interface
p	contact pressure

\mathbf{p}_r^t	total hydrodynamic pressures vector in reservoir water
p_r	acoustic pressure
p_u	maximum lateral resistance of soil
\mathbf{q}^t	vector of dynamic forces associated with absorbing boundary Γ_f
\mathbf{q}^0	vector of free-field tractions at absorbing boundary Γ_f
q	damping coefficient for reservoir sediments
$q_{u(up)}$	maximum vertical uplift resistance of soil
$q_{u(down)}$	maximum vertical bearing resistance of soil
\mathbf{r}^0	vector of free-field displacements
\mathbf{r}^t	vector of total displacements
\mathbf{r}_I^0	vector of incident free-field displacements
\mathbf{r}_h^t	displacement vector at reservoir-dam interface Γ_h
\mathbf{r}_b^t	displacement vector at reservoir-foundation interface Γ_b
t_u	maximum axial soil resistance
u_I	incident particle motion
u_R	reflected particle motion
u_T	transmitted particle motion
u_r	fluid particle motion
u_k	displacement component with respect to k -th spatial coordinate
x_u	ultimate relative displacement in axial direction
y_u	ultimate relative displacement in vertical direction

Greek letters

α_a	adhesion factor
α_r	wave reflection factor for reservoir bottom
α_z	impedance ratio
δ'	interface friction angle between pipe and soil
Γ_h	reservoir-dam interface
Γ_b	reservoir-foundation interface

Γ_r	truncated boundary for reservoir
Γ_f	absorbing boundary of the foundation
ξ	structural damping ratio
η	non-dimensional frequency
λ	wavelength
λ_L	Lame's first constant
ν	Poisson's ratio
ρ	mass density
ρ_r	reservoir water density
σ	normal stress
σ_I	incident stress
σ_R	reflected stress
σ_T	transmitted stress
σ_{xx}	normal stress in x-direction
σ_{yy}	normal stress in y-direction
σ_{zz}	normal stress in z-direction
σ_{xy}	shear stress in xz- plane
σ_{xz}	shear stress in xy- plane
σ_{yz}	shear stress in yx- plane
σ^0	free-field stress
τ	shear stress
ε	normal strain
$\bar{\varepsilon}$	volumetric strain
γ	shear strain
γ_s	total unit weight of soil
$\bar{\gamma}_s$	the effective unit weight of soil
ω	circular frequency (rad/s)
Ω_{kj}	rotation about the normal axis of the kj -plane
Ω^0	region interior of the absorbing boundary Γ_f

Ω^+ region exterior of the absorbing boundary Γ_f

Abbreviations

P-waves	Primary waves
S-waves	Shear waves
SV	Shear waves with vertical plane movement
SH	Shear waves with horizontal plane movement
GW	Ground Water
DRM	Domain Reduction Method
PML	Perfectly Matched Layer
1D	One dimensional
2D	Two dimensional
3D	Three dimensional
ALA	American Lifeline Alliance
PGA	Peak Ground Acceleration
FFT	Fast Fourier Transform
IFFT	Inverse Fast Fourier Transform

